이학박사 학위논문

Dynamical Properties of Nearby Galaxies and Their Environmental Dependence

가까운 은하들의 동역학적 특성과 환경 의존성

2019년 8월

서울대학교 대학원

물리·천문학부 천문학전공

정 하 은

Dynamical Properties of Nearby Galaxies and Their Environmental Dependence

가까운 은하들의 동역학적 특성과 환경 의존성

지도교수 박 용 선

이 논문을 이학박사 학위논문으로 제출함

2019년 4월

서울대학교 대학원

물리·천문학부 천문학전공

정 하 은

정 하 은 의 이학박사 학위논문을 인준함

2019년 6월

위 원 장 _____

부 위 원 장 _____

위 원 _____

위 원 _____

위 원 _____

Dynamical Properties of Nearby Galaxies and Their Environmental Dependence

by

Haeun Chung
(hchung@snu.ac.kr)

A dissertation submitted in partial fulfillment of the requirements for the degree of

Doctor of Philosophy

in

Astronomy

in

Astronomy Program
Department of Physics and Astronomy
Seoul National University

Committee:

Professor	Myungshin Im
Professor	Yong-Sun Park
Professor	Woong-Tae Kim
Professor	Changbom Park
Doctor	Jong Chul Lee

To my family.

ABSTRACT

We study the internal dynamical properties of nearby galaxies ($z \sim 0.01 - 0.15$) in the Mapping Nearby Galaxies at Apache Point Observatory (MaNGA) survey data, a part of the 4th generation of Sloan Digital Sky Survey (SDSS), the largest Integral Field Unit (IFU) survey up to date. The main objective of this study is to measure various kinematic properties and the mass profile of galaxies, and find the relation between the characteristics of their mass components and environment. Accordingly, we study the following three research topics.

First, we develop a deconvolution technique for the IFU data to mitigate the effects of the PSF convolution. A simulation shows that the effects of the PSF convolution are significant not only on the observed flux distribution, but also on the derived kinematics, which is linked directly to the dynamical mass distribution. We use the Lucy-Richardson algorithm to deconvolve the IFU data with the knowledge of the wavelength-dependent PSF. The performance of the algorithm is demonstrated by using mock IFU data. Simulations show that the kinematics of galaxies can be well-recovered for the galaxies with various radial profiles of line-of-sight velocity and velocity dispersion. We apply the technique to the SDSS-IV MaNGA data and show that the method results in noticeable difference in the derived kinematics. We also show that the estimation of λ_R parameter, a proxy of the spin parameter λ, can be significantly improved when measured from the deconvolved mock IFU data.

Second, we measure the rotation curve (RC) of nearby galaxies and study its environmental dependence. We propose an improved analytic model of RC, a combination of the hyperbolic tangent function and a linear term, to properly model the shape of galaxy rotation curves, especially at the outskirt of galaxies. We measure the 2D distribution of the line-of-sight velocity from the deconvolved IFU data of 4,425 unique MaNGA main galaxies and fit our RC model to them. We also calculate the small-scale (R_n, the projected distance to the nearest neighbor galaxy) and the large-scale (ρ_{20}, the background mass density estimated from the 20 nearest galaxies) environmental

parameters of the MaNGA galaxy samples. We investigate the RC of ~ 600 late-type MaNGA galaxies in details. It is found that the slope of RC is quite diverse at their outer radii ($> 1R_e$). The slope has a strong positive correlation with the galaxy stellar mass and the RC scale radius, where the central rigid body rotation ends. When the T morphological type (T-Type) of the galaxies is greater than or equal to 2, the slope shows strong mass dependence and no T-Type dependence. However, for the galaxies with T-Type less than 2, the mass dependence disappears and only T-Type dependence remains. Our results show that the shape of galaxy RC is closely related with environment, in particular with the distance to the nearest neighbor galaxy and the background mass density. We speculate that this is resulted by the cumulative effects of galaxy-galaxy interactions and also by the instantaneous influence by the nearest neighbor galaxy.

Third, we measure the radial profile of the mass components of MaNGA galaxies using Jeans-anisotropic-model (JAM). We use the mass density model composed of stellar mass and dark matter halo components. We fit the surface brightness distribution of the galaxies using the Multi-Gaussian-Expansion method, and apply the JAM method with the 2D line-of-sight RMS velocity distribution ($\mathrm{V_{RMS}} = \sqrt{\mathrm{V}^2 + \sigma^2}$) to fit the mass density model parameters under the Markov Chain Monte Carlo scheme. The obtained 3D mass density distributions exhibit a various combination of the M_*/L ratio, the velocity anisotropy, the dark matter fraction, and the dark matter halo inner density slope.

In addition to the above studies, we work on an instrument development project that can extend the current study. The instrument called Devasthal Optical Telescope Integral Field Spectrograph (DOTIFS) is a fiber-lenslet based multi-IFU optical spectrograph which can observe 16 objects simultaneously. The real-time deployable IFUs have a significant advantage over the other optical multi-IFU instruments, which have considerable overhead time for the IFU reconfiguration. We have performed a conceptual design study of the instrument in the early stage of the project and proposed a feasible design which fulfills all the demands from science requirements. We have de-

signed the optical systems of the instrument, which are the spectrograph collimator and camera optics, the fore-optics, and the calibration unit optics. We perform a tolerance analysis and a thermal analysis and suggest a solution to mitigate the impact of temperature variation on optical performance. We also have developed ancillary software for the instrument, such as a spectrograph CCD image simulator and a signal to noise ratio calculator.

Keywords: galaxies: dynamics – galaxies: rotation curve – techniques: deconvolution – instrumentation: IFU – instrumentation: spectrograph

Student Number: 2012-23104

Contents

List of Figures

List of Tables

Chapter 1

Introduction

1.1 Dynamics of Galaxies and Integral-Field-Unit Spectroscopy

Revealing the distribution of galaxy mass and its components is one of the primary interest to understand the structure and formation of the galaxies. Naively, the distribution can be inferred from the distribution of the luminous matters (stars and gas) which are observable, but not entirely due to the existence of the non-observable component - the dark matter. Since the discovery of flat rotation curve (RC) at M31 (Rubin & Ford 1970) and following observations in the multiple wavelengths to the other samples (Roberts & Whitehurst 1975; Faber & Gallagher 1979; Bosma 1981b; Rubin et al. 1985; Kent 1987; Sofue & Rubin 2001), the flat RC gradient at the outer radii of the galaxies is considered as a strong observational evidence of the existence of the dark matter, although there are other attempts to explain the observed kinematics without the dark matter (e. g. Modified Newtonian dynamics; Milgrom 1983). This is because the distribution of observable matters can not fully explain the flat RC at the outer radii within the Newtonian gravity framework.

Although the dark matter is not directly observable, their distribution in a galaxy scale can be inferred by the motion of the observable matter which follows the gravitational potential generated by total mass (baryonic + dark matter) distribution. With

the knowledge of kinematic motion of the galaxies and the distribution of the luminous matters, the total mass distribution can be estimated by dynamical modeling. Therefore, understanding the dynamics of galaxies is essential to study the distribution of the dark matter.

Previous studies on galaxy dynamics mostly concentrated on gas dynamics before 2000s (Mathewson et al. 1992; Courteau 1997; Sofue & Rubin 2001). Hα in optical or HI in radio are the primary kinematic tracers of the gravitational potential. The gas kinematics well follows the gravitation potential, thus can be used to study the kinematics at the outer region of the galaxies (several effective radii) where the dark matter is expected to be dominating, yet the region is difficult to observe by the galaxy stellar components. However, measuring the line-of-sight kinematics with Hα or HI have been limited to small number of galaxy samples because they are quite time costly. Hα observed by long-slit spectrograph requires multiple pointing with non-negligible exposure time, and HI requires interferometry observation which requires multiple dishes to obtain sufficient spatial resolution. Moreover, those observations are possible with gas-rich galaxies only which limit the study of galaxy dynamics to the late-type galaxies.

The advent of integral-field-unit (IFU) spectroscopy allows to study the spatially resolved kinematics of galaxies with lower observation cost. IFU data contains three dimensional information of an object, which is spectra at each spatial location in the IFU field of view. It allows us to understand the dynamical structure of galaxies not only for gas-poor but also gas-rich galaxies in greater detail. Along with the increasing number of IFU spectroscopy instruments in the world, several IFU surveys of galaxies have been conducted such as ATLAS^{3D} (Cappellari et al. 2011), DiskMass (Bershady et al. 2010), CALIFA (Sánchez et al. 2012), MASSIVE (Ma et al. 2014), SAMI (Croom et al. 2012), and MaNGA (Bundy et al. 2015). Consequently, the number of galaxy samples per survey is increasing rapidly from 260 galaxies of ATLAS^{3D} to $\sim$10,000 galaxies of MaNGA. Statistical study of the various two-dimensional properties of the galaxies becomes possible with the increased sample size. In addition, a dynamical modeling method has developed and applied widely to the IFU data (Cappellari 2008).

The method predicts the line-of-sight velocity root-mean-square distribution with the underlying mass distribution and the dynamical model of galaxies. The output from the model can be directly compared with the measured kinematics from IFU data, therefore the model is used to estimate the dynamical properties of the galaxies, including dynamical geometry, velocity ellipsoid shape and the mass profile of the galaxies. The method called Jeans-anisotropic model (JAM) becomes popular tool to study the 3D mass profile of the galaxy.

1.2 Environmental Effects on Galaxy Dynamics

It is well known that various galaxy properties are closely related with galaxy environment (Dressler 1980; Postman & Geller 1984; Dressler et al. 1997; Lewis et al. 2002; Gómez et al. 2003; Kauffmann et al. 2004; Park & Hwang 2009). Especially, multi-object spectroscopic surveys play an important role to reveal the environmental dependence of galaxies by providing reliable distance to the galaxies (redshift) therefore the three-dimensional distribution of neighbor galaxies can be estimated accurately. However, the environmental effects on galaxy dynamics are relatively not well studied due to the lack of information on the dynamical properties of galaxies.

Such studies become available with the increased number of IFU survey data. The kinematic structure of the early-type galaxies are found to be dominated by fast-rotators, which have ordered-rotation dominant angular momentum rather than the velocity dispersion, using λ_R[1] parameter (Emsellem et al. 2007; Cappellari et al. 2007; Emsellem et al. 2011; Graham et al. 2018). Lee et al. (2018) studied the environmental dependent of λ_{R_e}[2]. They found that when a late-type galaxy with $10 < \log_{10}M_*/M_\odot < 10.5$ have an early-type galaxy as the closest neighbor, λ_{R_e} is decreasing as the distance to the closest neighbor decreases. However, it is also reported that the average slow rotator fraction remains unchanged across five orders of magnitude in galaxy number density (Houghton et al. 2013, using 27 galaxies in the Coma cluster), the λ_{R_e} does

[1] proxy of the spin parameter λ

[2] λ_R calculated within one half-light radius aperture

not show much correlation with various environmental parameters (Veale et al. 2017, using 360 local early-type galaxies), and there is no clear difference on the dependence of angular momentum content on the stellar and the halo mass components between the central and satellite galaxies (Greene et al. 2018, using 379 central and 159 satellite early-type galaxies).

Environmental dependence of λ_R is also studied in the cosmological hydrodynamic simulation. Choi & Yi (2017), studied the galaxy spin evolution in the cluster environment. They found that the galaxy spin is globally decreasing with cosmic evolution due to the various events which are more frequently happening in the cluster environment compare to the field. The result is supported by another study using Horizon-AGN simulation data, which shows that non-merger tidal perturbation effects is the major contributor to the evolution of early-type galaxy spin evolution (Choi et al. 2018). Both studies utilize the λ_R parameter measured from mock-galaxies. There are studies which demonstrate the role of mergers to the galaxy spin evolution (Naab et al. 2014; Penoyre et al. 2017), but not in the context of environment. Lagos et al. (2018) found that slow rotator fraction, F_{SR} is primary depend on the stellar mass, but the fraction shows only weak dependence on the environment. They use 16,358 mock galaxies from EAGLE and HYDRANGEA simulation (Schaye et al. 2015; Bahé et al. 2017).

Most of the previous studies with both observation or simulation data utilize λ_{R_e} as a tracer of galaxy kinematics. Because the parameter is calculated with an aperture of $1R_e$[3], it does not contain the dynamical information outer than $1R_e$. Therefore, the further study with kinematic parameter, which could include information beyond the $1R_e$ is desirable to understand the environmental effect to the kinematic properties of the galaxies in detail.

1.3 SDSS-IV MaNGA IFU Survey

MaNGA (Mapping Nearby Galaxies at Apache Point Observatory)(Bundy et al. 2015) is an integral field spectroscopy survey project of the 4^{th} generation of Sloan Digital

[3]Radius which contains half of the total light of galaxy

Sky Survey (SDSS-IV). Its aim is to observe ∼10,000 galaxies in its 5-years survey duration. MaNGA instrument is designed to obtain spatially-resolved spectroscopy data from 17 objects simultaneously, by putting 17 IFUs within the 3° diameter field of view of the 2.5m Apache Point Observatory (Gunn et al. 2006). It utilizes the BOSS spectrograph (Smee et al. 2013), which covers a wavelength range of 3,600 - 10,300Å with the median spectral resolution of 2,000. The main science goals of the survey are understanding the growth and assembly history of galaxies, their star formation quenching mechanism and its relation with environment, and the formation of the sub-components of galaxies. More details of the survey can be found in the following papers; Yan et al. (2016a) (Survey design, execution and initial data quality), Drory et al. (2015) (IFU and fiber feed system), Wake et al. (2017) (Target selection and design), Law et al. (2015) (Observing strategy), Law et al. (2016) (Data reduction pipeline), and Yan et al. (2016b) (Spectrophotometric calibration). The latest data release (DR) of SDSS-IV is DR15 (Aguado et al. 2019), which became public in 2018 December. It includes 4,824 MaNGA IFU data cubes. Here we summarize the part of the MaNGA survey that is relevant to this thesis. We present the details of MaNGA survey samples below. In Appendix A, we describe MaNGA IFUs and its data reduction pipeline.

MaNGA is designed to observe a large number of galaxies that can provide the spatially varying spectroscopic properties of galaxies with sufficient statistical significance. Its target galaxies fulfill three main requirements: 1) A flat distribution in K-corrected i-band absolute magnitude (M_i) which is a reliable proxy of stellar mass without potential systematic bias, 2) Uniform radial coverage up to 1.5 R_e or 2.5 R_e. 3) Maximum spatial resolution and signal-to-noise ratio (S/N) considering the extant instrumentation and survey duration. MaNGA targeting catalog is complied by using an NSA catalog (Blanton M. `http://www.nsatlas.org`) which contains nearby galaxies within 200 Mpc ($z \simeq 0.055$), mostly based on the SDSS DR7 MAIN galaxy sample (Abazajian et al. 2009) with addition of near- and far-UV photometry data from *GALEX* survey. An extended version of the NSA catalog (version 1_0_1) have additional targets up to z=0.15 along with the photometry measured by elliptical Petrosian aperture, and

serves as a parent catalog of MaNGA survey. The catalog contains useful measured and derived quantities such as absolute magnitudes, stellar mass from photometric SED fitting (using kcorrect v4_3), etc. The final MaNGA targeting catalog and IFU size distribution are determined based on an extensive trade-off study to meet the three main requirements with the given parent NSA catalog.

In the targeting catalog, three main sample groups are defined. 1) Primary samples which have a radial coverage to 1.5 R_e with flat number density in M_i space. 2) Secondary samples with a radial coverage to 2.5 R_e as well as flat number density in M_i space. 3) Color-Enhanced samples which is a supplement sample to the Primary samples. This is designed to fill the NUV-i color vs M_i plane where low-mass red galaxies and high-mass blue galaxies are located. It should be noted that the number of galaxies in the samples is larger than the total number of galaxies which MaNGA aims to observe ($\sim$10,000). Actual target galaxies to be observed are selected as the survey progresses from the targeting catalog. Thus, there is no final list of MaNGA galaxies before the end of survey. In addition to the MaNGA main galaxy samples, there are ancillary samples which are selected for supplementary science goals. Most of the ancillary targets are single galaxies except for the IC342, Coma, and M31 samples which are targeting regions or intra-cluster light.

Among the 4,824 DR15 MaNGA cube data, it is known that there are 4,621 unique galaxies (67 repeated observations) and 136 special targets with IC342, Coma, and M31. The number of unique MaNGA main galaxies is 4430 (Primary: 2,090, Color-Enhanced: 1,645, Secondary:698. There are 3 overlaps between the Color-Enhanced and the Secondary)(Aguado et al. 2019). However, the known statistics is based on the 'MANGAID' identifier which uniquely identifies each object *within the same input catalog*. In DR15, there are five galaxies (In PLATE-ID designation, they are 9872-3703/7443-1902, 9872-1901/7443-1901, 9872-3702/7443-3701, 8983-3703/7495-12704, 8952-12703/7495-12703) with different MANGAID's but have an identical 'NSAID or IAUNAME', meaning that they are hidden duplicates. Half of them have MANGAID starting with 12, which are drawn from the older version of the NSA catalog as noted

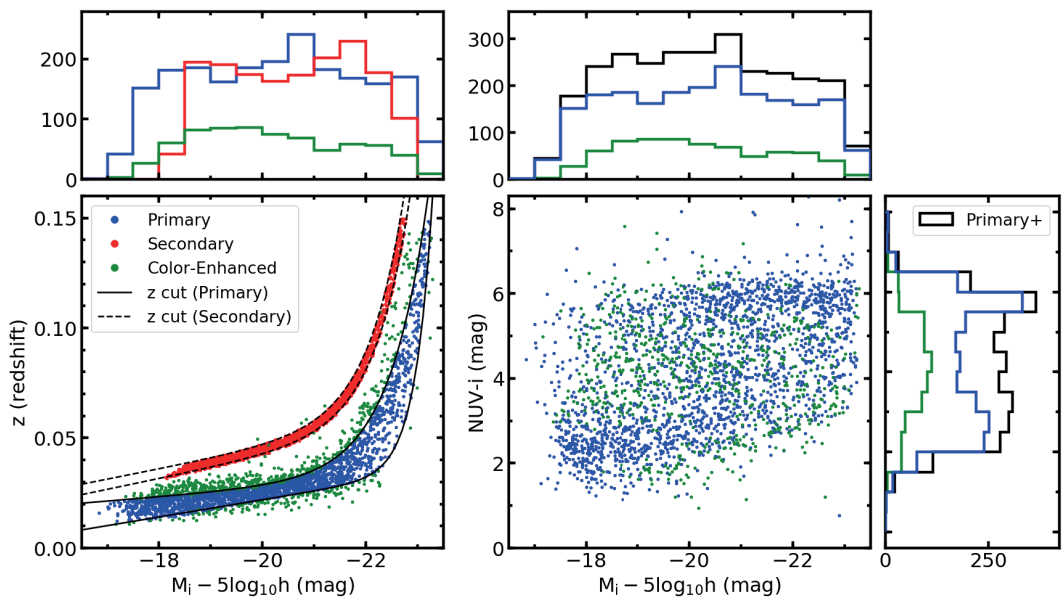

Figure 1.1. (left) Distribution of SDSS DR15 MaNGA main galaxies on the z-M_i plane. Blue, red and green points represent Primary, Secondary, and Color-Enhanced sample respectively. The solid and dashed lines are redshift limit of Primary and Secondary samples from equation 3 of Wake et al. (2017). The upper side histogram shows the nearly flat distribution of the observed MaNGA galaxies on the M_i plane. (right) Distribution of MaNGA Primary and Color-Enhanced sample galaxies on the (NUV − i) - M_i plane. The upper and right side histograms show the marginalized histogram of Primary, Color-Enhanced, Secondary sample on the M_i and NUV − i plane respectively.

in the SDSS MaNGA webpage[4]. Since all of them are marked as a Primary sample, half of them should be considered as duplicates if one wish to deal only unique galaxies. Considering those additional duplicates, there are 4,616 unique galaxies in the DR15 MaNGA data. Figure 1.1 shows the distribution of the *observed* MaNGA main galaxies (Primary, Color-Enhanced, and Secondary) up to date (DR15) on the z - M_i plane, and the $(NUV - i)$ - M_i plane. The Primary and the Secondary samples are strictly chosen from the given redshift cuts (Wake et al. 2017). The Color-Enhanced samples are chosen from the extended redshift range from the Primary samples, thus their location on the z - M_i plane are near the Primary sample redshift cut boundaries. On the $(NUV - i)$ - M_i plane, the distribution of the Color-Enhanced samples efficiently fill the region where the Primary samples do not (high mass blue galaxies, and low mass red galaxies). The marginalized histogram of the Primary+ samples (Sum of the Primary and the Color-Enhanced samples) on the $(NUV - i)$ plane show that the distribution are became flatted by the addition of the Color-Enhanced samples.

1.4 Devasthal Optical Telescope Integral Field Spectrograph (DOTIFS)

(This section and Appendix B are published in the SPIE Proceedings and the Publications of the Korean Astronomical Society)[5]

Integral Field Unit (IFU) spectrograph is an instrument which could obtain spectra of two-dimensional object(s) in one go, thus it provides a large amount of spectral data in homogeneous condition efficiently. On the account of its two-dimensional field of view over the traditional long-slit spectrographs, IFU instruments have became quite popular nowadays (see examples in section 2.1). However, there is still a dearth of IFU instruments therefore there is high demand for a new IFU instrument. Moreover, the number of multi-IFU instruments is even fewer, which will be a great advantage if there is such an instrument.

[4]https://www.sdss.org/dr15/manga/manga-data/catalogs/

[5]Chung et al. (2014, 2015, 2018a,b)

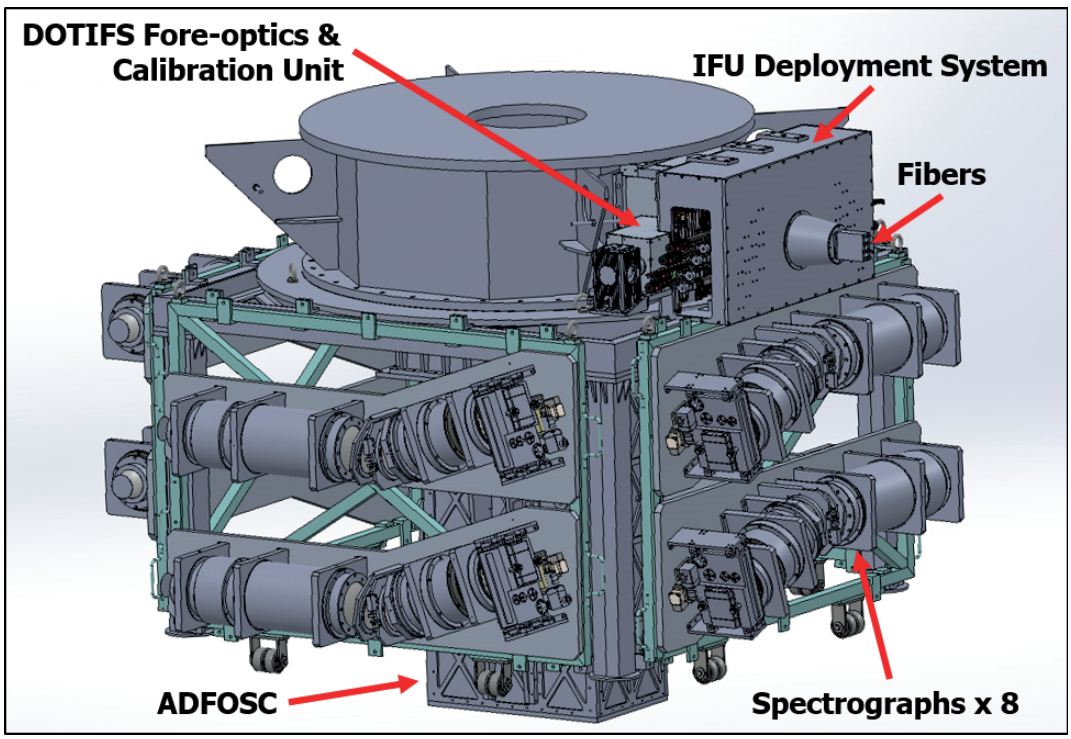

Figure 1.2. Overall mechanical rendering of DOTIFS mounted on the 3.6m Devasthal telescope. Each part of the spectrograph is pointed out with red arrows. 8 spectrographs are located around the main port instrument ADFOSC. 2 spectrographs are mounted at each side, in total four sides. Fibers between the IFU deployment system to each spectrograph are not shown.

Devasthal Optical Telescope Integral Field Spectrograph (DOTIFS) (Chung et al. 2014) is being developed to fill exactly the need for such an multi-IFU instrument. Figure 1.2 shows an overall mechanical layout of the instrument. It is planned to be mounted on 3.6m Devasthal optical telescope (Sagar et al. 2012) in Nainital, India. DOTIFS is designed to observe up to 16 independent extended objects, with IFUs which can be deployed over the $8'$ diameter field of view in a single exposure. An automated deployment system is introduced to deploy IFUs precisely and rapidly at the desired location on the sky. Each IFU covers $8.7'' \times 7.4''$ on the sky with hexagonal shape sampling elements. The sampling size is $0.8''$, which is matched with the median seeing size at the observing site. The IFUs are buttable (i.e. can be deployed next to each other) which provides great advantage for in depth observation of a single object as well. Light from the sampling elements are dispersed by eight identical spectrograph with the spectral resolution of R=1200-2400 over the 370-740 nm wavelength coverage.

DOTIFS supports a number of complementary capabilities over the other IFU instruments. For example, MaNGA (Bundy et al. 2015) has higher IFU multiplicity than the DOTIFS, but it has relatively low spatial resolution and it can hardly be used for PI-observation because it is designed for a specific survey. On the other hand, DOTIFS has higher spatial resolution, configurable any time with low overhead (less then CCD readout time). It also has higher efficiency with the larger telescope aperture size. Thus, DOTIFS can be used for multiple purposes such as a follow up observation for MaNGA targets, a new survey, or targeting an individual object in detail.

The primary scientific goals of DOTIFS are related with the nearby galaxies. This includes rotation curves of nearby galaxies, HII regions, and merging/interacting galaxies. Here we list proposed science topics for DOTIFS. Each topic requires either a single wide-field IFU or multi-IFU functionality. Detail descriptions of each topic can be found in DOTIFS science reference document. (Publication in preparation)

- HII regions in our galaxy and nearby galaxies.

- Circum-nuclear rings in barred galaxies

- Merging, and Interacting galaxies, ultra-luminous infrared galaxies.
- Galaxies in clusters and Groups, Star formation as a function of environment
- Outer regions of star forming galaxies
- Hα emission from Lyman-α clouds
- Hα rotation curves of nearby galaxies
- AGN outflows, Dual AGNs or pairs
- Emission-line galaxies at intermediate redshifts

Instrumentation group at the Inter-University Center for Astronomy and Astrophysics (IUCAA, Pune, India) is leading the project, and performing all the design, assembly, test, and integration of the instrument. Aryabhatta Research Institute of Observational Sciences (ARIES, Nainital, India) is operating the Devasthal telescope, and Korea Institute for Advanced Study (KIAS, Seoul, Korea) and Seoul National University (SNU, Seoul, Korea) are participating as international collaborators.

DOTIFS was first proposed by IUCAA in 2011, after the successful commissioning of a proto-type IFS, FIFUI (Srivastava et al. 2011) on the IUCAA 2-m Girawali telescope in 2010. Following the first proposal, a conceptual design study was initiated when KIAS joined the project in 2012. Since then, enormous effort has been putted to realize this extraordinary multi-IFU optical spectrograph. It had been through conceptual design review (October 2012), baseline design review (April 2013), and optics design review (June 2014). Progress has been made continuously from then. Currently, the project is divided into two stages, the first stage with 4 IFUs and 2 spectrographs, and the second stage with additional 12 IFUs and 6 spectrographs. As of June 2019, most of the main components (including lenses for fore-optics, calibration unit and spectrographs, filter, grating, CCD, microlenses, and optical fibers) are received and the project is in the assembly, integration and testing phase of its first stage.

In Appendix B, we highlight the contributions on this project. We give an overview of the instrument with the rationale behind the instrument design parameters in sec-

tion B.1. We describe the details of the fore-optics/calibration unit and the spectrograph optics in section B.2. We present software part of the instrument in section B.3, which includes S/N calculator and the CCD image data simulator.

1.5 Purpose of the Thesis

In this thesis, we try to understand the dynamical properties of nearby galaxies and their environmental dependence using Integral Field Spectroscopy survey data. First, we develop a new procedure for the PSF deconvolution of the IFS data to mitigate the effects of PSF, which correlates the spatial information. The small-scale spatial structure can be recovered, which is essential to study the kinematics and the dynamics of galaxies. Second, we investigate the environmental dependence of the galaxy rotation curve shape. We focus on the slope of the rotation curve at the outer radius ($> 1R_e$) where the dark matter becomes dominating the mass component fraction. Third, we model the 3D mass distribution of galaxies using Jeans-Anisotropic Model and decompose the mass profile of the galaxies into the baryonic and the dark matter. We measure the mass density slope of the galaxies and study their relation with the environment. The rest of this thesis is structured as fellows. In chapter 2, we describe a PSF deconvolution method that can be applied to any kind of IFU data. We validate our method by using mock IFU data and show its application to the real IFU data and measurement of the spin parameter proxy. In chapter 3, we investigate the relation between the shape of galaxy rotation curve and the environmental parameter. We introduce a new model which can describe the outer shape of the galaxy rotation curve. We show the result of the dynamical mass modeling of nearby galaxies in chapter 4. We summarize the main result of this thesis in chapter 5.

Chapter 2

PSF Deconvolution of the IFU Data and Restoration of Galaxy Stellar Kinematics

2.1 Introduction

Integral Field Spectroscopy (IFS), or 3D spectroscopy is an observation technique which can collect the two-dimensional spatial information simultaneously in the multiple wavelengths. IFS observation is performed by a single or multiple Integral Field Unit(s) (IFU(s)). Starting from SAURON IFU (Bacon et al. 2001), many IFS instruments (GMOS (Allington-Smith et al. 2002), VIMOS (Le Fèvre et al. 2005), IMACS (Dressler et al. 2011), PMAS/PPAK (Kelz et al. 2006), KMOS (Sharples et al. 2013), MUSE (Bacon et al. 2010)) have been developed in the optical and near-infrared. Nowadays there are thousands of publicly available IFU data from a number of IFU surveys such as ATLAS^{3D} (Emsellem et al. 2011), DiskMass (Bershady et al. 2010), CALIFA (Sánchez et al. 2016), SAMI (Scott et al. 2018), and MaNGA (Bundy et al. 2015). However, all of the IFU data from fore-mentioned ground-based surveys have a common fundamental limitation(unless corrected by Adaptive Optics): its spatial information is degraded by the Point Spread Function (PSF). It is the combination of the atmospheric seeing, the

aberration from the telescope and instrument optics, and the sampling size/scheme. Notably, the effect becomes more severe for the data obtained by bare fiber-based IFU, because of the physical gap between sampling elements which enlarges effective PSF size. Figure 2.1 shows the degraded image quality of the reconstructed MaNGA *gri* image compare to the SDSS *gri* image. MaNGA fiber is five times larger than the SDSS camera pixel and there is a gap between fibers as can be seen in the fiber arrangement of the 127 fiber MaNGA IFU. Due to the effect of PSF, every derived, measured, or fitted quantities from the IFU data are smoothed and becomes spatially correlated. To fully extract the spatially resolved information from the IFU data, one must overcome the effect of PSF with the best of knowledge. One possibility is accounting the PSF effect by the flux-weighted PSF convolution to the 2D model quantities (Cappellari 2008; Bouché et al. 2015), but this is only an approximation which cannot fully reflect the PSF effect.

Historically, there were numerous attempts that tried to mitigate the effects of PSF on 2D images particularly in the field of signal/image processing (see summary in Bongard et al. (2011), Villeneuve & Carfantan (2014) and references therein). However, those techniques are not directly applicable to the astronomical data since they are optimized to 3 channel color images or images which have different characteristics compared to astronomical images. There were studies that applied deconvolution in the field of astronomy, such as optimal spectrum extraction from the CCD image (Courbin et al. 2000; Lucy & Walsh 2003), or reduction of the *Spitzer* slit spectroscopy data (Rodet et al. 2008). More recently, several techniques (Bourguignon et al. 2011; Soulez et al. 2011; Bongard et al. 2011; Villeneuve & Carfantan 2014) were proposed to restore the spatially and spectrally correlated 3D cube data in the context of MUSE (Henault et al. 2003). Especially, Bongard et al. (2011) utilize the prior knowledge on the spatial and spectral correlation to deconvolve the IFU data by using a regularized χ^2 method. This technique accompanies a process of exploring the two hyper-parameters which are required for the deconvolution, by trial and error with the visual inspection. Besides, Villeneuve & Carfantan (2014) proposed nonlinear deconvolution technique on the IFU

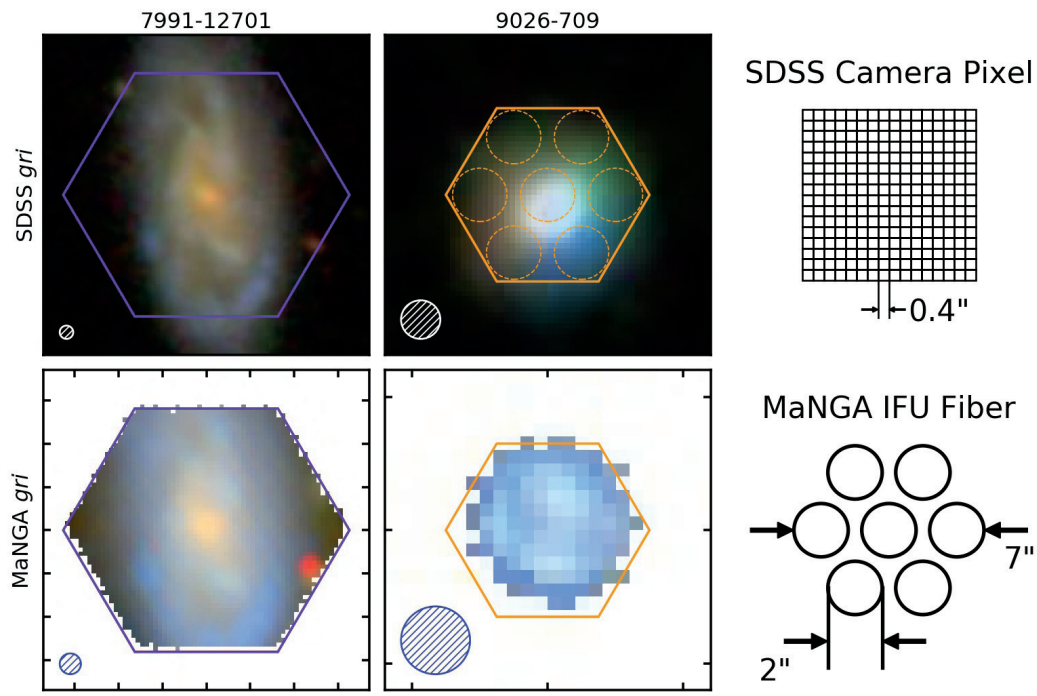

Figure 2.1. (left) SDSS *gri* image[a] and reconstructed MaNGA *gri* composite image of a MaNGA galaxy (PLATE-IFU: 7991-12701). Hatched circles represent a size of effective r-band PSF FWHM of SDSS and MaNGA image. Hexagon represents IFU field of view. A tick size is $5''$. (middle) SDSS *gri* image and reconstructed MaNGA *gri* image of a standard star observed by a MaNGA mini-IFU (PLATE-IFU: 9026-709). Dashed circles show a footprint of a mini-bundle fibers. (right) Schematic diagram of the sampling size of SDSS camera and MaNGA IFU. A size of the center to center gap between adjacent fibers is $0.5''$.

[a]Image Cutout API, http://skyserver.sdss.org/dr15/en/home.aspx

data with Markov-Chain Monte-Carlo in Bayesian framework, to recover the flux, relative velocity and the velocity dispersion distribution of the target. The technique was demonstrated on the simulated IFU data with two separated emission line objects in the narrow wavelength range. Although the technique achieved its goal to some extent, the result did not surpass the approach used by Bongard et al. (2011), and was not able to sufficiently restore the velocity dispersion distribution.

In this chapter, we explore a general method to overcome the effect of PSF which can be applied to any kind of IFU data. Particularly, we study the performance of the direct PSF deconvolution on the extended source (galaxy) to restore its true kinematics. We use the Lucy-Richardson (LR) algorithm (Richardson 1972; Lucy 1974), which is one of the simplest deconvolution techniques and requires a minimum number of parameters. We validate the algorithm using mock IFU data and show that the kinematics of galaxies can be well-restored through our deconvolution procedure. In addition, we apply the deconvolution to measure the spin parameter $\lambda_{\mathrm{R_e}}$ (Emsellem et al. 2007), which is a widely-used proxy of the galaxy angular momentum.

This chapter is organized as follows. In section 2.2, we introduce the LR deconvolution algorithm and its implementation to the IFU data. We demonstrate the validity of the deconvolution technique using the mock IFU data in section 2.3. In section 2.4 we illustrate the example of deconvolution to the MaNGA IFU data. We finally show how the application of the deconvolution improves the measurement of the spin parameter $\lambda_{\mathrm{R_e}}$ in section 2.5 and present a summary in section 2.6.

2.2 PSF Deconvolution of IFS Data

2.2.1 Lucy-Richardson Deconvolution Algorithm

Lucy-Richardson (LR) deconvolution algorithm is an iterative procedure to recover an image which is blurred (convolved) by a PSF. The algorithm is introduced here in a simple form,

$$u^{n+1} = u^n \cdot \left(\frac{d}{u^n \otimes p} \otimes p\right) \tag{2.1}$$

where u^n is n^{th} estimate of the maximum likelihood solution ($u^0 = d$), d is a PSF-convolved image, and p is 2D PSF. If d follows the Poisson Statistics and u^n converges as iteration proceeds, u^n becomes the maximum likelihood solution (Shepp & Vardi 1982). The LR deconvolution has several advantages that 1) it is straight-forward to implement, 2) requires a minimum number of parameters to perform, 3) can be done quickly on the average computing machine. If the shape of the PSF is known as Gaussian, the procedure can be done with only two parameters, 1) Full-Width-Half-Maximum (FWHM) of Gaussian function and 2) a number of iteration to perform. The algorithm produces a non-negative solution since it assumes Poisson Statistics. The well-known drawback of the algorithm is the noise amplification and the ringing artifact structure around sharp feature when the number of iteration (N_{iter}, Magain et al. (1998)) becomes high. Therefore, the relationship between the S/N of the image, N_{iter}, and the result of the deconvolution should be investigated to ensure the quality of the result for the further scientific analysis.

2.2.2 Implementation to the IFU Data

We develop a Python3 code to apply the LR deconvolution algorithm to the optical IFU data. We consider an IFU data as a combination of 2D images at different wavelengths and perform deconvolution of the image at each wavelength slice independently. In other words, we do deconvolution only in the spatial dimension, not in the spectral direction. The core part of the procedure is written in Equation 2.1. Fast-Fourier Transform (FFT)(Cooley & Tukey 1965; Press et al. 2007) is implemented to increase the speed of the procedure. Different size of PSF can be used at each wavelength slice to cope with the wavelength dependency of the PSF FWHM. To maximize the execution speed of FFT, we perform a zero padding on the 2D slice image to increase its size to $2^{\mathrm{N}} \times 2^{\mathrm{N}}$ before deconvolution. We also mark the bad pixels and non-positive pixels. The marked pixels are replaced by an iterative value-correction process, which alters the marked pixels to the average of the nearest positive pixel values. The process is performed multiple times, until the boundary of the data is extended by three times of $\mathrm{FWHM_{PSF}}$.

This process significantly reduces the artificial effect due to the sharp edge in the result of the deconvolution. The LR deconvolution is performed on the value-corrected $2^N \times 2^N$ size image. The values which were replaced by the iterative value-correction process are masked to zero after the deconvolution, and the padded region is cut out.

2.3 Deconvolution Performance Verification on the Mock IFS Data

In this section, we show the feasibility of the deconvolution by using numerous mock IFS data. We present parameters of the model galaxy, and the details about the mock IFU data production. We describe the method for the kinematic measurements and the RC model fitting on the mock IFU data. Finally, we report the performance of the deconvolution depending on N_{iter} and $\mathrm{FWHM_{PSF}}$. The performance is also validated by the Monte-Carlo mock IFU data which reflects various galaxy light profile, S/N distribution, and kinematics.

2.3.1 Mock Galaxy Model

We define a mock galaxy model which resembles a real rotating galaxy on the sky. Our mock galaxy model is composed of sub-models with simple photometric and kinematic models, which are Sérsic profile, RC model (see subsection 3.3.1), and radially dependent velocity dispersion function. The velocity dispersion function is defined as

$$\sigma_r = \sigma_0/(r + R_1) \tag{2.2}$$

where σ_0 is a velocity dispersion at the center, r is a circular radial distance from the center of a galaxy, and R_1 is a characteristic scale which is set as identical to the one in the RC model. The σ_r form is taken from (Graham et al. 2018), and it well describes the actual velocity dispersion distribution of galaxies (see subsection 2.4.3).

2.3.2 Mock IFS Data

We generate three *groups* of mock IFS data. The groups are designed to test the performance of the deconvolution in various aspects: Group 1 - effects of the number of deconvolution iteration, Group 2 - effects of the size of $\mathrm{FWHM_{PSF}}$, and Group 3 - effects of the galaxy photometric and kinematic distributions. Each group is characterized with multiple *sets* of model parameters, which are used to generate the mock galaxy IFU data. The detailed process of mock cube generation is described in section C.1.

The purpose of Group 1 is to investigate the performance of the deconvolution with respect to the number of deconvolution iteration. We determine sets of model parameters as in Table 2.1 to elaborate the diverse properties of galaxies. We use the realistic model parameters which could represent the photometric and kinematic distributions of actual galaxies which are similar to the target galaxies of SDSS-IV MaNGA IFU survey. Especially, the S/N at one half-light radius (1 R_e) is defined similarly to the MaNGA data product, which ranges S/N=14-35 per spatial element per resolution element (Bundy et al. 2015). We also choose the size and shape of the mock field of view to mimic those of MaNGA IFU. Combination of S/N at 1 R_e, Sérsic index (n_{Sersic}), inclination, R_1, and $1/R_2$ yields 216 sets of mock galaxies ($3 \times 2 \times 3 \times 4 \times 3 = 216$) (see section 3.3 for the definition). From the sets of galaxy parameters we construct three types of mock IFU data. Type 1 (*Free*) is an ideal IFU data without any PSF or noise (i.e. free from atmospheric seeing effects and optical aberrations). Type 2 (*Conv*) is a realistic IFU data where Gaussian PSF is convolved and the Gaussian noise is added. Type 3 (*Deconv*) is a deconvolved IFU data which is obtained by performing the deconvolution procedure to the Type 2 IFU data. We construct 216 *Free* mock IFU data, and generate 25 *Conv* IFU data for each of *Free* data with different random seed. This is to quantify the effect of random noise. We assume the wavelength dependent $\mathrm{FWHM_{PSF}}$ which corresponds to the $\mathrm{FWHM_{PSF,\lambda}} = \mathrm{c_0} + \mathrm{c_1} \times \lambda$, where c_0 and c_1 are as in the Table 2.1. Lastly, 20 *Deconv* IFU data are produced per each *Conv* IFU data with $N_{iter} = 1$ to 20. In total, 216 *Free* cube, 5,400 *Conv* cubes, and 108,000 *Deconv* cubes are produced as Group 1.

Group 2 is designed to investigate the effect of $\mathrm{FWHM_{PSF}}$ in two aspects; 1) the effect of the convolved PSF FWHM size ($\mathrm{FWHM_{Conv}}$), and 2) the effect of the PSF FWHM size used for the PSF deconvolution ($\mathrm{FWHM_{Deconv}}$). This is to verify the effect of deconvolution for the practical situation 1) where each IFU data is observed with various atmospheric seeing size and 2) where the $\mathrm{FWHM_{Deconv}}$ being different from the actual effective $\mathrm{FWHM_{Conv}}$. These effects are identified to ensure that the deconvolution provides more accurate kinematics compare to the one from the non-deconvolved data even with a little inaccurate $\mathrm{FWHM_{Conv}}$. We again construct three types of mock IFU data using the parameters given in Table 2.1. Group 2 - Type 1 data is identical to the Group 1 - Type 1 data. For each of the Group 2 - Type 1 *Free* IFU data, we produce 75 *Conv* IFU data with 3 different c_0 values as in Table 2.1 (i.e. 25 *Conv* IFU data with different random noise seed per each c_0). 1 *Deconv* IFU data is produced per each *Conv* IFU data with a fixed $N_{iter} = 20$. In total, 216 *Free* cube, 1,620 *Conv* cubes, and 1,620 *Deconv* cubes are produced as Group 2.

Lastly, we produce Group 3 data using a range of mock galaxy model parameters as in Table 2.2. This is to verify the performance of deconvolution in more diverse combination of galaxy photometric and kinematic distributions. 40,000 sets of galaxy model parameters are determined randomly (Monte-Carlo), and 1 *Free*, 1 *Conv*, 1 *Deconv* mock IFU is generated for each set. In total, 40,000 *Free* cubes, 40,000 *Conv* cubes, and 40,000 *Deconv* cubes are produced as Group 3.

2.3.3 Kinematics Measurement and Rotation Curve Model Fitting

We use an IDL version of the Penalized-Pixel Fitting (pPXF)(Cappellari & Emsellem 2004; Cappellari 2017) procedure to extract the Line-Of-Sight-Velocity-Distribution (LOSVD) from the mock IFU data. To minimize the pPXF computation time, we use the identical model SEDs to the ones we used for the mock generation, and fit only the velocity and the velocity dispersion without any additive or multiplicative Legendre polynomials or high-order kinematics. Following the recipe from Cappellari (2017), 1) we match the spectral resolution of the model SED to that of the mock IFU data,

Table 2.1. Mock Cube Parameters (Group 1 and 2)

Parameter	Value
IFU field of view ($''$)	32
Redial coverage (R_e)	2.5
S/N at $1R_e$	10, 20, 30
Sérsic index	1, 4
Inclination ($^\circ$)	40, 55, 70
Position Angle ($^\circ$)	15
V_{ROT} (km/s)	200
R_1 ($''$)	1, 2, 3, 4
$1/R_2$ ($1/''$)	-0.05, 0, 0.05
σ_0 (km/s)	150
FWHM coefficient c_0 ($''$)	2.6 (Group 1) 2.3, 2.6, 2.9 (Group 2)
FWHM coefficient c_1 ($\times 10^{-5}$ $''$/Å)	-1.2
Redshift	0.02

Note. — S/N at 1 R_e is defined as median S/N of a spaxel around 1 R_e per spectral element. When values of a parameter are listed with comma, one of the value is randomly selected. When values of a parameters is given in range (with hyphen), value is selected randomly within the range.

Table 2.2. Mock Cube Parameters (Group 3)

Parameter	Value
IFU field of view ($''$)	12, 17, 22, 27, 32
Redial coverage (R_e)	1.5, 2.5
S/N at $1R_e$	10 - 30
Sérsic index	1, 4
Inclination ($^\circ$)	10 - 80
Position Angle ($^\circ$)	15
V_{ROT} (km/s)	50 - 300
R_1 ($''$)	1 - 4
$1/R_2$ ($1/''$)	-0.1 - 0.1
σ_0 (km/s)	50 - 300
FWHM coefficient c_0 ($''$)	2.3 - 2.9
FWHM coefficient c_1 ($\times 10^{-5}$ $''$/Å)	-3.6 - 1.2
Redshift	0.02

and 2) we de-redshift the mock IFU data to the rest frame, before extracting the 2D LOSVD. We also masked the wavelength around the known emission lines, although there is no emission line in the mock IFU data. Considering the wavelength coverage of the mock IFU data, we limit the fitting wavelength range as 3700 to 7400 Å for the LOSVD measurement. From the extracted 2D velocity map, we fit the RC model to quantify the shape of the rotation curve following the procedure in subsection 3.3.2.

2.3.4 Results and Discussion

In this subsection, we present the result of the deconvolution test on the mock IFU data. We describe the overall effect of PSF and the deconvolution using mock IFU data of one model galaxy. We show the relation between the restored kinematics and the deconvolution parameters (N_{iter}, $\mathrm{FWHM_{Deconv}}$) and discuss the adequate choice of the deconvolution parameters.

Effects of PSF Convolution and Deconvolution

Figure 2.2 shows the effects of PSF and the deconvolution from one of the Group 3 (Monte-Carlo) mock IFU data ($n_{Sersic} = 1$, $S/N_{1R_e} = 25$, $i = 48°$, V_{ROT}=212 km/s, R_1=3.7″, $1/R_2$=0.02 (1/″), σ=74 km/s, $\mathrm{FWHM_{PSF}}$=2.88″, field of view = 32″), as an example. Panels on the leftmost column show the quantities measured or extracted from the *Free* IFU data. The quantities perfectly agree with the 2D photometric and kinematic distributions which we put into the mock, meaning that the mock IFU data is constructed accurately in accordance with the model parameters. The second left column presents distributions from *Conv* IFU data. The effects of PSF convolution on its flux, velocity, and velocity dispersion distribution are noticeable. Their difference with respect to the leftmost column panels are presented in the second right column. The flux and velocity distributions are smoothed with PSF relative to those of the *Free* IFU data. by the effect of PSF. The $\mathrm{Flux_{major}}$ and $\mathrm{V_{major}}$ difference profiles show evident deviation between the *Conv* and the *Free*. Especially, the characteristic radius of the rotation curve (R_1, measuring the size of the inner linear part) is increased after

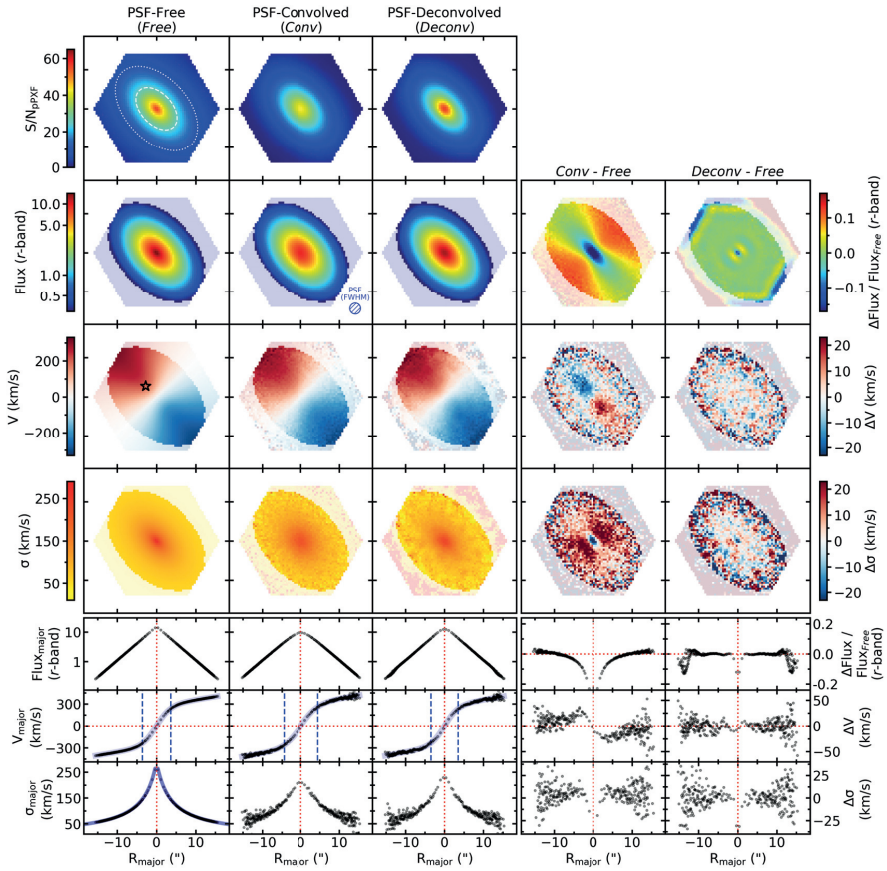

Figure 2.2. Effect of the PSF convolution and deconvolution of the S/N, r-band flux, line of sight velocity (V), and velocity dispersion (σ) on the 2D map and the major-axis profile are shown. The first, second, and third columns represent data from PSF-Free (*Free*), PSF-Convolved (*Conv*), and PSF-Deconvolved (*Deconv*) of one of the Monte-Carlo mock IFU data (see text). The fourth and fifth columns show a difference between the *Conv* to the *Free* and the *Deconv* to the *Free*. The size of the major tick in the maps is 10″. Dashed (Dotted) ellipses over-plotted on the top left corner panel denotes $1R_e$ ($2R_e$). FWHM of the convolved PSF is shown as a blue hatched circle in the Flux - *Conv* panel. Black open star on V - *Free* panel is the location of the example spectrum in Figure 2.3. Spaxels with S/N < 3 are paled out in the 2D maps except for the S/N map. Only data points within $\pm 5°$ of major axis are shown in the radial profiles for clarity. Blue paled-out lines are under-plotted on the V_{major} profiles (*Free*, *Conv*, *Deconv*) and the σ_{major} profile (*Free* only) to represent fitted RC model functions. Blue vertical dashed lines in the V_{major} profiles denote R_1 of the corresponding fitted RC model function.

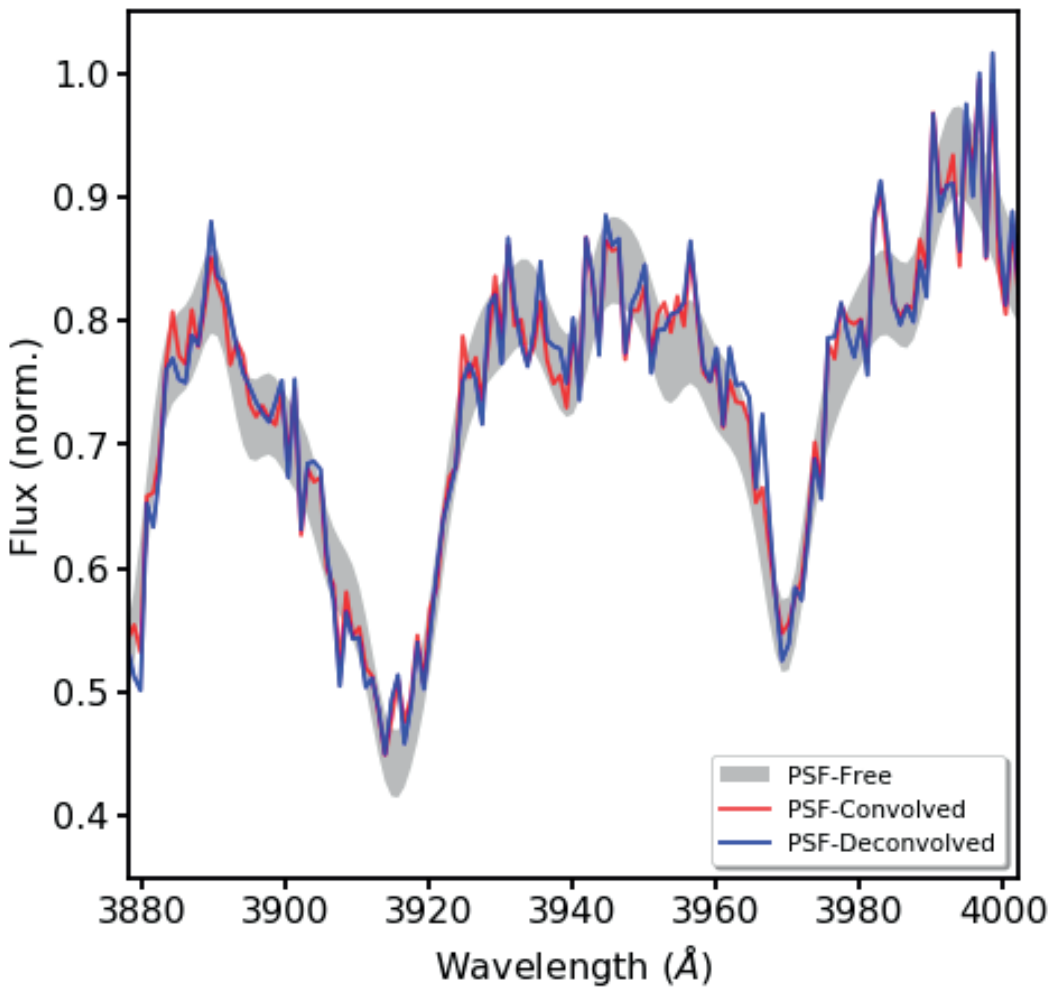

Figure 2.3. Spectrum of the spaxel where the ΔV between the *Conv* and the *Free* is -20 km/s. Only the spectra around the Ca H&K lines are shown. The location of this spaxel is marked as a black open star in Figure 2.2. Median S/N at this spaxel is 36. Each spectrum is normalized by the median of each to show only the difference between spectra in their shape. The thickness of the spectrum from *Free* (grey) represents $\pm 1\sigma$ error at each wavelength bin.

the PSF convolution. The velocity dispersion around the center is increased by the mixture of line of sight velocity distribution around the center, but at the very center, the velocity dispersion is decreased.

The central column presents the distributions from *Deconv* IFU data, and the rightmost column shows the difference between the *Deconv* and *Free*. It is clear that the difference between the *Deconv* and the *Free* is significantly less than that between the *Conv* and the *Free*. Both the apparent b/a ratio of the model galaxy flus is decreased, and the R_1 of the rotation curve is much close to those from the *Free*. The velocity distribution is also much improved. However, the distribution near the edge of the galaxy become fuzzier and show some systematic feature especially in the flux distribution. We put additional examples of Group 1 mock IFU data in section C.2. The examples in section C.2 demonstrate that the deconvolution on IFU data is working effectively well and restores the true distributions of photometric and kinematic properties of the model galaxies.

We visualize the effect of deconvolution in the wavelength dimension. Figure 2.3 shows an example of spectra at the spaxel where ΔV between the *Conv* and the *Free* is about -20 km/s. Because the size of one wavelength bin corresponds to 69 km/s, ΔV of -20 km/s hardly recognized by eyes between the spectra, even around a strong absorption line. It is also noticed that the *Deconv* spectrum is slightly noisier than the *Conv* spectrum. The mean difference between the *Conv* and the *Deconv* spectrum with respect to the *Free* spectrum at this spaxel is 4.0% and 4.6%, respectively. In fact, the noisier *Deconv* spectrum is expected by the effect of LR deconvolution algorithm (noise amplification). Although the *Deconv* spectrum is nosier then the *Conv* spectrum, the overall shape of the *Conv* spectrum has changed by the deconvolution, and the line-of-sight velocity and the velocity dispersion of the *Deconv* spectrum are better recovered to the true value.

Deconvolution Parameters

We investigate the dependence of the restored kinematic quantities on the deconvolution parameters, N_{iter} and $\mathrm{FWHM}_{\mathrm{PSF}}$. Ideally, the deconvolution results should give the

best result when $N_{iter} \to \infty$. However, it is computationally expensive and does not guarantee the best result due to the noise amplification and artifacts caused by the LR deconvolution algorithm. Therefore, it is necessary to investigate the quality of the deconvolution result as a function of N_{iter} In addition, the $\mathrm{FWHM_{PSF}}$ used for the deconvolution would be not be the same as the true one due to the measurement error in practice. Thus, we investigate the dependence of the result on the $\mathrm{FWHM_{PSF}}$ used for the deconvolution as well.

Figure 2.4 represents the difference between the fitted and the true RC model parameter value as N_{iter} increases from 1 to 20. Error bar is calculated from the 25 mock IFU data with different random seeds which we implemented for the noise realization. Since the deviation from the true value depends on the galaxy model parameters, we show the result from multiple model galaxies by using the Group 1 mock IFU data. The figure shows the case of the mock data with $n_{Sersic} = 1$, 4 and $i = 40$, 55, 70°. The difference between the parameters from the *Conv* (arrows at the $N_{iter} = 0$) and the true value is evident. As N_{iter} increases, the difference between the parameters from the *Deconv* (open circles) and the true value decreases. However, small offsets from the true values remain even at $N_{iter} = 20$. The offsets are larger when $n_{Sersic} = 4$, compared to those when $n_{Sersic} = 1$. In general, the deconvolution provides meaningful results even when the noise is considered since the error bars are smaller than the changes caused by the deconvolution. The error bar becomes significant for the lower S/N at 1 R_e, as expected. We conclude that in most cases, the kinematic parameters are reasonably well-restored with $N_{iter} = 20$ when the size of error is taken into account. In subsection C.3.1, we present similar figures with various mock galaxy model parameters to more support the validity of the deconvolution algorithm.

Figure 2.5 presents the difference between the fitted RC model parameter and the respective true value as $\mathrm{FWHM_{Deconv}}$ changes from 2.3″ to 2.9″ with 0.05″ intervals when $\mathrm{FWHM_{Conv}} = 2.6''$ and N_{iter}=20. Again the error bar is calculated from the result with 25 mock IFU data generated by different random seeds. The figure shows the case of the mock data with $n_{Sersic} = 1$, 4 and $i = 40$, 55, 70°. Indeed there is a

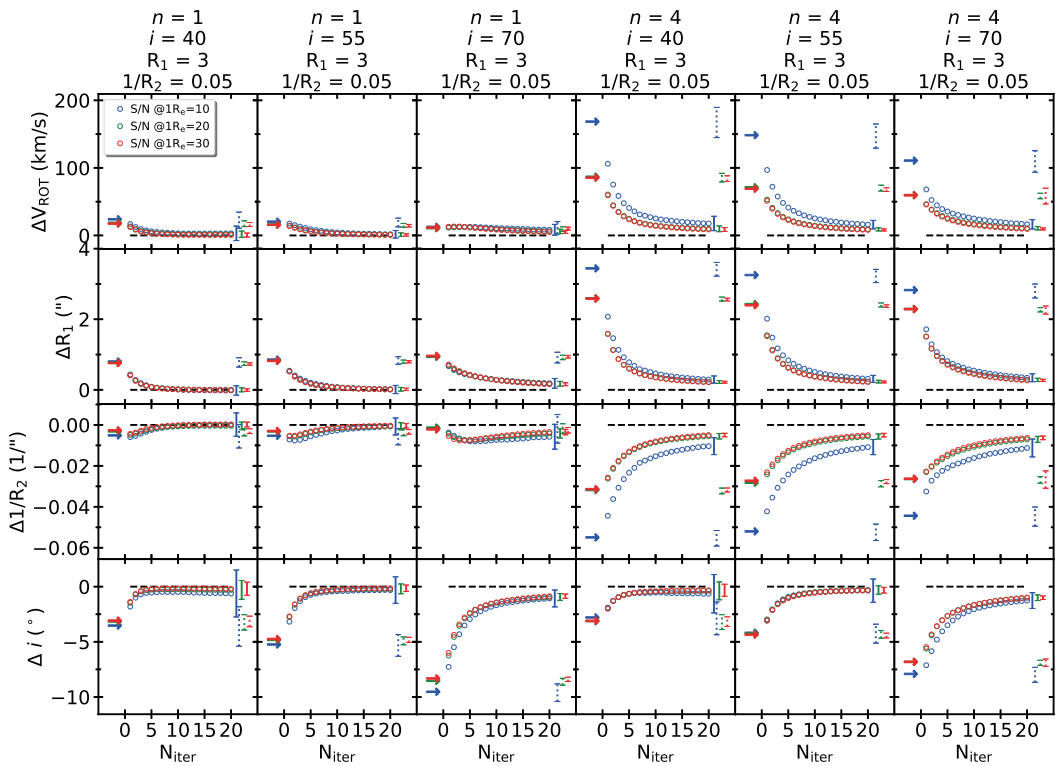

Figure 2.4. Difference between the fitted and the true model RC parameters with respect to the number of LR deconvolution iteration. Each column shows the results from the mock cube with different n_{Sersic} and i. Differences are plotted as open circles. Color represents S/N at 1 R_e of the corresponding *Free* mock cube. Black dashed line represents the fitted parameter value from the *Free* mock cube, which is identical to the true model parameter. Color arrows points out the value of the fitted parameters of the *Conv* mock cube. Error bar denotes median error of the fitted parameters.

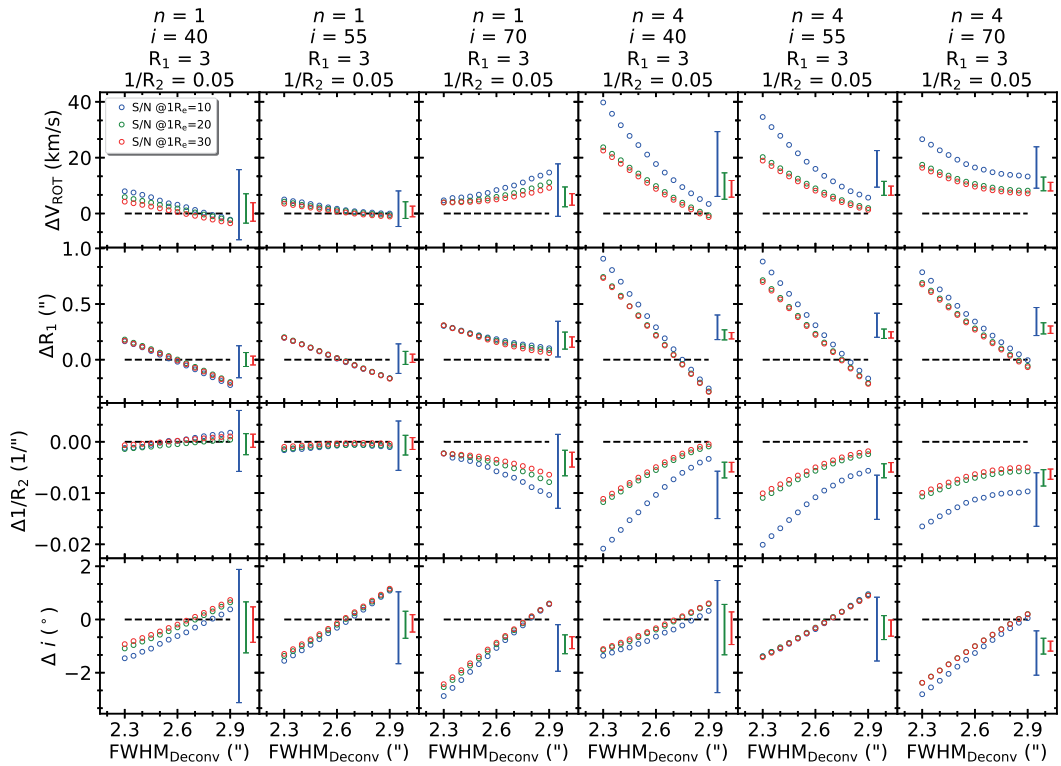

Figure 2.5. Difference between the fitted and true model RC parameters with respect to the FWHM of PSF used for the deconvolution (N_{iter}=20). The size of the PSF convolved to the *Free* mock cube is 2.6″ in FWHM. Each column shows the result from the mock cube with different n_{Sersic} and i. Differences are plotted as open circles. Color represents S/N at 1 R_e of corresponding *Free* mock cube. The Error bar denotes the median of the fitted parameter errors at each $\mathrm{FWHM_{Deconv}}$.

dependence of the fitted parameters to the $\mathrm{FWHM_{Deconv}}$ value, but its variation is not significant when the $|\mathrm{FWHM_{Deconv}} - \mathrm{FWHM_{Conv}}| < 0.2''$, considering the error bar. As the $\mathrm{FWHM_{Deconv}}$ increases, the difference between the parameters from the *Deconv* (open circles) to the true value varies but not quite linearly. Considering all four kinds of fitted parameters, the best result is obtained when $\mathrm{FWHM_{Deconv}} = \mathrm{FWHM_{Conv}}$, although the difference between the fitted and the true model parameters from the *Deconv* and the *Free* is not minimum at $\mathrm{FWHM_{Deconv}} = \mathrm{FWHM_{Conv}}$. We conclude that in most cases, the deconvolved IFU data produces a consistent result when the $\mathrm{FWHM_{PSF}}$ measurement error is less than $0.2''$. In subsection C.3.2, we present supplementary figures with different $\mathrm{FWHM_{Conv}}$ values ($2.3''$ and $2.9''$) and different mock galaxy model parameters.

Results from the Monte-Carlo Mock Cubes

We present the result with Group 3 Monte-Carlo mock IFU data. This is to validate the deconvolution method with diverse combination of the galaxy model parameters. We divide the results according to n_{Sersic} since the results are highly correlated with n_{Sersic}. Figure 2.6 and Figure 2.7 shows the results with $n_{Sersic} = 1$ and $n_{Sersic} = 4$, respectively. We only include the results when the data from *Deconv* cube satisfies the fit qualification criteria, $R_{major,S/N>3}/R_1 > 3''$ and $70^\circ > i > 20^\circ$. In Figure 2.6, all V_{ROT}, R_1, $1/R_2$ and i measured from the *Deconv* cubes show good agreement with the true value. On the contrary, R_1, and i measured from the *Conv* cubes show significant deviations from the true value. V_{ROT} and $1/R_2$ from the *Conv* cubes show much less offsets from the true values. In Figure 2.7, again all parameters measured from the *Deconv* cubes show good agreement with the true value. However, the parameters measured from the *Conv* cubes show significant deviations for all parameters.

Results from the figures show that the deconvolution successfully restored the true kinematic properties of galaxies in each sample. It also shows that the measured parameter values from the *Conv* cube show a noticeable deviation from the true value, especially when $n_{Sersic} = 4$. It can be interpreted that the PSF convolution effect

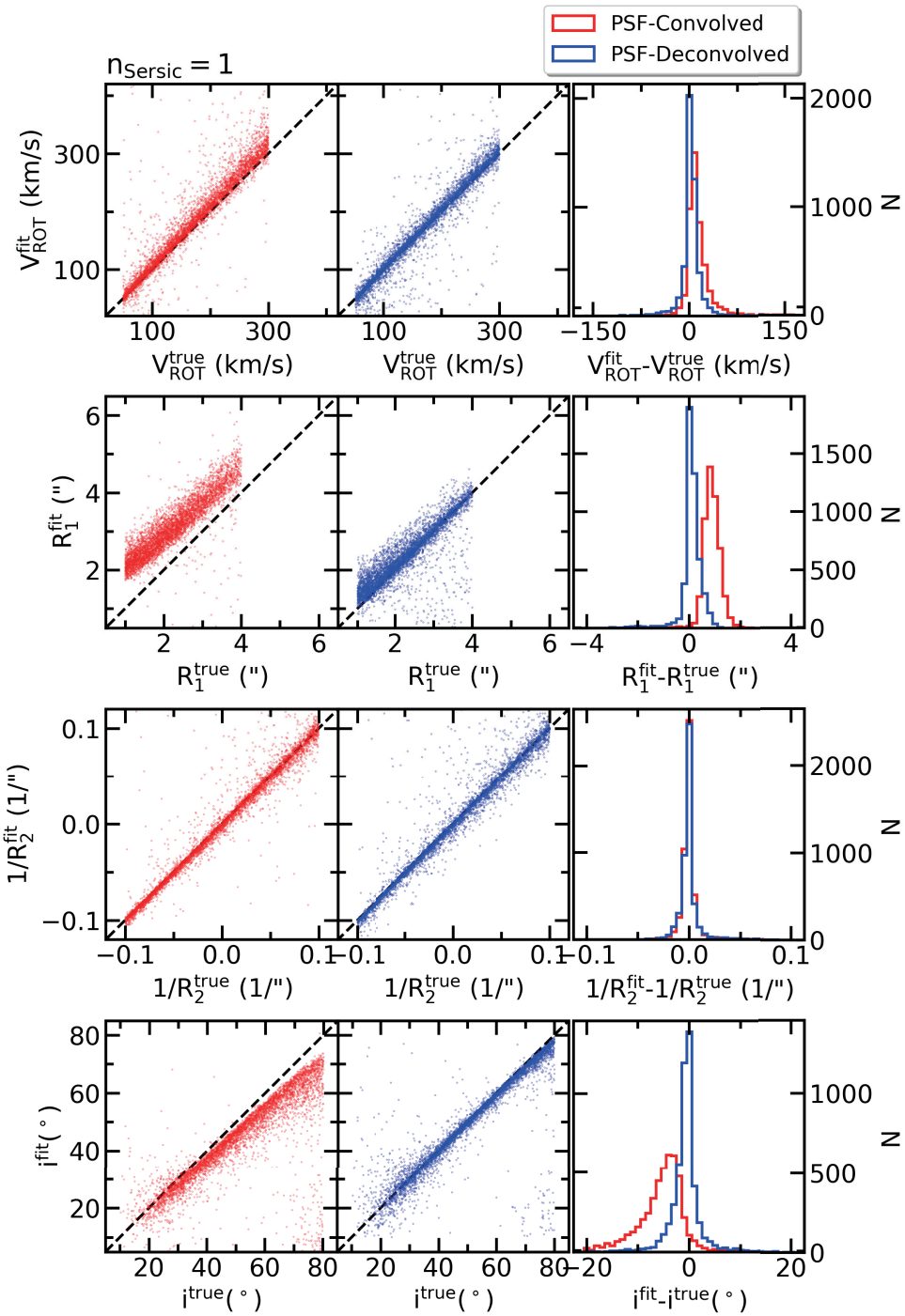

Figure 2.6. 1:1 relation of fitted RC model parameters between *Conv*-true and *Deconv*-true when $n_{Sersic} = 1$

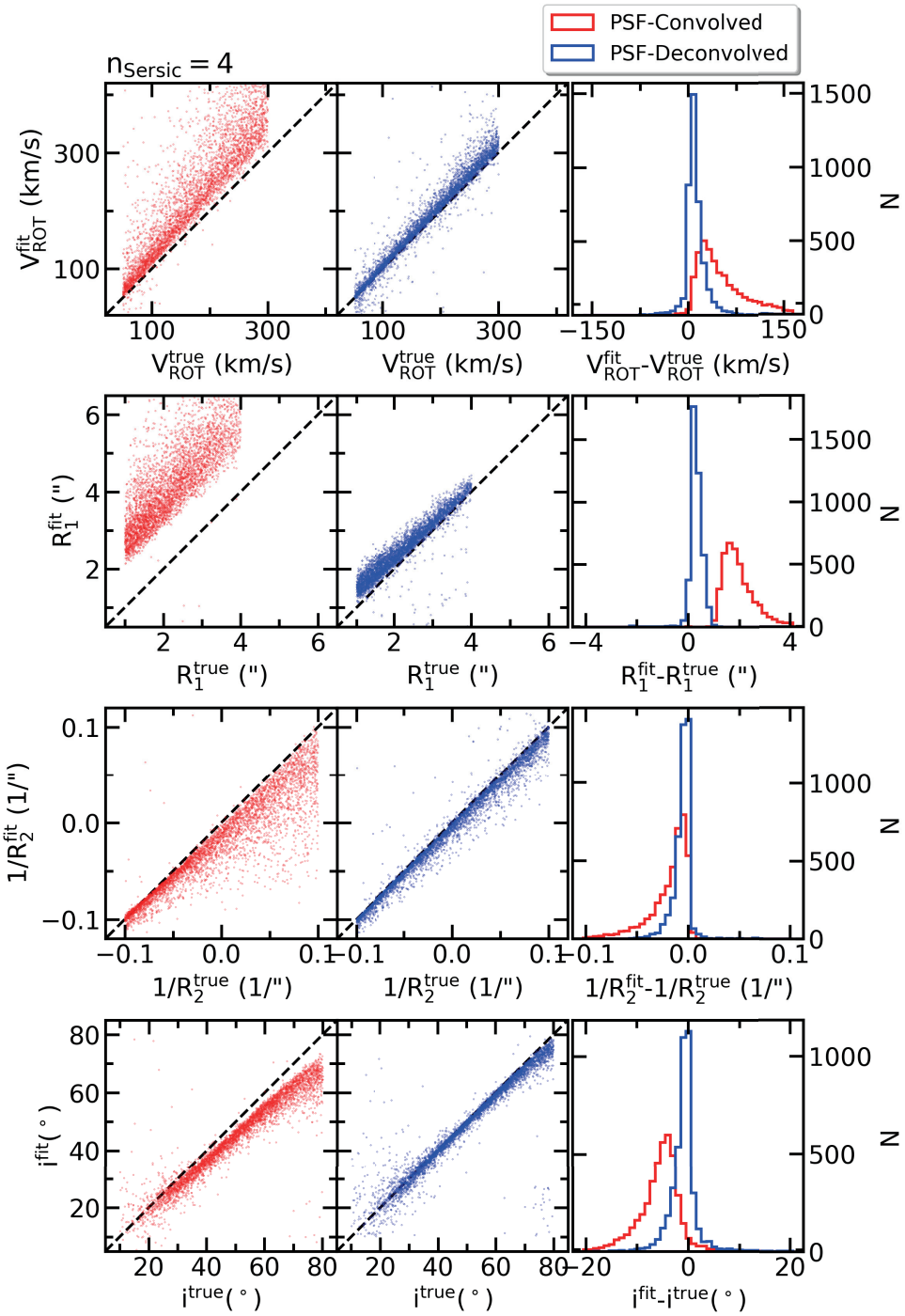

Figure 2.7. 1:1 relation of fitted RC model parameters between *Conv*-true and *Deconv*-true when $n_{Sersic} = 4$

becomes more significant when there is a larger relative flux difference between the adjacent spaxels. This effect is most evident for R_1 parameter, which is a characteristic scale radius where the RC becomes flat. For example, $R_1^{fit} - R_1^{true}$ for *Conv* show a median offset of 1.8 $''$ in Figure 2.7. This large offset also affects $1/R_2$, where many $1/R_2$ values from *Conv* are measured in the condition where they did not meet the fitting qualification criteria.

2.4 Application to SDSS-IV MaNGA IFU Data

2.4.1 MaNGA Point Spread Function

We use IFU data of 4,425 unique galaxies from the third public release of the MaNGA (Bundy et al. 2015)(see section 1.3), which is a part of SDSS DR15 (Aguado et al. 2019). For the repeated observations, we only use the data with the highest blue channel S/N as recorded in the cube data header. In the context of deconvolution, it is important to have accurate information about the shape and size of PSF in MaNGA data cube. According to the Law et al. (2015, 2016); Yan et al. (2016a), it is known that 1) size of $\mathrm{FWHM_{PSF}}$ ranges between 2.2 - 2.7 $''$ in g-band, 2) the shape of PSF is well-described by a single 2D Gaussian function, 3) FWHM of the fitted model Gaussian function agrees with the measured value within 1 - 2%, 4) $\mathrm{FWHM_{PSF}}$ varies less than 10% across the field of view of a given IFU. MaNGA date cube provides the reconstructed MaNGA PSF image in *griz* band as well as their $\mathrm{FWHM_{PSF}}$ values in the header. The distribution of the g-band $\mathrm{FWHM_{PSF}}$ is shown in the left panel of Figure 2.8. To account for the wavelength dependence of MaNGA $\mathrm{FWHM_{PSF}}$ (Figure 2.8, middle panel), we fit a simple linear function (first order polynomial) to the $\mathrm{FWHM_{PSF}}$ in *griz*-bands to interpolate/extrapolate the FWHM at a different wavelength. The average absolute difference between the reconstructed $\mathrm{FWHM_{PSF}}$ and the value from a linear function is less than $0.01''$ for 75%, and $0.02''$ for 95% of the entire MaNGA galaxies. Considering the error of the reconstructed $\mathrm{FWHM_{PSF}}$ (1-2%)(Law et al. 2016), we conclude that the $\mathrm{FWHM_{PSF}}$ from the fitted linear function gives reasonable $\mathrm{FWHM_{PSF}}$ at each

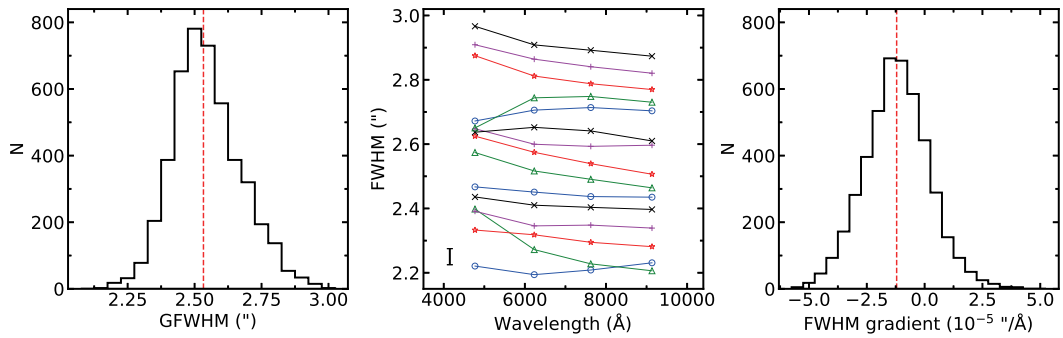

Figure 2.8. (left) Distribution of reconstructed FWHM in g-band. Median value is 2.53 $''$. (middle) Wavelength-dependent $\mathrm{FWHM_{PSF}}$ of the selected MaNGA galaxies. Each connected line represents $griz$ FWHM of PSF from a particular sample. Samples are randomly selected for illustrative purpose. Error bar denotes 1% of 2.5$''$ range. (right) Distribution of wavelength-dependent FWHM gradient. The gradient is obtained by fitting a linear function to the reconstructed FWHM at $griz$-bands. Median value is $-1.21 \times 10^{-5}''/\text{Å}$.

wavelength bin. The distribution of the slope of linear functions is shown in the right panel of Figure 2.8.

2.4.2 Measurements of Kinematic Parameters

We extract the line-of-sight velocity and the velocity dispersion from 4,824 MaNGA galaxies. The procedure is similar to what we described in subsection 2.3.3 with some differences. We use 156 single-stellar population model templates from MILES stellar library (Sánchez-Blázquez et al. 2006; Falcón-Barroso et al. 2011; Vazdekis et al. 2010) using unimodal initial mass function (Vazdekis et al. 1996) and Padova+00 isochrones (Girardi et al. 2000), age from 1 to 17.78 Gyr, metallicity (Z) from -2.32 to 0.22 (26 ages $\times$ 6 metallicites = 156). We use the 6^{th} order additive and multiplicative Legendre polynomials during the fitting to account for the low-order difference and offset between the MILES model and data. We mask the spectrum pixels around the known emission lines and the pixels which are flagged as DONOTUSE by the MaNGA Data Reduction Pipeline (Law et al. 2016). Model SED templates are convolved with a Gaussian function to match the spectrum resolution of MaNGA data as provided in the SPECRES

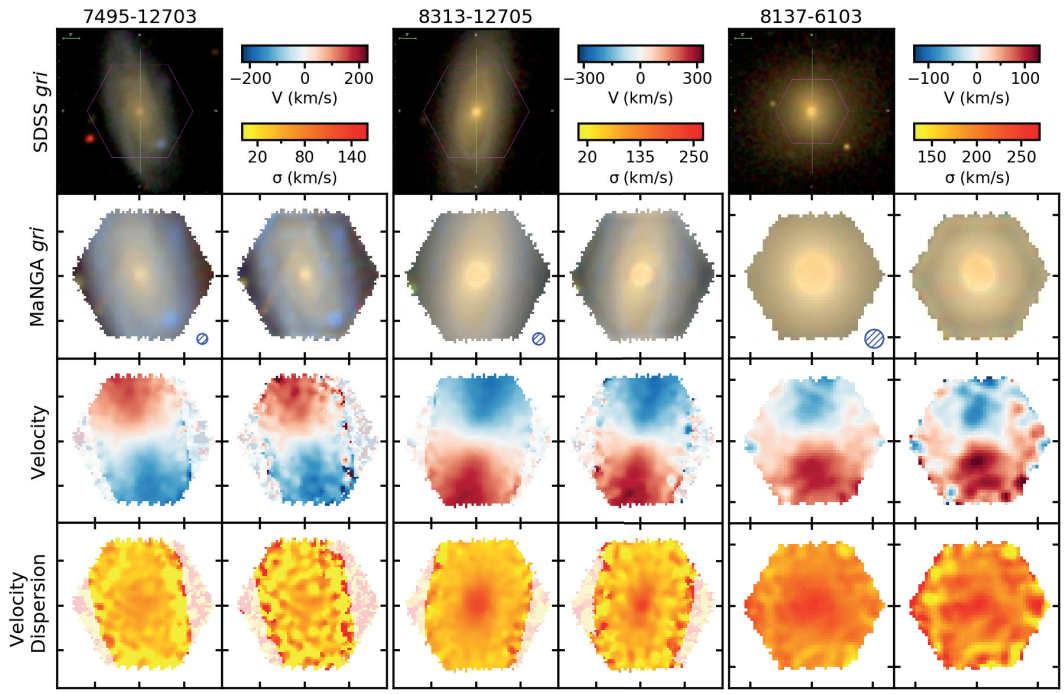

Figure 2.9. Examples showing the effects of the PSF deconvolution on three MaNGA galaxies. The number above the each SDSS *gri* image is the PLATE-IFU designation of a given galaxy. For each galaxy, images in the left column show reconstructed MaNGA *gri* image, velocity and velocity dispersion distribution obtained from the *original* MaNGA data. Images in the right column are the same of those in the left column but from the $PSF-deconvolved$ MaNGA data. Hatched blue circles represent FWHM of PSF on each galaxy. Spaxels with median $S/N_{pPXF} < 3$ are paled out in the velocity and velocity dispersion distributions.

HDU.

2.4.3 Results

Figure 2.9 shows the result of deconvolution applied to three galaxies. The reconstructed *gri* images show a noticeable difference from the image from the original MaNGA (*Ori*) Deconvolution sharpens the image, and restores some substructures which have been seen in the SDSS *gri* image. The velocity distribution also shows the apparent change, especially around the center of galaxies (i.e. the velocity gradient becomes steeper).

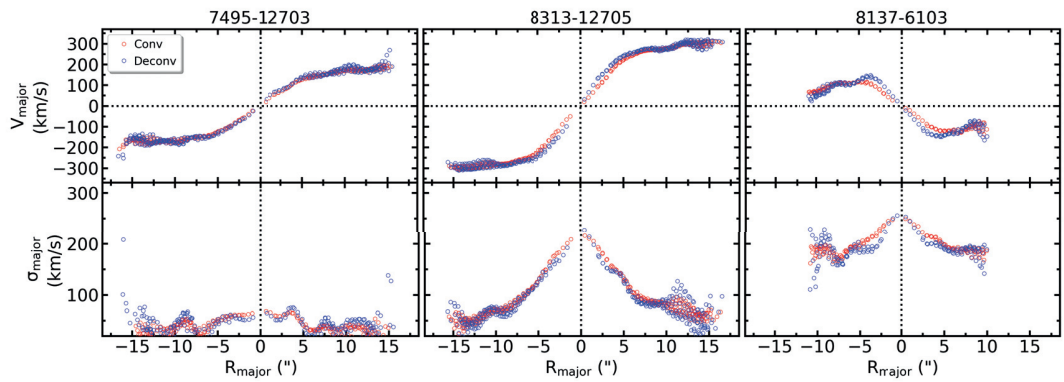

Figure 2.10. The velocity and velocity dispersion profile from the original and deconvolved MaNGA data. Only the data points from $\pm 10^{\circ}$ of the major axis with median $\mathrm{S/N_{pPXF}} > 3$ are shown for clarity.

The velocity dispersion exhibits some changes as well, and shows narrower dispersion distribution near the center and sharper substructures. The restored substructures can be understood intuitively as a result of deconvolution. The difference between MaNGA-*Ori* and MaNGA-*Deconv* data can be seen more prominently in Figure 2.10. The figure clearly exhibit the changes in the velocity and the velocity dispersion distribution along the galaxy major axis.

2.5 Measurement of the Spin Parameter

In this section, we investigate the effect of the deconvolution to measurement of the λ_R parameter. λ_R is a proxy of the spin parameter λ, calculated by the luminosity-weighted first and second velocity moments (Emsellem et al. 2007). The formula given in Emsellem et al. (2007) is

$$\lambda_R \equiv \frac{\langle R|V|\rangle}{\langle R\sqrt{V^2+\sigma^2}\rangle} = \frac{\Sigma_{i=1}^{N} F_i R_i |V_i|}{\Sigma_{i=1}^{N} F_i R_i \sqrt{V_i^2+\sigma_i^2}} \tag{2.3}$$

where F_i, R_i, V_i, σ_i are the flux, the radius of a concentric ellipse, the line-of-sight velocity and the line-of-sight velocity dispersion at the ith spatial bin. λ_R is widely used in various application, such as kinematic classification of galaxies (Emsellem et al. 2011;

van de Sande et al. 2017; Cortese et al. 2016; Graham et al. 2018), the angular momentum of merger remnants (Jesseit et al. 2009), environmental dependence of spin (Greene et al. 2018; Lee et al. 2018), and the evolution of spin parameter using simulation data (Choi & Yi 2017; Choi et al. 2018). Typically λ_R is measured up to the half-light radius (equivalent to the R_e^{major})(Hopkins et al. 2010; Cappellari et al. 2013), and denoted as $\lambda_{\mathrm{R_e}}$. $\lambda_{\mathrm{R_e}}$ is mainly correlated with two parameters: inclination angle (ϵ, as axis ratio) and $\mathrm{FWHM_{PSF}}$, because these parameters affect the distribution of F_i, R_i, V_i, and σ_i. Effect of the PSF can be easily noticed in Figure 2.2.

There were attempts to mitigate the effect of the PSF on $\lambda_{\mathrm{R_e}}$ measurement by correcting $\lambda_{\mathrm{R_e}}$ by $1/\sqrt{\epsilon}$ (Emsellem et al. 2011; Cortese et al. 2016; Greene et al. 2018) or by applying an empirical correction function (Graham et al. 2018)(hereafter G18). We measure $\lambda_{\mathrm{R_e}}$ from the Monte-Carlo mock data cubes (*Free*, *Conv*, *Deconv*) and examine whether or not the deconvolution can restore the true $\lambda_{\mathrm{R_e}}$ value. We also check the feasibility of the G18 correction by using our mock data. Finally, we compare the $\lambda_{\mathrm{R_e}}$ measured from the MaNGA-*Ori* cube and MaNGA-*Deconv* cube and check the amount of change caused by the deconvolution.

2.5.1 Application to Mock Data

$\lambda_{\mathrm{R_e}}$ is calculated from the reconstructed r-band flux, the velocity and the velocity dispersion derived from the *Free*, *Conv*, *Deconv* Monte-Carlo mock data cubes (10,000 cubes each)(see subsection 2.3.1 and Table 2.2). Concentric elliptical radius at each spaxel is calculated from the geometrical parameter of the *Free* cube. Figure 2.11 shows the distribution of $\Delta\lambda_{\mathrm{R_e}}$ from the *Conv* and the *Deconv* with respect to the *Free*. We also calculate the corrected $\lambda_{\mathrm{R_e}}$ from the $\lambda_{\mathrm{R_e}}^{\mathrm{Conv}}$ by following the prescription in G18, and plot the distribution of $\lambda_{\mathrm{R_e}}^{\mathrm{G18corr.}}$ - $\lambda_{\mathrm{R_e}}^{\mathrm{Free}}$. We use $n_{Sérsic}^{Free}$, R_e^{Free} and $\mathrm{FWHM_{PSF}}$ at the r-band pivot wavelength (6231Å) for the G18 correction. We divide the result depends on $n_{Sersic} = 1$ or 4, because of its clear dependence on the n_{Sersic}. The left panels show the $\Delta\lambda_{\mathrm{R_e}}$ with respect to the $\lambda_{\mathrm{R_e}}^{\mathrm{Free}}$ separately, and the right panel shows the histogram of $\Delta\lambda_{\mathrm{R_e}}$ together. The result shows that $\lambda_{\mathrm{R_e}}^{\mathrm{Conv}}$ deviates significantly from

the $\lambda_{R_e}^{Free}$ value (median offset is -0.043 for n_{Sersic}=1 and -0.065 for n_{Sersic}=4). On the other hand, the λ_{R_e} measured from *Deconv* is strikingly well-restored to the correct value ($\lambda_{R_e}^{Free}$). The median (standard deviation) of $\Delta\lambda_{R_e}^{Deconv}$ is -0.001 (0.014) for the $n_{Sersic} = 1$, and 0.002 (0.019) for $n_{Sersic} = 4$. $\lambda_{R_e}^{G18\ Corr.}$ is also well restored for the $n_{Sersic} = 1$ case (median offset is 0.004 and standard deviation is 0.028), but not very well for the $n_{Sersic} = 4$ case (median offset is 0.049).

2.5.2 Application to MaNGA Data

We investigate the change in λ_{R_e} induced by the deconvolution. From the 2D velocity and the velocity dispersion (subsection 2.4.2) along with the reconstructed MaNGA *r*-band flux, we calculate λ_{R_e} of 4,425 MaNGA galaxies (subsection 2.4.1). We use 'NSA_ELPETRO_BA', 'NSA_ELPETRO_PHI', 'IFURA/IFUDEC' and 'OBJRA/OBJDEC' in the FITS header of each galaxy cube data to evaluate the concentric ellipse. To ensure the quality of measured λ_{R_e}, we did not include the spaxels with 1) median $S/N_{pPXF} < 3$, or 2) flagged as 'DONOTUSE' by the MaNGA Data Reduction Pipeline in the λ_{R_e} calculation. When the number of spaxels which fall on those criteria exceeds 10% of the total number of spaxels within $1R_e$, we do not use λ_{R_e} for the further analysis. These criteria would be sufficient to observe the impact of deconvolution on λ_{R_e} for the real data. We note that more strict quality control criteria should be applied for the detailed analysis using λ_{R_e} (Lee et al. 2018; Graham et al. 2018).

We present the relation between the $\lambda_{R_e}^{Ori}$ and the $\lambda_{R_e}^{Deconv}$ in Figure 2.12. Compare to the $\lambda_{R_e}^{Ori}$, most of the $\lambda_{R_e}^{Deconv}$ values shows positive change with maximum $\lambda_{R_e}^{Deconv} - \lambda_{R_e}^{Ori} = 0.2$. This is in agreement with the result in Figure 2.11, where the $\Delta\lambda_{R_e}^{Conv}$ always shows negative change after the PSF convolution. In addition, $\Delta\lambda_{R_e}$ caused by the deconvolution in the MaNGA data is comparable to $\Delta\lambda_{R_e}^{Conv}$ in Figure 2.11. Therefore, we expect that λ_{R_e} calculated from the deconvolved MaNGA data would give the value fairly close to the true λ_{R_e} value. We also plot the relation between the $\lambda_{R_e}^{Ori}$ and the corrected λ_{R_e} (following the G18). Compare to the result with the

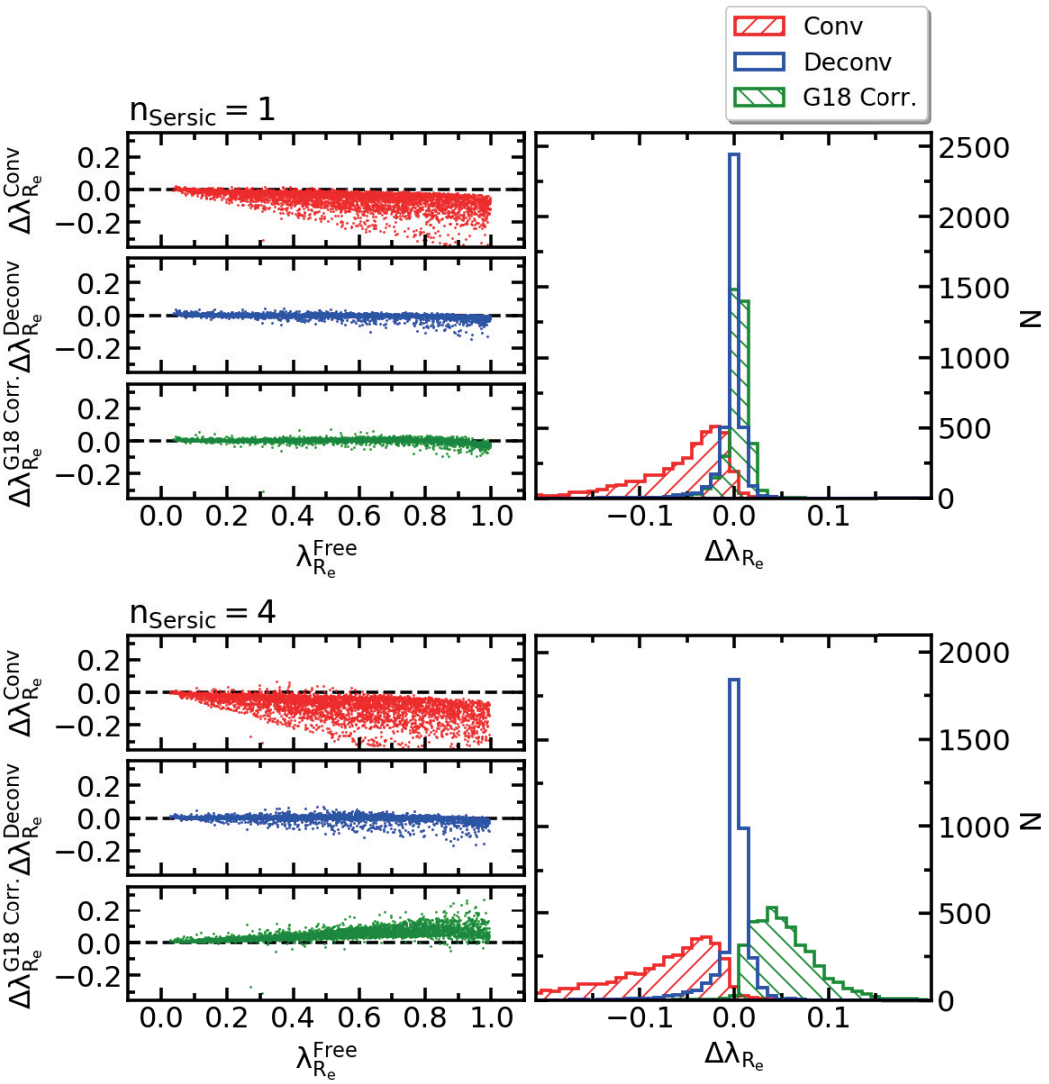

Figure 2.11. Difference between the true and the measured/corrected spin parameter. On the left panel, red (blue) points show the difference between the measured and true spin parameters from PSF-Convolved (PSF-Deconvolved) cube. Green points are corrected values from the spin parameters of PSF-Convolved cubes. (Top) Differences from the model IFU data with $n_{Sérsic} = 1$. (Bottom) Differences from the model IFU data with $n_{Sérsic} = 4$. Right panels show the histogram of the differences. Left panels show the distribution of the difference between the true and

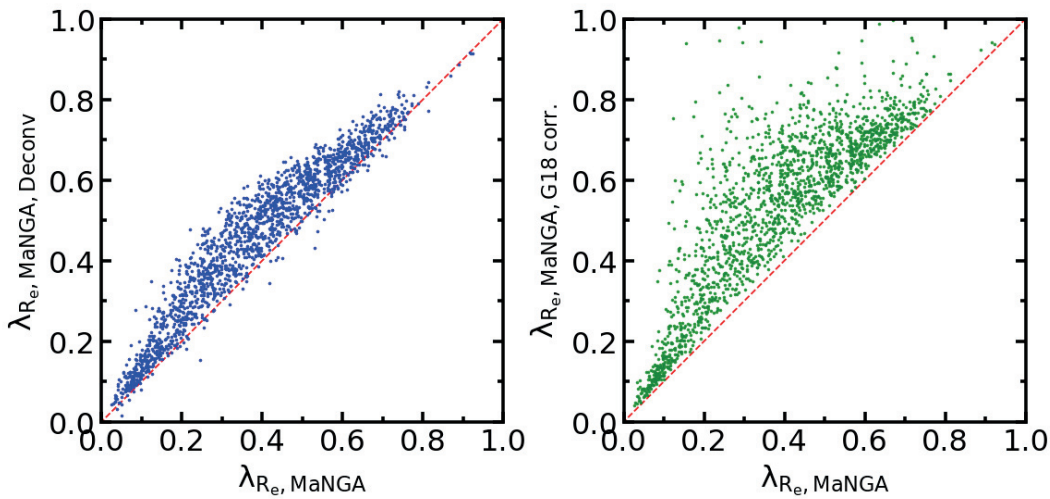

Figure 2.12. (left) λ_{R_e} comparison between measured from original MaNGA cube and deconvolved MaNGA cube. (right) λ_{R_e} comparison between measured from original MaNGA cube and corrected value following G18.

deconvolution, the average amount of $\Delta\lambda_{\mathrm{R_e}}$ caused by the G18 correction is higher. Sometimes the corrected value becomes higher than $\lambda_{\mathrm{R_e}} = 1$ which is nonphysical. Although the usage of analytic correction function is convenient, the result shows that the usage of such a simple function should be used with much caution.

2.6 Summary and Conclusion

We investigate the effects of the PSF Deconvolution by applying the Lucy-Richardson algorithm to the optical integral field spectroscopy data. We develop the procedure to apply the algorithm to MaNGA IFU data, which can deconvolve the given IFU data efficiently using two parameters only (N_{iter} and $\mathrm{FWHM_{PSF}}$). We generate a large number of mock data based on Sérsic profile and the rotation curve model, and use them to confirm that the deconvolution can restore the true kinematics that have been smoothed with the PSF. The deconvolution is powerful in the sense that it can provide an unbiased (model independent) correction to the any PSF-convolved IFU data. We perform the deconvolution to the real data, SDSS-IV MaNGA, and show that

the deconvolution makes a noticeable difference in the 2D flux, the velocity, and the velocity dispersion distribution. Finally, we demonstrate that the λ_{R_e} parameter can be well-corrected to the true value by applying this technique.

Chapter 3

Rotation Curves of Nearby Galaxies and their Environmental Dependence

3.1 Introduction

The galaxy rotation curve (RC) contains information on the various galaxy properties. Early studies lead to the discovery of flat RCs of spiral galaxies, which implies the presence of the dark matter on galaxy scale (Rubin et al. 1980; Bosma 1981a; Persic & Salucci 1988). Subsequent studies discover the relation between the RC and the properties of galaxies such as their kinematic structure, mass, mass profile, morphology, merging feature, etc. Such studies include characterizing the shape of RCs and finding its relation with galaxy properties. It is well known that the inner rise of the RCs are correlated with the light distribution of spiral galaxies (Kent 1987; Corradi & Capaccioli 1990). Swaters et al. (2009) also reported that RC of late-type dwarf galaxies have similar shape with those of late-type spiral galaxies, and the distributions of light at the center of both spiral and dwarf late-type galaxies are correlated with the inner rise of the RC. These results suggest that the gravitational potential at the central region of the galaxies are dominated by the luminous matter. Several studies focus

on the outer shape of the RCs. Sofue et al. (1999) proposed a galaxy classification scheme that uses the shape of the RC at the central region. Avila-Reese et al. (2002) argued the correlation of the outer shape of the RCs with the disk surface brightness, bulge-to-disk ratio, and the dark matter fraction. Noordermeer et al. (2007) found that the curve declining at the intermediate radii, and the decline is stronger for more luminous galaxies, using RCs of 19 early-type disc galaxies. Wiegert & English (2014) classified non-interacting spiral galaxies by parameterizing the shape of RCs, using 79 HI RCs selected from literature. They found that the RCs with the largest rotational velocities have Sb/Sbc morphology on average. However, these previous studies may require further verification because they were done with small galaxy samples, and mostly utilize HI or Hα observation data.

Recently, surveys of the disk galaxies are revealing new relations or supporting the previous findings with larger galaxy samples. DiskMass Survey (Bershady et al. 2010) observed disk galaxies with integral field units (IFUs) to study the dynamical disk-mass surface density, star formation rates, and kinematic/photometric regularity of galaxy disks. They measured Hα velocity fields of 146 galaxies, which include stellar velocity fields of 46 galaxies. They modeled the galaxy RC from the Hα velocity fields with a hyperbolic tangent function. They found a scaling relation between the disk-scale length and the rotation speed (Andersen & Bershady 2013). Kalinova et al. (2017) derived circular velocity curve (CVC) of 238 galaxies from CALIFA survey (Sánchez et al. 2016) by using the Jean-Anisotropic-Modeling method (Cappellari 2008). They performed principal component analysis on the shape of the galaxy CVCs and extracted four principal components. One of their findings is a dependence between the shape of CVC and the galaxy morphology. They found that the galaxies with sharp-peaked CVC mostly have early-type morphology, while the galaxies with slow-rising shape CVS have late-type morphology.

There are a few studies on the relation between the galaxy environment and the RC. Early studies suggest a positive correlation between the outer gradient of RC and the projected cluster-centric radius for the galaxies in cluster environment compare to

the galaxies in field environment (Whitmore 1984; Rubin et al. 1988; Whitmore et al. 1988, using 47 field galaxies and 19 cluster galaxies, both in Hα). They quantify the RC outer gradient as a percentage increase from 0.4 R_{25}[1] to 0.8 R_{25}, normalized to the maximum RC velocity. Their result has been challenged by later studies (Distefano et al. 1990; Amram et al. 1993; Sperandio et al. 1995; Dale et al. 2001; Vogt et al. 2004) which show mild or negligible relation between the outer gradient and the projected cluster-centric radius. Especially, Dale et al. (2001) demonstrated a negligible correlation using 510 cluster spiral galaxy RCs. Instead, they found mild trend between the cluster-centric radius and RC asymmetry parameter[2]. Subsequent studies show that the RC asymmetry parameter is related with galaxy-galaxy interactions (major/minor merger and flyby events), by both observation and simulation (Kronberger et al. 2008; Pedrosa et al. 2008; Bösch et al. 2013). In summary, previous observational studies on the RC shape in the context of the galaxy environment are mostly conveyed by using gas kinematics (Hα) and show that the RC shape seems somewhat correlated with the environment, such as cluster-centric radius and affected by the galaxy-galaxy interaction.

In this chapter, we parameterize the stellar RC of galaxies and explore their dependence on the galaxy properties and the environment. We use an improved RC function which can describe the outer slope of the RCs. This chapter is organized as follows. In section 3.2, we describe SDSS-IV MaNGA survey, galaxy catalogs, and environmental parameters which we employ in this study. We present our RC model and fitting procedure in section 3.3. We show the result of the RC outer slope dependence on the galaxy properties and the environment in section 3.4. We summarize in section 3.5.

[1] R_{25}: the radius at the 25th B mag arcsec^{-2} isophote

[2] The RC asymmetry parameter measures the global RC asymmetry by normalizing the total area between the kinematically folded approaching and receding halves with the average area under the RC

3.2 Data

3.2.1 SDSS-IV MaNGA

SDSS-IV MaNGA survey, one the three core program of the fourth generation Sloan Digital Sky Survey (SDSS) is an IFU survey to observe about 10,000 nearby galaxies during its five-year survey duration. As described in section 1.3, the flat distribution of the MaNGA galaxies in the stellar mass dimension allows to study the mass dependency of the various spatially resolved properties of galaxies with good statistics. Two-dimensional line-of-sight velocity distribution is one of the direct product of IFU data, which allows us to study the kinematics of the galaxies. We use the data from the third data release of the MaNGA survey (Bundy et al. 2015, DR15), which is the latest public release as of June 2019. Among the 4,824 cube data samples of DR15, we exclude non-galaxy observations (136 cubes) and use only unique MaNGA main galaxy samples composed of the Primary, Secondary, and the color-enhanced Primary+ samples. This leaves 4,425 galaxies by excluding some of the galaxies from the ancillary programs and duplicated observations. For the repeated observation data, we first choose the data observed with a bigger IFU, and select the one with the highest blue channel S/N if observed with identical size IFU.

3.2.2 Supplementary Catalogs

KIAS Value Added Galaxy Catalog

For galaxy morphology classification, we use galaxy morphology data from the KIAS value added galaxy catalog (Choi et al. 2010). KIAS VAGC supplements the New York University Value-Added Galaxy Catalog with more redshift from other catalog thus provide better spectroscopic completeness. KIAS VAGC classifies galaxies into early or late morphological types. They use the automated morphology classification scheme developed by Park & Choi (2005) along with the subsequent visual inspection. In addition to the morphological classification with early/late type, we perform morphological classification of $\sim$ 646 selected MaNGA galaxies with T morphological type (T-Type),

following the classification scheme in de Vaucouleurs et al. (1991, Third Reference Catalog of Bright Galaxies) and Nair & Abraham (2010, Table 1)

NASA-Sloan Atlas Catalog

NASA-Sloan Atlas (NSA) provides several useful quantities of local galaxies from SDSS imaging and GALEX ultraviolet imaging survey data. We adopt the latest version (Wake et al. 2017, v1_0_1) of the NSA catalog as the parent catalog of MaNGA galaxies. We use the parameters such as redshift, stellar mass, half light radius ($\lambda_{\mathrm{R_e}}$, effective radius), b/a ratio, position angle, and AB magnitudes with elliptical Petrosian aperture from the NSA catalog.

Bulge+disk decomposition catalog

Simard et al. (2011) perform two-dimensional, point-spread-function-convolved, bulge + disk decompositions in the galaxies from the Legacy area of the SDSS DR7 in g and r band. They fit the 2D galaxy surface brightness fitting with three models, one with a pure Sérsic model, a bulge + disk model with fixed bulge Sérsic index ($n_b = 4$), and a bulge + disk model with free bulge Sérsic index. Disk model is a Sérsic profile with $n_d = 1$. From their catalog, we adopt the bulge to total ratio (B/T ratio) values from the model with bulge+disk model with free bulge Sérsic index, measured in r band.

3.2.3 Environmental Parameters

Large-Scale Background Density Environmental Parameter - ρ_{20}

We use a normalized background mass density $\rho_{20}/<\rho>$ as a large-scale environmental parameter. The detail of calculation of the parameter is described in the Park et al. (2008); Park & Choi (2009, Equation 1), and Song et al. (2016, Appendix). The parameter describes the background density at the location of a target galaxy using the projected distance, morphology, and the luminosity of the 20 closest neighbor galaxies in the volume-limited sample ($0.01 < \mathrm{z} < 0.15$ and $M_r > -20.60$ mag). $<\rho>$ is the

mean mass density within a sample of the total volume: $<\rho> = 0.0223 \pm 0.0005 (\gamma L)_{-20}$, where $(\gamma L)_{-20}$ is the mass of a late-type galaxy with $M_r = -20$ mag.

Small Scale Environmental Parameter - R_n

We use the distance to the nearest neighbor galaxy normalized by the virial radius of the neighbor $\mathrm{R_{dist,n}/r_{vir.,neighbor}} = \mathrm{R_n/r_{vir,n}}$, as a small scale environmental parameter (Park & Choi 2009). The nearest neighbor of a target galaxy is defined as the galaxy with the closest projected distance to a target galaxy among the neighbors which are brighter than $M_{r,target}+0.5$ mag in the absolute magnitude as well as has the line of sight velocity difference less than 600 km $\mathrm{s^{-1}}$ for early-type targets or 400 km $\mathrm{s^{-1}}$ for late-type target galaxies. R_n, the virial radius of the neighbor is defined as the projected radius of the sphere where the mean mass density within the volume becomes 200 times the critical density or 740 times the mean density of the universe (Park & Choi 2009, Equation 5). The virial radii of galaxies defined by the formulae with $M_r = -19.5, -20.0, -20.5$ are 260, 300, and 350 h^{-1} for early type and 210, 240, and 280 h^{-1} for late types, respectively.

3.3 Galaxy Rotation Curve Model

In this section, we present an improved thin-disk RC model to describe the circular rotational motion of galaxies. We also describe a method to fit the model onto a 2D velocity map.

3.3.1 Model

Velocity field of a galaxy is often complex, so the modeling the field is a non-trivial work. According to the previous studies with integral field spectroscopy, S0's and late-type galaxies exhibit the ordered and fast rotation. On the contrary, elliptical galaxies show more complex and dispersion-dominant rotation but still have evidence for ordered rotation (Emsellem et al. 2007; Cappellari et al. 2007, 2011; Emsellem et al. 2011;

Graham et al. 2018). We focus on the ordered rotation of galaxies which can be described by an infinitely thin-disk RC model. There are several functional forms which describe the typical shape of the disk galaxies: an arc tangent (Puech et al. 2008), a hyperbolic tangent (Andersen & Bershady 2013), and an inverted exponential (Feng & Gallo 2011). All these model have a RC converging to a constant velocity at outer radii (beyond the characteristic radius), namely the well-known $flat$ RC. Although it is difficult to describe the complex shape of the real RC in a simple form, we try to improve the current model further but still can be represented by a simple form. We propose the following model which is a combination of the hyperbolic tangent function and a linear term,

$$V(r) = V_{\rm ROT}\ (\tanh(\frac{r}{R_1}) + \frac{r}{R_2}) \tag{3.1}$$

where $V_{\rm ROT}$ is a maximum circular velocity when $1/R_2 = 0$, R_1 is a characteristic radius where the curve slope changes, and $1/R_2$ is the slope of the curve at the outer radii. Figure 3.1 shows an example of this model. The advantage of this model is that it can describe the inclined/flat RC at the outer radius, as well as the rigid body motion near the center of galaxies.

3.3.2 Model Fitting of the 2D Velocity Map

We fit our RC model to the 2D velocity map of a galaxy to describe its kinematics with the RC model parameters ($V_{ROT}, R_1, 1/R_2$) and the kinematic geometrical parameters (center x, center y, position angle and inclination angle). We use the 2D line-of-sight velocity distribution of 4,425 unique MaNGA main galaxy samples, measured in subsection 2.4.2. The procedure uses the minimum χ^2 method which finds a set of parameters minimizing the χ^2 between the model 2D velocity map and the measured 2D velocity map. The following equation describes the 2D model velocity map,

$$V_{\rm obs}(r, \phi) = V_{\rm SYS} + V(r)\, \sin i\, \cos(\phi - \phi_0) \tag{3.2}$$

where r is the distance from the kinematic center of the galaxy to each pixel, determined by the geometrical parameters, $V_{\rm SYS}$ is a systematic velocity of the velocity map, i and

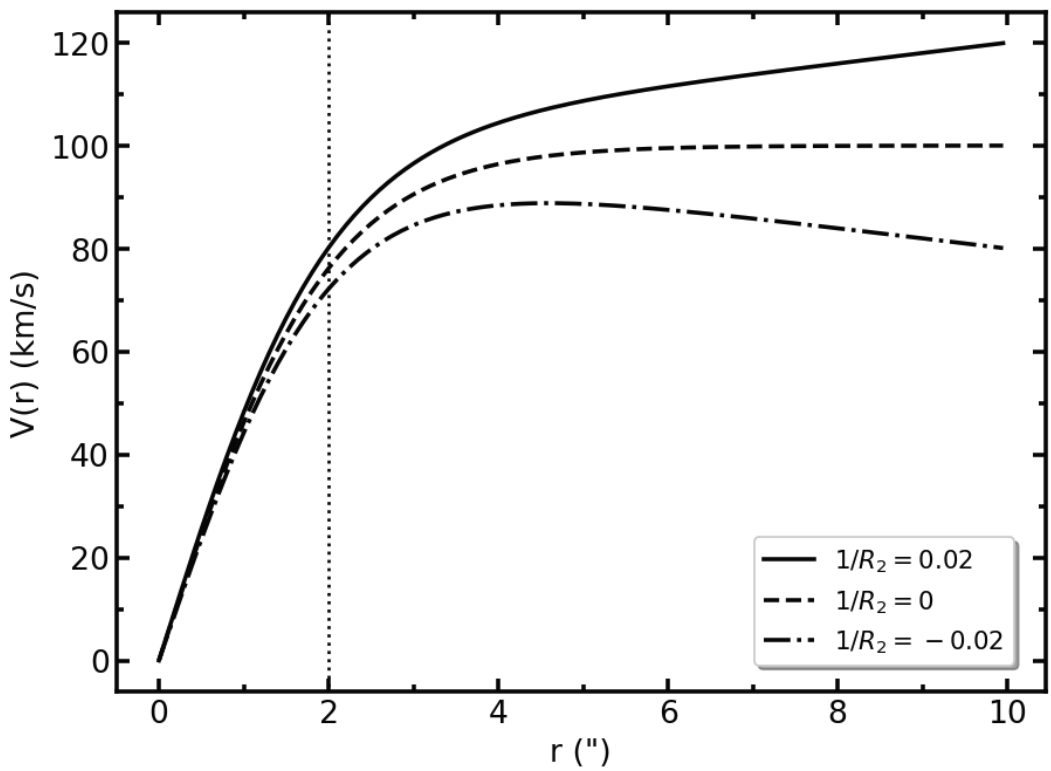

Figure 3.1. Example of rotation curve model. Each line shows different shape at the outskirt described by $1/R_2$ value (when $V_{\rm ROT}$ = 100 km/s and R_1=2″) Vertical dotted line indicates R_1.

ϕ_0 are kinematic inclination angle and the position angle. Including kinematic center position, eight parameters are fitted simultaneously (V_{SYS}, V_{ROT}, R_1, $1/R_2$, i, ϕ_0, x_{cent}, y_{cent}). It is important to provide reasonable initial values of the fitted parameters to fit the model successfully since the minimum χ^2 method becomes sensitive to the initial values when there are many fitting parameters. We find that the fitting result is relatively more sensitive to the geometrical parameters compare to the RC model parameters. We fit the 2D Sérsic model to the reconstructed *gri* images to obtain reasonable initial geometrical parameters. The 2D Sérsic fit is generally less sensitive to the initial parameter, and it gives reasonable initial geometric parameters of a galaxy. One caveat in fitting our RC model is the radial coverage of the 2D velocity map. To have a meaningful $1/R_2$ value, the velocity map should cover a sufficiently large radial range along the major axis compare to the R_1. This is because 1) a $1/R_2$ can not be constrained without the velocity at the outer radii, 2) the velocity at pixels around the minor axis is significantly less sensitive to the RC model due to $\cos(\phi - \phi_0)$ term in Equation 3.2). We check the validity of fitting results by measuring its dependence on radial coverage of the data along the major axis ($R_{max,major}$) relative to R_1. We find that when $R_{max,major}/R_1$ is greater than 3, the fitting results are of good quality. Another caveat for the fitting is the inclination angle. Due to the $\sin i$ term in the Equation 3.2, the RC model cannot be well constrained at a low inclination angle (close to face on). In other words, both RC model parameters and inclination angles are measured incorrectly when the angle is low. The fitting is not well performed for the galaxies with high inclination angle as well, because of the low number of data points and the beam-smearing effect which even remains in the PSF-deconvolved cube. Therefore, we consider fitting result as acceptable when the fitted inclination angle is greater than 20° and less than 70°.

In the following analysis, we use galaxies with late-type morphology. Since our RC model assumes infinitely thin disk, it is not feasible to apply our model to the early-type galaxies. The number of galaxies which satisfies the fore-mentioned conditions ($R_{max,major}/R_1 > 3$ and $20° < \mathrm{i} < 70°$ is 646. Among 646 galaxies, 528 galaxies have

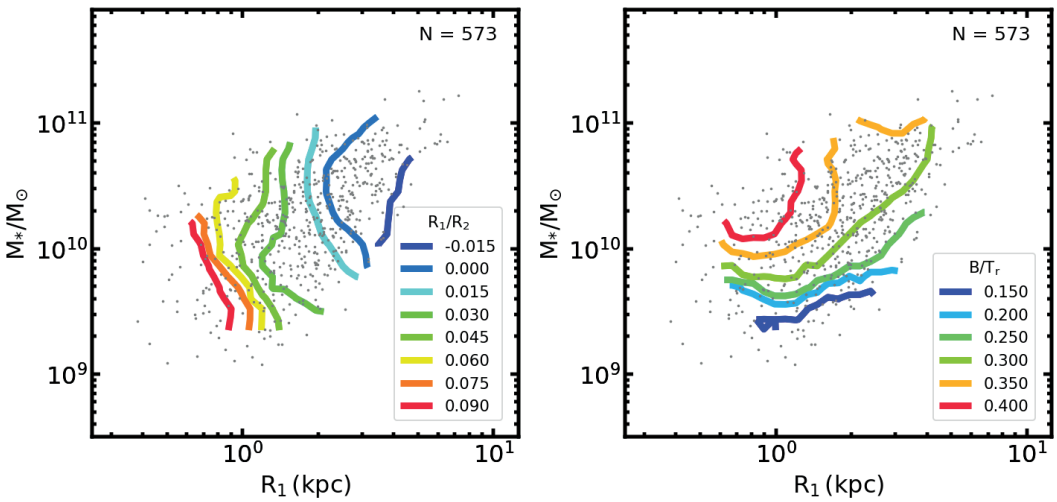

Figure 3.2. RC outer gradient (left) and B/T ratio (right) contours on galaxy stellar mass and RC scale radius R_1.

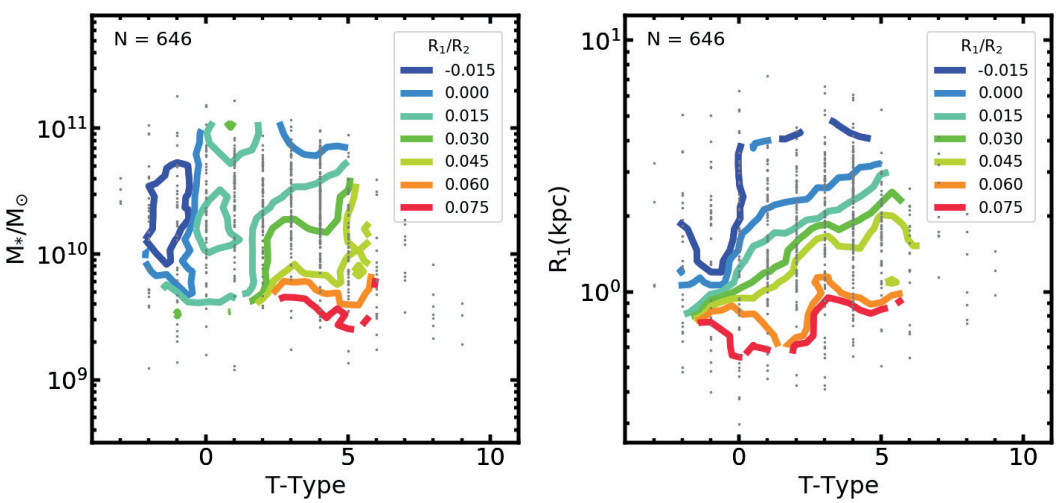

Figure 3.3. RC outer gradient contours on mass and T-Type space, and RC scale radius and T-Type space.

T-Type equal or greater than 0, and 573 galaxies have B/T ratio information.

3.4 Results

3.4.1 Mass and Morphological Dependence

Figure 3.2 shows the dependence of RC slope at outer radii (R_1/R_2) on galaxy stellar mass and RC scale radius (R_1), and bulge to total ratio (B/T ratio) on galaxy stellar mass and R_1. The distribution of data points (grey dots) implies that R_1 and M_* have a positive correlation. To derive the smooth distribution of the R_1/R_2 (and B/T ratio) on the 2D parameter space, we perform following scheme. First, we define 40 by 40 regular grid on the given x-axis and the y-axis range. Second, on each grid point, we give a weight for each data point using spline kernel (Monaghan & Lattanzio 1985, Equation 21, h=smoothing scale) with the distance between grid point and data point in logarithmic scale of x-axis and the y-axis. Applied smoothing scales to the both panels in Figure 3.2 are 0.2 dex and 0.4 dex in the logarithmic scale of R_1 and M_* direction, respectively. The scales are roughly 1/8 of the x-axis or y-axis range in logarithmic scale. The scale is chosen to smooth the contours but also to preserve the features in the contours at the same time. Third, on each grid point, we sort the data points in ascending order and calculate the cumulative distribution of the weights in the same order. Data point value corresponding to the 50% of the summation of all weights is considered as a representative value at the grid point. In Figure 3.2, the contours on the left panel are mostly vertical. This means that R_1/R_2 is highly depend on the R_1 at fixed M_*. The right panel shows that interestingly the iso-B/T ratio contours do not have negative slopes but have positive slopes. The B/T ratio is decreasing with increasing R_1 when the stellar mass is high ($> 2 \times 10^{10} M_\odot$), but at smaller stellar mass the trend is weak and only the dependency of B/T ratio on stellar mass remains. High B/T ratio at small R_1 and high stellar mass means that the galaxies with brighter bulge have a kinematically compact core. This could be evidence for different formation history between bulges of low-mass and high-mass galaxies. The latter may have been

formed by dynamical mergers.

We investigate the correlations between R_1/R_2 and other variables using similar plots in the rest of the analysis by putting the galaxy stellar mass or R_1 on the y-axis. This is to separate the explicit dependence from the implicit dependence. Figure 3.3 shows the dependence of R_1/R_2 on galaxy stellar mass/RC scale radius and T-Type. Applied smoothing scale is 0.4 and 0.2 dex in logarithmic scale of M_* and R_1 respectively, and 1.25 in linear scale of T-Type. On the left panel, when T-type is less than 2 (Sab), R_1/R_2 mostly shows T-Type dependence and has weak or no dependence on stellar mass. On the other hand, when T-type is equal or greater than 2, contours are mostly horizontal, and R_1/R_2 shows only stellar mass dependence. We note that the absent of contours at the low mass & low T-Type region is due to the lack of data points around the region, therefore does not mean that the overall R_1/R_2 value around the region is 0.015. We speculate that this result may implies that formation of S0 (from Sa-Sd) involves sudden dynamical event which ignites kinematic change regardless of their mass, compare to the high-mass spirals which remain their morphological type while gradually gaining their mass. On the right panel, R_1/R_2 shows positive correlation with T-Type at fixed R_1, but only at the intermediate R_1 ($0.8\ \mathrm{kpc} < R_1 < 3\ \mathrm{kpc}$). The correlation becomes weaker at small R_1 (< 0.8 kpc) or at larger R_1 (> 3 kpc). This is consistent with the left panel of Figure 3.2, where the galaxies with low R_1 have high R_1/R_2, and the galaxies with high R_1 have low R_1/R_2. The dependence of R_1/R_2 on T-Type morphology is consistent with Figure 3.4. Applied smoothing scale is 0.4 and 0.2 dex in logarithmic scale of M_* and R_1, respectively, and 0.125 in linear scale of B/T ratio. The B/T ratio can be considered as a quantitative measure of T-Type morphology for the late-type disk galaxies. Unlike T-Type, the B/T ratios have continuous values between 0 to 1. On the left panel of Figure 3.4, B/T ratio exhibits vertical contour around $B/T_r = 0.5$, which would have S0 morphology (T-Type < 1). On the right panel, R_1/R_2 shows negative correlation with B/T ratio at fixed R_1. This could mean that the amount of disk component is related with the increasing RC slope at the outer radii.

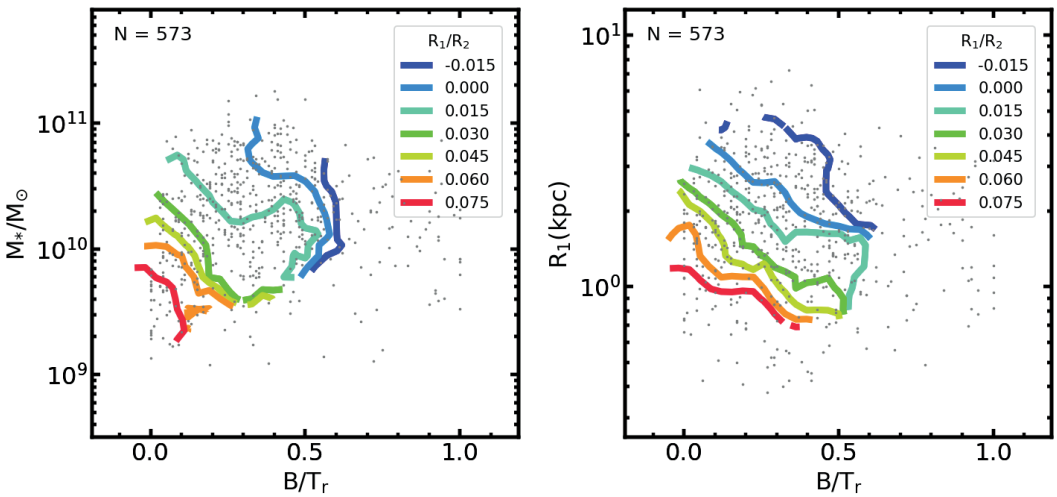

Figure 3.4. RC outer gradient contours on mass and B/T ratio space and RC scale radius and B/T ratio space.

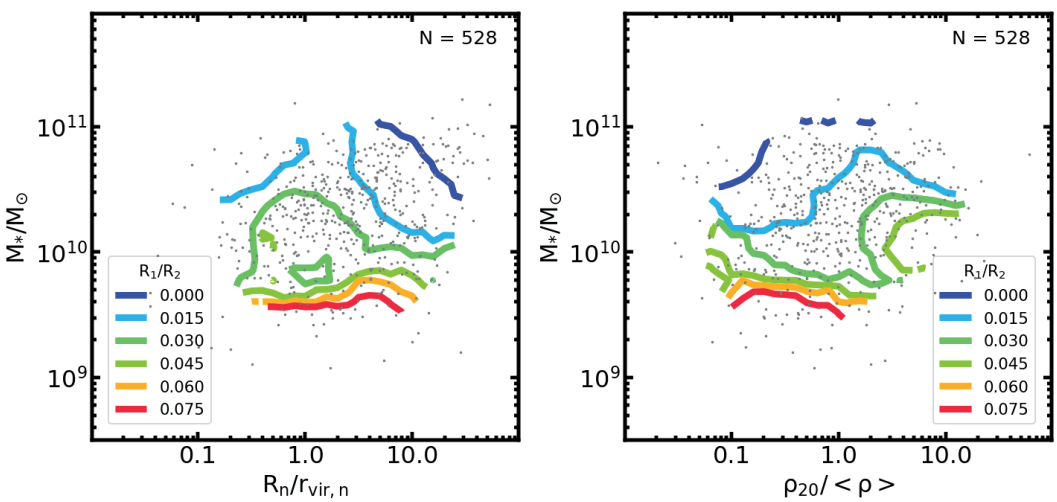

Figure 3.5. RC outer gradient contour on mass and environmental parameters ($R_n/r_{vir,n}$, $\rho_{20}/<\rho>$).

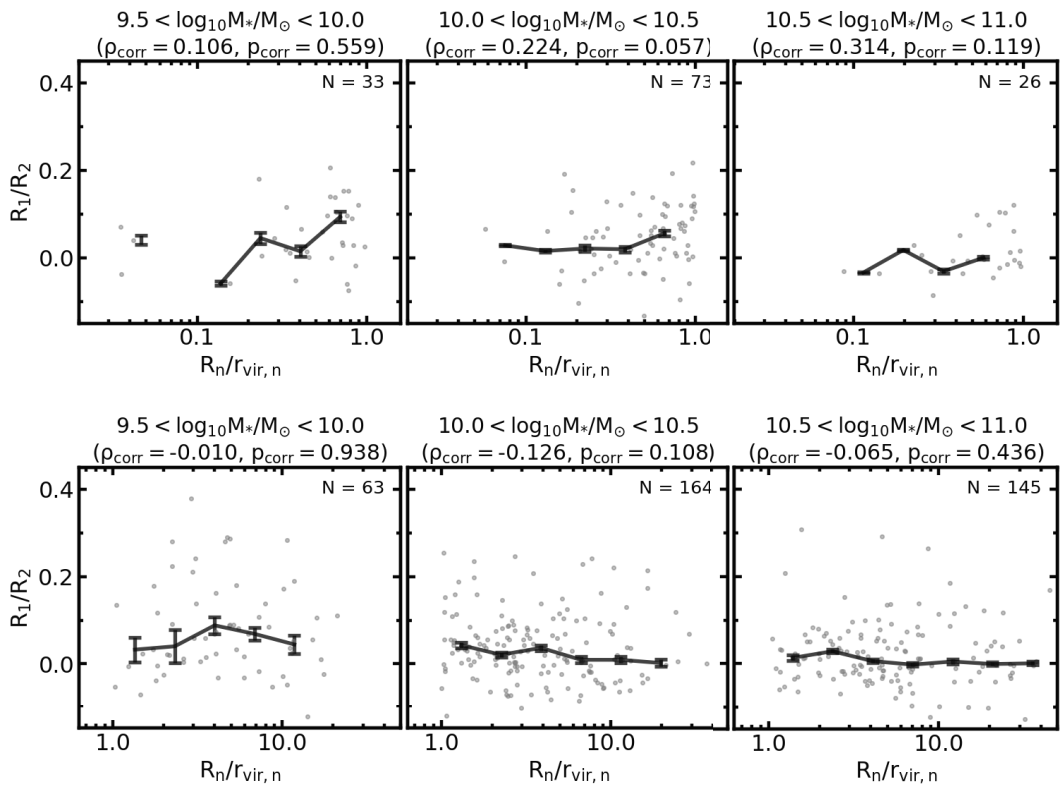

Figure 3.6. Dependence of RC outer gradient on the small-scale environmental parameter ($R_n/r_{vir,n}$). The target galaxies in the left, center, and right panels are limited to their stellar mass ranges of $\log_{10}M_*/M_\odot$ = 9.5-10.0, 10.0-10.5, and 10.5-11.0, respectively. The top (bottom) panels shows the dependence when $R_n/r_{vir,n} \leq 1$ ($R_n/r_{vir,n} > 1$). On each panel, Spearman rank correlation coefficient (ρ_{corr}) and the corresponding p-value (p_{corr}) is shown. The median values of R_1/R_2 are also presented with black solid line.

3.4.2 Environmental Dependence

Figure 3.5 shows the dependence of R_1/R_2 on the stellar mass and environmental parameters (R_n and ρ_{20}). On the left panel, R_1/R_2 shows no dependence on R_n for low-mass galaxies ($M_* < 10^{10}M_\odot$), but exhibits a dependence on R_n for the high-mass galaxies ($M_* \geq 10^{10}M_\odot$). The contours on the right panel show similar shapes but with more complex feature. For the constant stellar mass, R_1/R_2 has negligible dependence on background density when $\rho_{20}/<\rho>$ is less than 1. However, when $\rho_{20}/<\rho>$ is greater than 1, R_1/R_2 shows mild dependence on background density at intermediate mass range ($10 < \log_{10}M_*/M_\odot < 10.5$). To understand the R_1/R_2-environment relation further, we present R_1/R_2 as a function of environmental parameter for three mass bins of $\log_{10}M_*/M_\odot$ = 9.5-10.0 (low), 10.0-10.5 (intermediate), and 10.5-11.0 (high) in Figure 3.6 and Figure 3.7. We also divide the panels according to the environmental parameter range because the correlation exhibited in Figure 3.5 is not entirely linear but shows different trends when the environmental parameter is small or large.

We use Spearman correlation test to measure the amount of correlation between R_1/R_2 and the environmental parameters quantitatively. In Figure 3.6, Spearman coefficients indicate that R_1/R_2 have positive correlation with R_n when $R_n/r_{vir,n} < 1$ in the intermediate and high mass range with 1.9σ and 1.6σ level, respectively. On the other hand, R_1/R_2 shows negative correlation with R_n when $R_n/r_{vir,n} \geq 1$ in the intermediate mass range with 1.6σ level. Other panels have high p-values, therefore do not show noticeable correlation, possibly due to the low number of samples on the other panels. We speculate that the increasing R_1/R_2 as the neighbor approaches to $R_n/r_{vir,n} = 1$ is because of the tidal effect of the neighbor to the target galaxy. We calculate Spearman coefficient of the galaxies with narrower range, $R_n/r_{vir,n} = 1$ to 3.16, and find that the correlation becomes stronger ($\rho_{corr} = -0.206$) and more significant (1.9σ) with 82 data points. The decreasing R_1/R_2 as the neighbor approaches closer than $R_n/r_{vir,n} = 1$ could be explained as result of the direct interaction between the galaxies, because they are located closer than the virial radius of the neighbor.

In Figure 3.7, Spearman coefficients indicate that R_1/R_2 have positive correlation

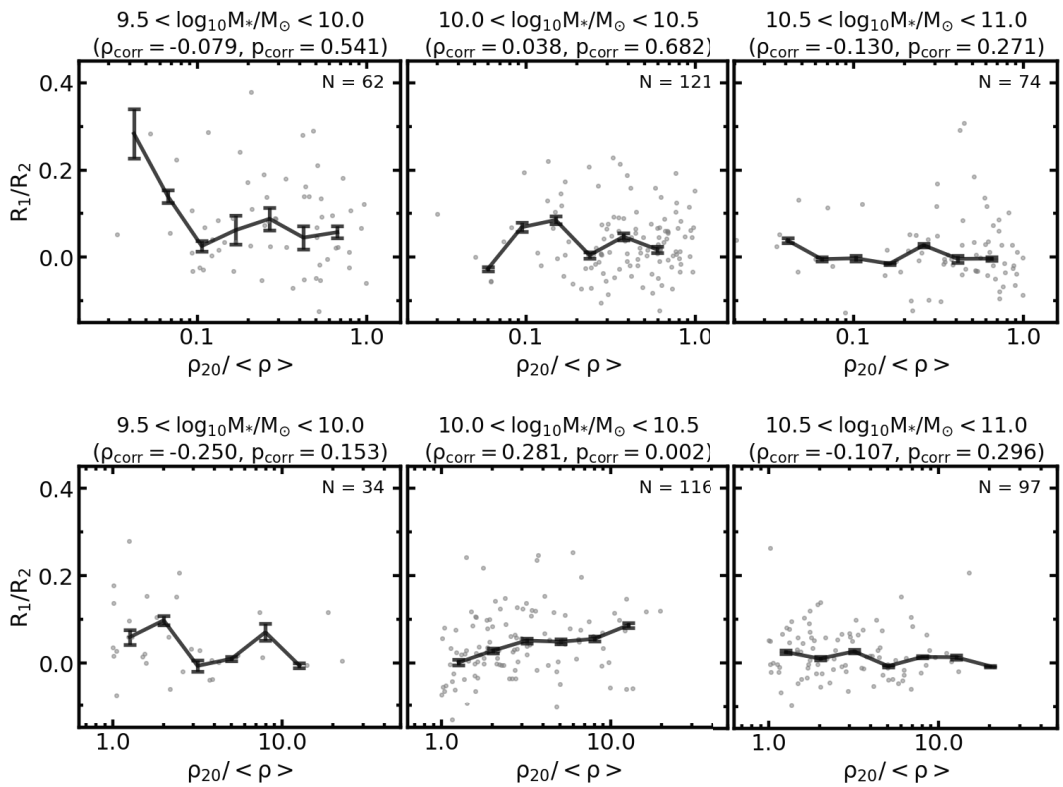

Figure 3.7. Dependence of RC outer gradient on the large-scale environmental parameter (ρ_{20}). The target galaxies in the left, center, and right panels are limited to their stellar mass ranges of $\log_{10}M_*/M_\odot$ = 9.5-10.0, 10.0-10.5, and 10.5-11.0, respectively. The top (bottom) panels shows the dependence when background density is less or equal than (greater than) the mean cosmic mass density. On each panel, Spearman rank correlation coefficient ($\rho_{\rm corr}$) and the corresponding p-value ($\rm p_{corr}$) is shown at title. The median values of R_1/R_2 are presented with black solid line.

with rho$_{20}$ when $\rho_{20}/<\rho>$ is greater than 1 in the intermediate mass range with 3.1σ level. Again, other panels does not show noticeable correlations with high p-values. This is in contradiction with the fore-mentioned interpretation of R_1/R_2 and small-scale environmental parameter, because high background mass density environment is more likely to have a smaller $\mathrm{R_n/r_{vir,n}}$. To examine this contradiction, we plot the distribution of target galaxies on the small- and large- scale environment parameter in Figure 3.8. The distribution shows that median $\mathrm{R_n/r_{vir,n}}$ values of the the galaxies in the intermediate mass range are greater than 1 even at $\rho_{20}/<\rho> > 1$. This means that the R_1/R_2 values at the $\rho_{20}/<\rho> > 1$ in Figure 3.7 are from the galaxies with $\mathrm{R_n/r_{vir,n}}$ slightly higher than 1. To investigate the strength of relative dependence of the environmental parameters to R_1/R_2, we plot R_1/R_2 contours on the small- and large- scale environmental parameters in Figure 3.9. Applied smoothing scale to the panels in Figure 3.9 is 0.6 dex. in logarithmic scale of both $\mathrm{R_n/r_{vir,n}}$ and $\rho_{20}/<\rho>$. In the intermediate mass range (middle panel), R_1/R_2 shows strong dependence on the background mass density but weak dependence on the distance to the nearest neighbor at $\rho_{20}/<\rho> > 1$. This $\rho_{20}/<\rho>$ dependence and the median $\mathrm{R_n/r_{vir,n}}$ greater than 1 at $\rho_{20}/<\rho>$ cause the strong positive correlation of R_1/R_2 on $\rho_{20}/<\rho>$ in the intermediate mass range, when $\rho_{20}/<\rho>$ is greater than 1 (Figure 3.7, bottom center). In Figure 3.9, the galaxies at high $\mathrm{R_n/r_{vir,n}}$, low $\rho_{20}/<\rho>$ and low mass range have high R_1/R_2 values (left panel). This can be interpreted as high R_1/R_2 is an intrinsic properties of the low-mass disk galaxies. High-mass galaxies (right panel) exhibit weak environmental dependence, but in general they have low R_1/R_2 value. In hierarchical galaxy formation scenario, this trend shows that galaxy RC outer gradient is decreasing as it experiences galaxy-galaxy interactions and mergers in general.

3.5 Summary and Conclusion

We measure RCs of SDSS-IV MaNGA galaxies and study their dependence on mass and environmental parameters. We perform deconvolution on the 3D Cube data by using wavelength-dependent PSF size information to mitigate the atmospheric seeing and the

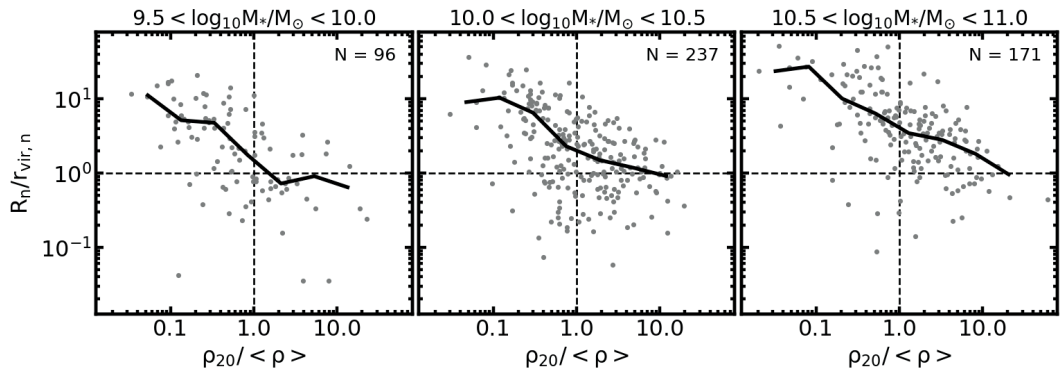

Figure 3.8. Data distribution on environmental parameters depend on stellar mass. The target galaxies in the left, center, and right panels are limited to their stellar mass ranges of $\log_{10}M_*/M_\odot$ = 9.5-10.0, 10.0-10.5, and 10.5-11.0, respectively. The median values of $R_n/r_{vir,n}$ are presented with black solid line.

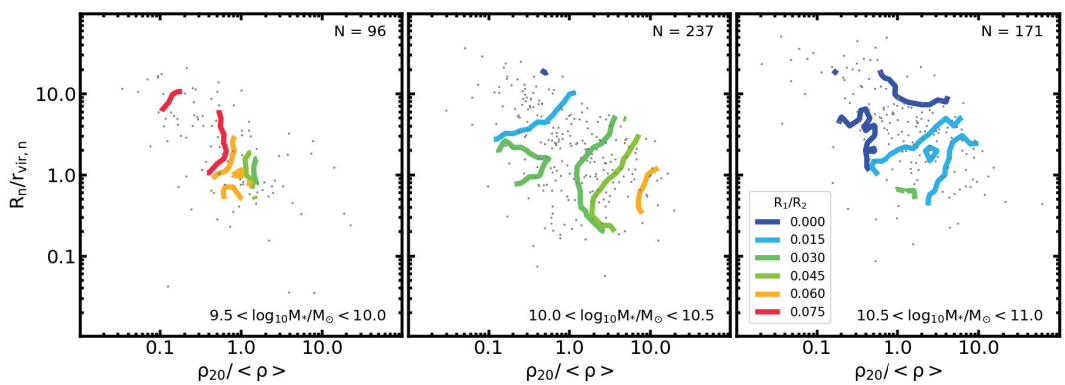

Figure 3.9. RC outer gradient contours on environmental parameters depend on stellar mass. The target galaxies in the left, center, and right panels are limited to their stellar mass ranges of $\log_{10}M_*/M_\odot$ = 9.5-10.0, 10.0-10.5, and 10.5-11.0, respectively. Contours are drawn only when there is sufficient number of data points (30) to calculate the representative value at a particular grid point.

beam-smearing effect. Using 2D stellar velocity maps measured from the deconvolved cubes, we fit simple thin-disk RC model (hyperbolic tangent function with the linear term) to obtain model parameters and kinematic geometry of the galaxies. This cube deconvolution is crucial to study the detail of the RC. We confirm that disk galaxies show clear rigid body rotation around the center and flat rotation at the outer part, but also show inclined RC (decreasing/increasing) at their outer radii. We examine the correlation between the RC outer gradient and the galaxy stellar mass, morphology, and environmental parameters. We find that kinematic core (RC scale radius) and the photometric core (bulge fraction - bulge to total ratio) of disk galaxies have different correlations depend on galaxy stellar mass. We also notice that RC outer gradients of the disk galaxies with T-type equal or greater than 2 (Sb, Sc, and Sd) have mass dependence, but those of the T-type less than 2 (S0, Sa) have no mass dependence but have T-Type dependence. RC outer gradient of intermediate mass galaxies ($10.0 < \log_{10}M_*/M_\odot < 10.5$) exhibit complex environmental dependence. The slope gradient is increasing as the nearest neighbor approaches up to $R_n/r_{vir,n} = 1$, but decreasing as the distance becomes shorter then $R_n/r_{vir,n} = 1$. No correlation is observed between the slope gradient and $\rho_{20}/<\rho>$ when $\rho_{20}/<\rho>$ is less than 1, but positive correlation is shown with high significance when $\rho_{20}/<\rho>$ is greater than 1. These results suggest that both large and small scale environmental parameters play a considerable effect on stellar kinematics.

Chapter 4

Dynamical Properties of Nearby Galaxies

4.1 Introduction

Dynamical modeling is essential to fully understand the kinematic properties of galaxies such as the amplitude and shape of rotation curve, mass distribution, and relative contribution of mass components to the total gravitational potential profile. The dynamical modeling requires both kinematic and photometric information of galaxy because the observed kinematics is the result of the motion of stars and gas, which are orbiting galaxy while emitting photons. The mass distribution obtained from the dynamical modeling is related with the galaxy properties, such as stellar mass, morphology, and the mass assembly history. Thus, understanding those relations will expand our knowledge on the galaxy formation process. Several methods for the dynamical modeling methods exist, such as Schwarzchild technique (Schwarzschild 1979, 1982), Made-to-measure N-body realization method (Syer & Tremaine 1996; de Lorenzi et al. 2007; Long & Mao 2010; Portail et al. 2015), analytic distribution-function-based methods (Binney 2010; Bovy 2014), and Jeans-Anisotropic-Model (JAM) method with the velocity second moments (Cappellari 2008).

Increasing number of integral field unit (IFU) spectroscopy surveys has recently

been providing a large number of samples to be dynamically modeled because the IFU data naturally provide the two-dimensional line-of-sight kinematic information. Among the available dynamical modeling methods, the JAM method has been implemented frequently to the IFU data to model the early-type fast-rotator or late-type disk galaxies. Its reliability in the dynamical modeling, along with the availability of `IDL` or `Python` codes and relatively short-computation time promotes its usage on the IFU survey data. For SAURON IFU data (Bacon et al. 2001), the JAM method was used to study the galaxy mass-to-light ratio and the kinematic inclination angle (Cappellari et al. 2006). Inclusion of the dark matter halo to the mass component was tested with ATLAS^{3D} data (Cappellari et al. 2011) and fraction of dark matter within 1 R_e was estimated (Cappellari et al. 2013). The method was also used to constrain the initial mass function of the galaxies by using the stellar mass-to-light ratio obtained from stellar population synthesis modeling and JAM method (Cappellari et al. 2012). Li et al. (2016) tested the reliability of JAM method when applied to the mock galaxies from Illustris simulation data (Genel et al. 2014). Cappellari et al. (2015); Bellstedt et al. (2018) applied the method to the combination of ATLAS^{3D} IFU data around the galaxy central region and the long-slit spectroscopy data which covers the galaxies up to $\sim 4R_e$. They compare the total mass profiles of early-type galaxies from the observation and EAGLE cosmological simulation data (Schaye et al. 2015). Recently, Li et al. (2019) studied the inner density slope of the nearby galaxies using JAM method to MaNGA IFU survey data (Mapping Nearby Galaxies at Apache Point Observatory; Bundy et al. 2015).

In this chapter, we apply the JAM method to SDSS DR15 MaNGA data (Aguado et al. 2019) and model the mass profile of galaxies. We use a mass model, a combination of a generalized Navarro-Frenk-White (NFW) profile and a galaxy stellar mass profile following the light profile of the galaxy with constant stellar mass-to-light ratio. This chapter is organized as follows. In section 4.2, we describe photometric and derived kinematics data used for the mass modeling. In section 4.3, we introduce JAM method and the fitting procedure. We show the result of JAM modeling and the derived galaxy

mass profile in section 4.4. We summarize in section 4.5.

4.2 Data

We use the third data release of the MaNGA survey (Bundy et al. 2015, DR15), part of the fourth generation of SDSS (Blanton et al. 2017). The survey aims to observe $\sim 10,000$ galaxies during its five-years duration, utilizing multiple IFUs which capture spectral information from 17 different area on the sky simultaneously. The detail of the survey can be found in section 1.3 and Appendix A. As with the previous chapter, we exclude the duplicated observations and the non-galaxy samples (see subsection 4.2.1). We use the deconvolved MaNGA IFU data using the deconvolution technique described in chapter 2. The total number of unique MaNGA galaxies used in this chapter is 4,425.

4.2.1 Photometry

An accurate galaxy photometry is essential to have a reliable 3D galaxy mass modeling result. There are two options for the photometry of MaNGA galaxies: 1) reconstructed broadband image from the deconvolved MaNGA data cube, 2) SDSS legacy imaging data taken by SDSS imaging camera. The reconstructed MaNGA broadband image have several advantages that it provides high S/N as well as contains only the region of interest (i.e. it does not require additional masking), but it may not sufficiently cover the galaxy due to the limited IFU field of view. Figure 2.1 shows an example where the MaNGA does not sufficiently cover the entire galaxy. On the other hand, SDSS imaging data has a finer sampling size than the reconstructed MaNGA broadband image (SDSS: 0.4 pixel, MaNGA: 0.5 pixel), and it has full radial coverage of a galaxy which is essential to model the galaxy photometry accurately. This is an advantage over the reconstructed MaNGA broadband image because the full radial coverage would enable more accurate photometry modeling. We compare the result of Multi-Gaussian Expansion modeling of galaxy photometry using both the reconstructed MaNGA r-band image and SDSS r-band imaging data. We find that SDSS imaging data provides better results, therefore we choose the SDSS imaging data as photometry data for the 3D mass modeling.

4.2.2 2D kinematics

We use the 2D line-of-sight velocity distribution (LOSVD, both velocity and the velocity dispersion) of 4,425 MaNGA main galaxy samples, measured in subsection 2.4.2. The galaxy LOSVD is accurately measured by fitting the MILES spectral engery distribution model using pPXF (Cappellari & Emsellem 2004; Cappellari 2017) (See subsection 2.3.3 and subsection 2.4.2).

4.3 Jeans Anisotropic Modeling with Multi-Gaussian Expansion

4.3.1 Multi-Gaussian Expansion

Multi-Gaussian Expansion (MGE) is an efficient method to model the photometry of galaxy. The method decompose the given 2D distribution into the summation of multiple 2D Gaussian function. It is a generalized approach of Monnet et al. (1992), described in Emsellem et al. (1994); Cappellari (2002). The method have several advantages: 1) It can accurately reproduce the given 2D photometry. 2) It provides simple way of de-projecting the decomposed 2D distribution with a given viewing angle, 3) It can consider the effect of PSF convolution and provide the PSF-deconvolved analytic description of the given surface brightness distribution, 4) It can also be applied to decompose 1D distribution such as a dark matter halo profile. Here we describe the equations and derivations of MGE method, cited and summarized from Emsellem et al. (1994), Cappellari (2002) and Cappellari (2008) (hereafter C08). The surface brightness μ of a galaxy can be written as (C08, eq. 12)

$$\mu(x', y') = \sum_{k=1}^{N} \frac{L_k}{2\pi\sigma_k^2 q_{k'}} \exp\left[-\frac{1}{2\sigma_k^2}\left(x'^2 + \frac{y'^2}{q_k'^2}\right)\right], \tag{4.1}$$

at the location of (x', y') on the plane of sky, where N is the number of Gaussian function with total luminosity L_k, dispersion σ_k, and apparent axial ratio of $0 \leq q_k' \leq 1$ (1 being circle), assuming the x-axis is aligned with the major axis of the galaxy. Assuming

the 3D shape of a galaxy is axisymmetric and oblate, the de-projected MGE luminous density ν in the cylindrical coordinate can be obtained as (C08, eq. 13,14)

$$\nu(R,z) = \sum_{k=1}^{N} \frac{L_k}{(\sqrt{2\pi}\,\sigma_k)^3 q_k} \exp\left[-\frac{1}{2\sigma_k^2}\left(R^2 + \frac{z^2}{q_k^2}\right)\right], \tag{4.2}$$

$$q_k = \frac{\sqrt{q_k'^2 - \cos^2 i}}{\sin i}, \tag{4.3}$$

where the de-projected Gaussian components have identical total luminosity L_k and dispersion σ_k of the projected Gaussian components but with different intrinsic axial ratio q_k, depend on the inclination angle i.

The mass density ρ of the galaxy also can be represented by MGE as (C08, eq. 15)

$$\rho(R,z) = \sum_{j=1}^{M} \frac{M_j}{(\sqrt{2\pi}\,\sigma_j)^3 q_j} \exp\left[-\frac{1}{2\sigma_j^2}\left(R^2 + \frac{z^2}{q_j^2}\right)\right], \tag{4.4}$$

where M_j is the total mass of the j^{th} Gaussian component. If the mass component distribution follows the same light distribution as Equation 4.2, then $M = N$, $\sigma_j = \sigma_k$, $q_j = q_k$, and $M_j = \Upsilon_k L_k$ where Υ_k is the mass to light ratio (M/L) of k^{th} Gaussian component. If there is an additional mass component such as dark matter, M becomes greater than N and the additional mass component in MGE format should be added.

Emsellem et al. (1994, eq. 39-40) derived the gravitational potential Φ originated by the Equation 4.4 as (C08, eq. 16,17)

$$\Phi(R,z) = -\sqrt{2/\pi}\,G \int_0^1 \sum_{j=1}^{M} \frac{M_j\,\mathcal{H}_j(u)}{\sigma_j} \mathrm{d}u, \tag{4.5}$$

where

$$\mathcal{H}_j(u) = \frac{\exp\left\{-\frac{u^2}{2\sigma_j^2}\left[R^2 + \frac{z^2}{1-(1-q_j^2)u^2}\right]\right\}}{\sqrt{1-(1-q_j^2)u^2}}, \tag{4.6}$$

and G is the gravitational constant.

To apply the MGE method to the observation data, we use `Python` version of the latest `MGE package`[1] (`v5_0_11`) developed by Cappellari (2002). We follow the scheme described below to model the galaxy photometry with MGE.

[1] MgeFit, `http://www-astro.physics.ox.ac.uk/~mxc/software/`

1. We make a postage r-band image of each MaNGA galaxy from the SDSS r-band *field* images. To cover sufficient area around each target, size of the postage image is determined to be 24 times of the elliptical Petrosian half-light radius of the target galaxy ($1R_e$), as provided by NSA catalog.

2. We subtract the sky background from each image by using `measure_sky`[2] routine. The routine estimates the background level by fitting the second order polynomial (ax^2+bx+c) on the logarithmic histogram of the flux. The location of the central peak ($-b/2a$) is determined as the sky level. σ_{sky} is determined as $(-2a\ln 10)^{-0.5}$.

3. We find a galaxy from each postage image, by searching area around the center of each galaxy with elliptical aperture. We modify the `find_galaxy`, a subroutine of `mge_fit` package to limit the search region according to the given mask. The elliptical aperture size is determined as 3 times larger than $1R_e$. Axis ratio and positional angle values from NSA catalog are implemented to determine the shape and orientation of the aperture. In addition, we use `DAOStarFinder` routine from `Astropy`[3] (`v3_1_2`) to find point sources within the elliptical aperture. We mask the circular region around each point sources with a radius 3 times larger than the seeing size of each image. This additional mask efficiently excludes the foreground/background stars and improve the galaxy finding accuracy.

4. We perform MGE fitting on each galaxy using `sectors_photometry` and `mge_fit_sectors` which are subroutines of the `mge_fit` package. Before the fitting, we define a new elliptical aperture around each galaxy, with the new geometry (center, axial ratio, and position angle) determined by `find_galaxy` routine. Then, we replace all the pixel values outside of the elliptical aperture to be less than 3 σ_{sky} to perform MGE fit on the target galaxy only. We use bulge/disk decomposition option, which enforce the result of MGE fitting to have two different axial ratios. We find that the galaxy photometry can be more accurately modeled by using the option.

[2] `https://gist.github.com/jiffyclub/1310947#file-msky-py`

[3] `https://www.astropy.org`

Figure 4.1 shows an example of the galaxy finding and the MGE fitting step. It also shows the masked region around a star near the target. Figure 4.2 shows the example of MGE result.

4.3.2 Jeans Anisotropic Modeling

JAM is an efficient method to model the line-of-sight velocity second moment of galaxies. The method is based on the axisymmetric Jeans equations which can describe the distribution function of a large system of stars in a steady state under the influence of the smooth gravitational potential. A detail description of the method is described in C08, so here we describe the equations and derivations of JAM method, cited and summarized from C08.

From the collisionless Boltzmann equation (Binney & Tremaine 1987, equation 4-13b), we can derive the following equation (C08, eq. 2) with the assumption of axial symmetry ($\partial\Phi/\partial\phi = \partial f/\partial\phi = 0$).

$$v_R\frac{\partial f}{\partial R} + v_z\frac{\partial f}{\partial z} + \left(\frac{v_\phi^2}{R} - \frac{\partial\Phi}{\partial R}\right)\frac{\partial f}{\partial v_R} - \frac{\partial\Phi}{\partial z}\frac{\partial f}{\partial v_z} - \frac{v_R v_\phi}{R}\frac{\partial f}{\partial v_\phi} = 0, \tag{4.7}$$

where $f(\mathbf{x}, \mathbf{v})$ is the distribution function of star system.

By multiplying v_z and v_R respectively on Equation 4.7 and integrating over all velocities, the two Jeans equations (Jeans 1922) are derived as follow (C08, eq. 3-5).

$$\frac{\nu\overline{v_R v_z}}{R} + \frac{\partial(\nu\overline{v_z^2})}{\partial z} + \frac{\partial(\nu\overline{v_R v_z})}{\partial R} = -\nu\frac{\partial\Phi_{tot}}{\partial z}, \tag{4.8}$$

$$\frac{\nu\overline{v_R^2} - \nu\overline{v_\phi^2}}{R} + \frac{\partial(\nu\overline{v_R^2})}{\partial R} + \frac{\partial(\nu\overline{v_R v_z})}{\partial z} = -\nu\frac{\partial\Phi_{tot}}{\partial R}, \tag{4.9}$$

where Φ_{tot} is the total potential, ν is luminosity density, and

$$\nu\overline{v_k v_j} \equiv \int v_k v_j f \, \mathrm{d}^3\mathbf{v}. \tag{4.10}$$

The above equations can be further revised with the assumptions made in Cappellari (2008): 1) the velocity ellipsoid is aligned with the cylindrical coordinate system

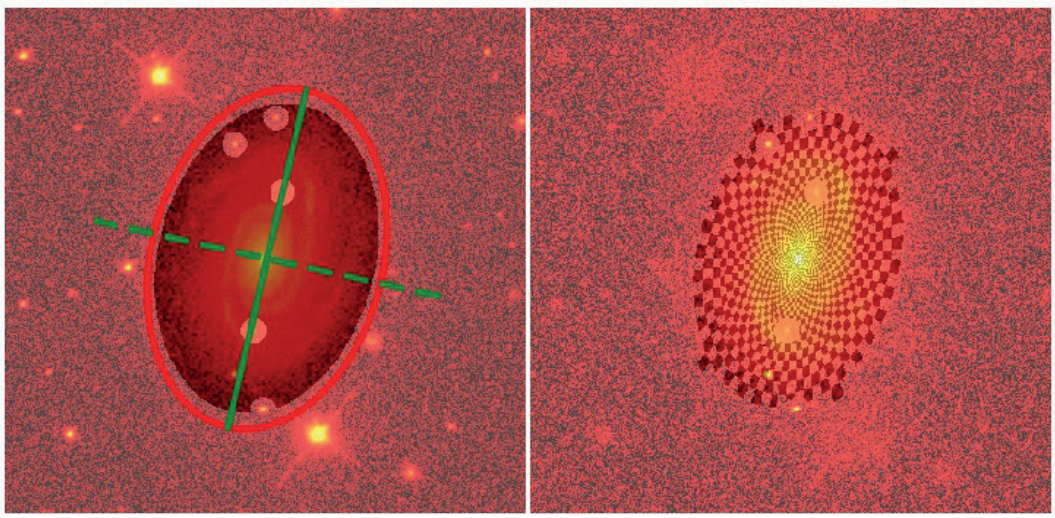

Figure 4.1. Example of galaxy finding and MGE fitting. (left) Image shows galaxy search region with masked point sources with in the region (Point sources can be cross-matched with the galaxy image in Figure 4.2.) (right) A region of MGE fitting is marked with cross stripe pattern. Note that the objects outside of the fitting region are now clipped out.

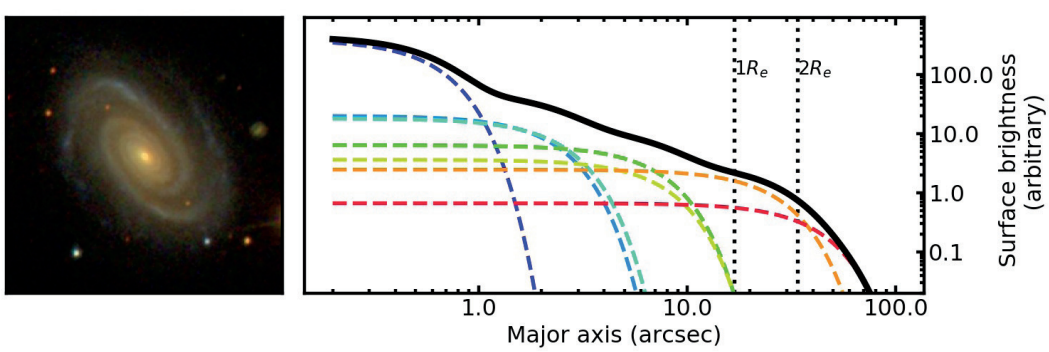

Figure 4.2. Result of MGE fitting on a galaxy. The sum of multiple Gaussian consists the total surface brightness profile of the galaxy.

(R, z, ϕ) ($\nu\overline{v_R v_z} = 0$), 2) the anisotropy is constant, quantified as $\overline{v_R^2} = b\,\overline{v_z^2}$. Use of the cylindrical coordinate does not accurately represent the shape and orientation of the velocity ellipsoid, but it provides good approximation near the equatorial plane where the density is at its maximum. With the assumptions, Equation 4.8 and Equation 4.9 become (C08, eq. 8,9)

$$\frac{\partial(\nu\overline{v_z^2})}{\partial z} = -\nu\frac{\partial\Phi_{tot}}{\partial z}, \tag{4.11}$$

$$\frac{b\,\nu\overline{v_z^2} - \nu\overline{v_\phi^2}}{R} + \frac{\partial(b\,\nu\overline{v_z^2})}{\partial R} = -\nu\frac{\partial\Phi_{tot}}{\partial R}. \tag{4.12}$$

If we applies the boundary condition $\nu\overline{v_z^2} = 0$ as $z \to \infty$, we can derive the solution as (C08, eq. 10,11)

$$\nu\overline{v_z^2}(R, z) = \int_z^\infty \nu\frac{\partial\Phi_{tot}}{\partial z}\mathrm{d}z, \tag{4.13}$$

$$\nu\overline{v_\phi^2}(R, z) = b\left[R\frac{\partial(\nu\overline{v_z^2})}{\partial R} + \nu\overline{v_z^2}\right] + R\nu\frac{\partial\Phi_{tot}}{\partial R}. \tag{4.14}$$

Now the $\nu(R, z)$ and $\rho(R, z)$ described by MGE method can be applied to solve the axisymmetric-anisotropic Jeans euations. Substituting Equations (4.2), (4.4), (4.5), and (4.6) into Equation 4.13 and Equation 4.14, and performing analytical integration in z, we get (C08, eq. 19-23)

$$[\nu\overline{v_R^2}]_k = b_k[\nu\overline{v_z^2}]_k, \tag{4.15}$$

$$[\nu\overline{v_z^2}]_k = 4\pi G\int_0^1 \sum_{j=1}^M \frac{\sigma_k^2 q_k^2 \nu_k q_j \rho_{0j}\mathcal{H}_j(u)\,u^2}{1 - \mathcal{C}u^2}\,\mathrm{d}u, \tag{4.16}$$

$$\begin{aligned}[\nu\overline{v_\phi^2}]_k &= [\nu\overline{v_R^2}]_k + 4\pi G\int_0^1 \sum_{j=1}^M \frac{\nu_k q_j \rho_{0j}\mathcal{H}_j(u)\,u^2}{1 - \mathcal{C}u^2}\mathcal{D}\,R^2\mathrm{d}u \\ &= 4\pi G\int_0^1 \sum_{j=1}^M \frac{\nu_k q_j \rho_{0j}\mathcal{H}_j(u)\,u^2}{1 - \mathcal{C}u^2}\left(\mathcal{D}\,R^2 + b_k\sigma_k^2 q_k^2\right)\mathrm{d}u,\end{aligned} \tag{4.17}$$

where $\nu_k = \nu_k(R, z)$, $\rho_{0j} = \rho_j(0, 0)$ and

$$\mathcal{C} = 1 - q_j^2 - \frac{\sigma_k^2 \, q_k^2}{\sigma_j^2}, \tag{4.18}$$

$$\mathcal{D} = 1 - b_k \, q_k^2 - \left[(1 - b_k) \, \mathcal{C} + (1 - q_j^2) \, b_k\right] u^2. \tag{4.19}$$

To compare the model with the observation, we need a line-of-sight integration of the velocity second moment. We define the sky coordinate system of (x', y', z') where z' is line-of-sight direction, and the x' and y' axes are aligned with the projected major and minor axis of the galaxy. The galaxy coordinate are expressed by the sky coordinates as (C08, eq. 25)

$$\begin{aligned} x &= x', \\ y &= -y' \cos i + z' \sin i, \\ z &= y' \sin i + z' \cos i, \end{aligned} \tag{4.20}$$

where z is the galaxy symmetry direction, and x and y are constrained by the cylindrical radius as $R^2 = x^2 + y^2$.

The projected velocity second moments $\overline{v_{\rm los}^2}$ is identical to $\overline{v_{z'}^2}$. It is given for each Gaussian component of the MGE surface density as (C08, eq. 26)

$$[\Sigma \, \overline{v_{\rm los}^2}]_k = \int_{-\infty}^{\infty} \left\{ [\nu \overline{v_z^2}]_k \cos^2 i + \left([\nu \overline{v_R^2}]_k \sin^2 \phi + [\nu \overline{v_\phi^2}]_k \cos^2 \phi \right) \sin^2 i \right\} \mathrm{d}z', \tag{4.21}$$

where $\cos \phi = x/R$. The total observed second moment for the whole MGE model is then (C08, eq. 27),

$$\Sigma \, \overline{v_{\rm los}^2} = \sum_{k=1}^{N} [\Sigma \, \overline{v_{\rm los}^2}]_k. \tag{4.22}$$

By substituting Equations (4.6), (4.15) - (4.17), (4.20), and (4.21) into (4.22), and performing z' integral analytically, we can obtain the final expression of the line-of-

sight velocity second moments at the given sky location (x', y') as (C08, eq. 28-30)

$$\overline{v_{\rm los}^2}(x', y') = 4\pi^{3/2} G \int_0^1 \sum_{k=1}^{N} \sum_{j=1}^{M} \nu_{0k}\, q_j\, \rho_{0j}\, u^2 \times \frac{\sigma_k^2 q_k^2 \left(\cos^2 i + b_k \sin^2 i\right) + \mathcal{D}\, x'^2 \sin^2 i}{(1 - \mathcal{C}u^2)\sqrt{(\mathcal{A} + \mathcal{B}\cos^2 i)\left[1 - (1 - q_j^2)u^2\right]}} \times \exp\left\{-\mathcal{A}\left[x'^2 + \frac{(\mathcal{A} + \mathcal{B})y'^2}{\mathcal{A} + \mathcal{B}\cos^2 i}\right]\right\} {\rm d}u, \tag{4.23}$$

where we define $\nu_{0k} = \nu_k(0, 0)$ and

$$\mathcal{A} = \frac{1}{2}\left(\frac{u^2}{\sigma_j^2} + \frac{1}{\sigma_k^2}\right), \tag{4.24}$$

$$\mathcal{B} = \frac{1}{2}\left\{\frac{1 - q_k^2}{\sigma_k^2 q_k^2} + \frac{(1 - q_j^2)u^4}{\sigma_j^2\left[1 - (1 - q_j^2)u^2\right]}\right\}. \tag{4.25}$$

The observed quantity $V_{\rm rms}^2 = V^2 + \sigma^2$, which is a quadrature summation of the line-of-sight stellar velocity V and the velocity dispersion σ is a good approximation of the velocity second moments $\overline{v_{\rm los}^2}$ (Equation 4.23). We can model the 3D mass distribution of a given galaxy by comparing the $\overline{v_{\rm los}^2}(x', y')$ from JAM model with the $V_{\rm rms}^2(x', y')$ from observed kinematics in 2D.

We apply JAM method to model the mass distribution of MaNGA galaxies. We choose a galaxy mass model comprised of two components: 1) Baryonic mass distribution which follows the surface brightness distribution, 2) Dark matter halo model with the generalized NFW (gNFW) profile (Hernquist 1990; Navarro et al. 1996; Merritt et al. 2006). Here we list the assumptions we made in our mass model:

1. The galaxy surface brightness distribution is in oblate shape, therefore the MGE model can be de-projected analytically following the Equation (4.2) and (4.3).

2. Both stars and gas follow the same galaxy surface brightness distribution.

3. A constant baryonic mass-to-light ratio over the galaxy.

4. A constant velocity anisotropy (β_z) over the galaxy.

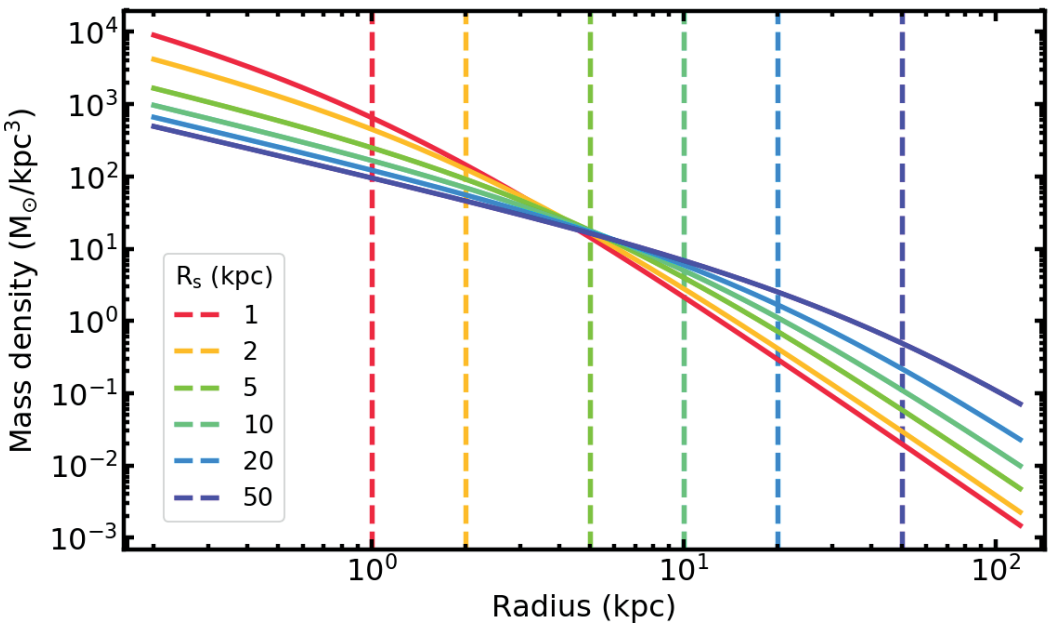

Figure 4.3. NFW profiles with various R_s with $\gamma = -1$. Density slope of all profiles are converging to -3 when $r \gg R_s$

5. Fixed gNFW profile scale radius (R_s) as 20 kpc.

The gNFW profile has a following form

$$\rho(r) = \rho_0 (\frac{r}{R_s})^{-\gamma} (\frac{1}{2} + \frac{1}{2}\frac{r}{R_s})^{\gamma-3}, \tag{4.26}$$

where R_s is scale length of the profile and $\rho_0 = \rho(R_s)$. As an example, we plot several NFW profiles with different R_s in Figure 4.3. The equation becomes power law gradient $\gamma = -3$ at the larger radii $r \gg R_s$, and allows inner gradient variant with γ. With $\gamma = -1$, the equation converges to the standard NFW profile.

To utilize the gNFW profile for the JAM method, we convert the given profile into the sum of multiple Gaussians by using 1D MGE package[4]. Then the profile becomes

$$\rho(r) = \rho_0 \sum_{j=1}^{M} \frac{S_j}{\sqrt{2\pi}\sigma_j} \exp\left[-\frac{r^2}{2\sigma_j^2}\right], \tag{4.27}$$

[4]MGE 1D routine, `http://www-astro.physics.ox.ac.uk/~mxc/software/`

where S_j is a surface mass density of j^{th} Gaussian component of $\rho(r)$ when $\rho_0 = 1$. By de-normalizing the S_j to express $\rho(r)$ in a form consistent with Equation 4.4 (i.e. in 3D), now $\rho(r)$ becomes

$$\rho(r) = \rho_0 \sum_{j=1}^{M} \frac{M_j}{(\sqrt{2\pi}\sigma_j)^3} \exp\left[-\frac{1}{2\sigma_j^2}\left(R^2 + z^2\right)\right], \tag{4.28}$$

where R, z are in cylindrical coordinate and $M_j = 2\pi {\sigma_j}^2 S_j$.

Follow the approach of Cappellari et al. (2013) and Li et al. (2016), we express the ρ_0 as f_{DM} which is the fraction of dark matter over the total mass within the galaxy half light radius R_e.

The constant velocity anisotropy allows to use a single parameter β_z to express the anisotropy of the whole galaxy (C08, eq. 24).

$$\beta_z(R,z) \equiv 1 - \frac{\overline{v_z^2}}{v_R^2} = 1 - \frac{\sum_k [\nu \overline{v_z^2}]_k}{\sum_k b_k [\nu \overline{v_z^2}]_k} \approx 1 - \frac{\sum_k \nu_k}{\sum_k b_k \nu_k}. \tag{4.29}$$

Our JAM model have five free parameters: Inclination angle i, velocity anisotropy β_z, barynoic mass to light ratio M/L, dark matter fraction f_{DM}, dark matter halo inner gradient γ, and the dark matter scale radius R_s. We use Python3 version of the latest `JAM package`[5] (`v3.1.20`) developed by C08. The package calculate the projected $\overline{v_{\rm los}^2}(x', y')$ distribution from the given inclination angle, and velocity anisotropy, $\nu(R, z)$ and $\rho(R, z)$ in the form of MGE. To find the best-fit set of model parameters efficiently, we use MCMC approach using emcee package, a widely used MCMC sampler.

4.4 Galaxy Mass Profile

Figure 4.4 shows the examples of the JAM fitting result and the mass profile of MaNGA galaxies. The 2D $V_{\rm rms,obs.}$ map and the $V_{\rm rms,model}$ map exhibit great agreement with each other, although there are some differences in the small scale. The right most column shows the total and the decomposed mass profiles divided by stellar and dark matter. Figure 4.5 presents the distribution of the derived JAM model parameters of the

[5]JAM, `http://www-astro.physics.ox.ac.uk/~mxc/software/`

MaNGA galaxies. The distributions are located mostly around the known parameter range (ref), except for the $i_{\rm JAM}$ parameter which is used for the de-projection of 2D luminosity distribution into the 3D. Its distribution is highly skewed for the higher inclination angle, and shows systematic offset when compared with the $i_{\rm NSA}$ values calculated from the b/a ratio. This is due to the known inclination degeneracy with JAM model (ref) that the dynamical inclination is not well constrained by the projected 2D $V_{\rm RMS}$ distribution only. There are also several unusual parameter values at low $\beta_{\rm z}$ (<-1), high γ (> -0.5), or small peak around $M_*/L \sim 6$. Further quality assurance and investigation is required to the galaxies with abnormal model parameters.

4.5 Summary and Conclusion

We perform the dynamical modeling of SDSS-IV MaNGA Galaxies and decompose their 3D mass profiles in to the baryonic matter and the dark matter. We use the Jeans-Anisotropic Multi-Gaussian Expansion (JAM) model which describe distribution of stellar motions following the Jeans equation. The model describe the observed 2D velocity root-mean-square distribution by solving the Jeans equation assuming the axial symmetry, constant velocity ellipsoid shape aligned with the cylindrical coordinate system, constant stellar mass-to-light ratio, and the oblate shape luminosity distribution. Our JAM model is comprised of the surface brightness of galaxy described by multi-Gaussian, dynamical inclination angle, velocity anisotropy, stellar mass to light ratio, fraction of the dark matter, and the inner density slope of the generalized dark-matter halo. The derived mass profiles exhibit various combination of model parameters. Future study will explore the relation between the model parameters and the galaxy properties.

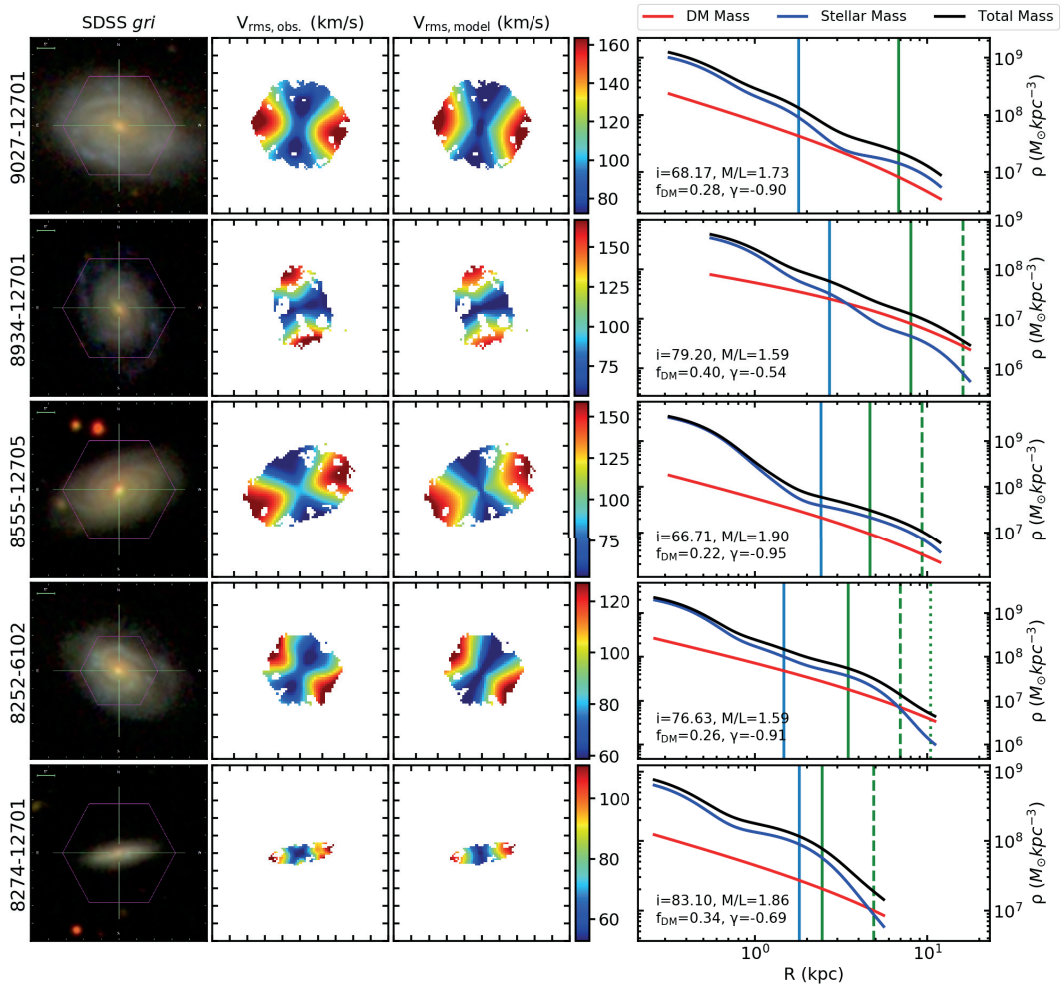

Figure 4.4. Example of the result of JAM fitting and mass profile of galaxies. Each row represents the result of the selected MaNGA galaxy. PLATE-IFU designation of each galaxy is presented on the left side of each *gri* image. Identical color bar is used for both 2D $V_{rms,obs.}$ and $V_{rms,model}$ distribution. A tick size of the 2D distribution is 5″. The vertical light-blue line marks the scale radius of the fitted RC model. The green solid, dashed, dotted vertical lines represent 1 R_e, 2 R_e, and 3 R_e, respectively. The profiles are fitted from 0.5″ (converted to kpc) to the maximum radial distance on the galaxy minor axis with $S/N_{pPXF} > 5$. The model parameter values are shown in the lower-left corner of each mass profile plot, where i is inclination angle, M/L is stellar mass to light ratio, f_{DM} is the fraction of dark matter over the total mass with in 1 R_e, and γ is the inner density slope of the gNFW profile.

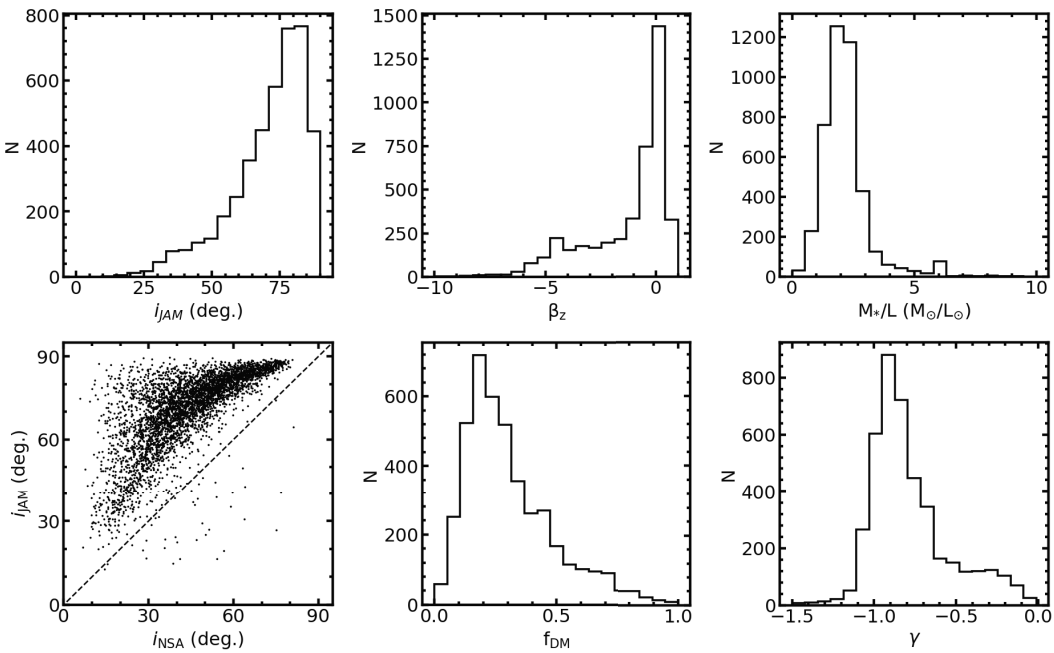

Figure 4.5. Each plot shows the distribution of JAM model parameters ($i_{\rm JAM}$, $\beta_{\rm z}$, $\rm M_*/L$, $\rm f_{DM}$, and γ), except for the lower left plot which present the relation between $i_{\rm NSA}$ and $i_{\rm JAM}$.

Chapter 5

Summary

In this thesis, we study the dynamical properties of the nearby galaxies and their relation to the environment. To do that, we utilize the integral field spectroscopy data, which can provide the spatially resolved kinematics of the galaxies, therefore the information of the galaxy mass distribution. We use the data from SDSS-IV MaNGA, the largest integral-field-unit (IFU) survey up to date. The use of ~ 4500 galaxy IFU data enable us to avoid the sampling bias and perform a statistical study on the dynamics of the galaxies spans on the wide range of stellar mass and morphology.

Although MaNGA survey provides a large number of galaxy IFU data, the combination of the atmospheric seeing effect and the sparse distribution of IFU sampling elements (optical fibers) make a large effective Point Spread Function (PSF) and generate highly correlated data in the spatial direction. In chapter 2, we develop a PSF deconvolution technique for the IFU data to mitigate the effects of the PSF convolution. The technique considers the IFU data as a combination of multiple 2D images at each wavelength, and applies Lucy-Richardson algorithm to deconvolve each 2D image using the information of the wavelength dependent PSF size which was convolved on to the images. The algorithm requires only two parameters which are the Full-Width-Half-Maximum (FWHM) of Gaussian shape PSF, and the number of iteration to perform. By using mock IFU data, we quantitatively demonstrate that the effects of PSF convolution is indeed significant, but at the same time, the effect can be relieved by our PSF

deconvolution method. We test our method to the ∼150,000 mock IFU data which is comprised of diverse combinations of the galaxy geometry, luminosity profile, signal to noise ratio, and velocity/velocity dispersion profile. We confirm that our method works efficiently and can be used to recover the kinematic distribution of the galaxy. Through the experiments with the mock IFU data, we find a suitable number of iteration for the deconvolution as $N_{iter} = 20$. We also investigate the cases where the size of PSF FWHM used for the deconvolution is different from the actual value, which is indeed inevitable in practice. We demonstrate that the result from the deconvolution is still effective even when the size of PSF FWHM used for the deconvolution is $\pm 0.3''$ larger or smaller than the actual PSF FWHM value.

We apply our method to the MaNGA survey data. The result shows that the technique makes noticeable difference in the derived 2D velocity and velocity dispersion distribution. We also find that the method can be applied to measure the correct λ_R parameter, a proxy of the spin parameter λ. We compare the λ_R value measured from the PSF-free, PSF-convolved, and PSF-deconvolved mock IFU data and find that the λ_{R_e} measured from the PSF-deconvolved data provides the value comparable to the correct value. Unlike the known analytic correction function which may over-corrects the λ_R value, the one measured from the deconvolved-IFU data provides reasonable value.

In chapter 3, we study the rotation curve (RC) of the nearby galaxies using the deconvolved MaNGA IFU data. We employ 4,425 unique MaNGA galaxy IFU data from its main galaxy sample. We introduce an improved RC model, which is a combination of the hyperbolic tangent function and a linear term. The improved RC model allows a radially increasing/decreasing RC at galaxy outskirts, which are the characteristics of the real galaxy RC. We fit the RC model to the 2D line-of-sight velocity distribution of MaNGA galaxies, and obtain the RC model parameter values. To study the relation between the properties of galaxy RC and their environment, we use the small-scale (R_n, the projected distance to the nearest neighbor) and the large-scale (ρ_{20}, the background mass density from the 20 nearest galaxies) environmental parameters. We limit our

analysis to late-type galaxies only because the model fitting assumes thin-disk model, which is physically not valid for the early-type galaxies. We also select galaxies which are well-fitted by our RC model and have radial coverage sufficient to characterize the outer slope of the RC.

We study the two parameters from the RC models, which are 1) the RC scale radius (R_1) where the central rigid body rotation ends, and 2) the normalized RC slope at the outer radii beyond the RC scale radius (R_1/R_2). From the $\sim$ 600 MaNGA late-type galaxies, we find that they have a variety of RC outer slope (nearly flat but increasing or decreasing as well). The R_1/R_2 exhibits a positive correlation, weakly with the galaxy stellar mass and strongly with the R_1, relatively. There is also an R_1/R_2 dependence on the morphology, but only with the galaxies of T morphological Type (T-Type) less than 2. For the galaxies with T-Type equal or greater than 2, T-Type dependence is disappeared and strong stellar mass dependence is arisen. For the intermediate mass ($10.0 < \log_{10}\mathrm{M}_*/\mathrm{M}_\odot < 10.5$) galaxies, the R_1/R_2 is slightly increasing as the R_n gets closer to one virial radius of the nearest neighbor galaxy, and is decreasing as the distance becomes shorter than one virial radius. In the galaxy stellar mass versus ρ_{20} plane, the gradient is almost flat as the ρ_{20} increases to the mean cosmic mass density, and then is increasing after then. These results show that the shape of the galaxy rotation curve is closely related to their environment, especially to the morphology and the distance of the nearest neighbor. This could be the result of the direct interaction and the tidal effect of the nearest neighbor. On the R_n versus the ρ_{20} plane, the R_1/R_2 value shows strong correlation with ρ_{20} when ρ_{20} becomes larger than the mean background mass density of the universe. Low mass galaxies at low background mass density, far from the nearest neighbor have high R_1/R_2 intrinsically. It seems that the RC outer slope becomes flatten as galaxy experience various galaxy-galaxy interaction and merger.

In chapter 4, we model the 3D distribution of the mass components of MaNGA galaxies using Jeans-anisotropic-model (JAM) method. With the assumption of axial symmetry and the constant velocity anisotropy over the entire radius, JAM provides

a expected line-of-sight RMS velocity distribution ($V_{RMS} = \sqrt{V^2 + \sigma^2}$) with the underlying surface brightness and the mass density distribution described by the Multi-Gaussian-Expansion (MGE) method. By using JAM method, the analytic expression of the 2D line-of-sight V_{RMS} distribution can be calculated with only a single quadrature integration, which significantly reduces the computation time, therefore, enables the model parameter search based on the computationally expensive Markov chain Monte Carlo scheme. We model the surface brightness distribution of the 4,425 MaNGA main galaxy samples with MGE method using the SDSS r-band postage image, and apply JAM method with the mass density model which is a summation of a) the stellar mass density profile following the surface brightness distribution and b) the generalized NFW halo profile. As a result, we obtain the mass density profile of the entire MaNGA galaxies and show some of the profiles. The density profiles have a diverse combination of model parameters (inclination angle, M_*/L ratio, the velocity anisotropy, the dark matter fraction, and the dark matter halo inner density slope) thus they can be used for the future research to find a link between the mass density model parameters and the galaxy properties.

Along with the research on the dynamical properties of the galaxies, we have worked on the development of the multi-IFU optical spectrograph instrument to extend the current study. The instrument called Devasthal Optical Telescope Integral Field Unit (DOTIFS), being developed by the instrumentation group at the Inter-University Centre for Astronomy and Astrophysics, will be mounted on the 3.6m Devasthal Optical Telescope managed by Aryabhatta Research Institute of Observational Sciences. Korea Institute for Advanced Study and Seoul National University are participating in the project as international collaborators. The strength of DOTIFS is coming from its multi-object observation capability with the 16 fiber-lenslet based IFUs (each with $8.7'' \times 7.4''$ field of view). The real-time deployable IFUs have a significant advantage over the other optical multi-IFU instruments such as MaNGA and SAMI, which have considerable overhead time for the IFU reconfiguration. DOTIFS IFUs can be even buttable with each other thus it can act as a single IFU with wider field of view. The

spectrograph covers the entire optical wavelength range from 370 nm to 740 nm, with spectral resolving power of R = 1200 − 2400. In the early stage of the development, we conducted a conceptual design study of the instrument. The study include the optics parameter determination, IFU design, and the deployment system concept. The proposed design is used as a reference for the individual subsystem design. We have designed the optics subsystems which are spectrograph collimator and camera optics, fore-optics, and the calibration unit optics. The spectrograph optics exploits the high-throughput volume-phase-holographic grating, Calcium Fluoride and i-line glasses, and the graded coating on the CCD to maximize its throughput over the entire wavelength range. We performed a tolerance analysis and derived the optics fabrication and the alignment budget. We also conducted a thermal analysis and discovered the possibility of the optical performance degradation due to the thermal expansion. We resolved the issue by adopting a linear stage for the movement of CCD dewar. In addition to the hardware designs, we have developed the spectrograph CCD image simulator and the signal to noise ratio calculator. Currently, the project is in the assembly, integration, and test period of its first stage, which will employ four IFUs with two spectrographs. Its second stage with additional twelve IFUs and six spectrographs will be followed immediately after the completion of the first stage. When DOTIFS is commissioned, it will be used to conduct various observational studies including follow up of MaNGA survey, outer region of nearby galaxies, and interacting/merging galaxy systems.

Bibliography

Abazajian, K. N., Adelman-McCarthy, J. K., Agüeros, M. A., et al. 2009, ApJS, 182, 543

Aguado, D. S., Ahumada, R., Almeida, A., et al. 2019, ApJS, 240, 23

Allington-Smith, J., Murray, G., Content, R., et al. 2002, PASP, 114, 892

Amram, P., Sullivan, W. T., I., Balkowski, C., Marcelin, M., & Cayatte, V. 1993, ApJ, 403, L59

Andersen, D. R. & Bershady, M. A. 2013, ApJ, 768, 41

Avila-Reese, V., Firmani, C., & Zavala, J. 2002, in Astronomical Society of the Pacific Conference Series, Vol. 282, Galaxies: the Third Dimension, ed. M. Rosada, L. Binette, & L. Arias, 137

Bacon, R., Accardo, M., Adjali, L., et al. 2010, in Society of Photo-Optical Instrumentation Engineers (SPIE) Conference Series, Vol. 7735, Proc. SPIE, 773508

Bacon, R., Copin, Y., Monnet, G., et al. 2001, MNRAS, 326, 23

Bahé, Y. M., Barnes, D. J., Dalla Vecchia, C., et al. 2017, MNRAS, 470, 4186

Baldry, I. K., Bland-Hawthorn, J., & Robertson, J. G. 2004, PASP, 116, 403

Barden, S. C., Arns, J. A., & Colburn, W. S. 1998, in Society of Photo-Optical Instrumentation Engineers (SPIE) Conference Series, Vol. 3355, Proc. SPIE, ed. S. D'Odorico, 866–876

Barden, S. C., Arns, J. A., Colburn, W. S., & Williams, J. B. 2000, PASP, 112, 809

Bellstedt, S., Forbes, D. A., Romanowsky, A. J., et al. 2018, MNRAS, 476, 4543

Bershady, M. A., Verheijen, M. A. W., Swaters, R. A., et al. 2010, ApJ, 716, 198

Binney, J. 2010, MNRAS, 401, 2318

Binney, J. & Tremaine, S. 1987, Galactic dynamics

Blanton, M. R., Bershady, M. A., Abolfathi, B., et al. 2017, AJ, 154, 28

Bongard, S., Soulez, F., Thiébaut, É., & Pecontal, É. 2011, MNRAS, 418, 258

Bösch, B., Böhm, A., Wolf, C., et al. 2013, A&A, 549, A142

Bosma, A. 1981a, AJ, 86, 1791

Bosma, A. 1981b, AJ, 86, 1825

Bouché, N., Carfantan, H., Schroetter, I., Michel-Dansac, L., & Contini, T. 2015, AJ, 150, 92

Bourguignon, S., Carfantan, H., Slezak, , & Mary, D. 2011, in 2011 3rd Workshop on Hyperspectral Image and Signal Processing: Evolution in Remote Sensing (WHISPERS), 1–4

Bovy, J. 2014, ApJ, 795, 95

Bundy, K., Bershady, M. A., Law, D. R., et al. 2015, ApJ, 798, 7

Burgh, E. B., Bershady, M. A., Westfall, K. B., & Nordsieck, K. H. 2007, PASP, 119, 1069

Burgh, E. B., Nordsieck, K. H., Kobulnicky, H. A., et al. 2003, in Society of Photo-Optical Instrumentation Engineers (SPIE) Conference Series, Vol. 4841, Proc. SPIE, ed. M. Iye & A. F. M. Moorwood, 1463–1471

Cappellari, M. 2002, MNRAS, 333, 400

Cappellari, M. 2008, MNRAS, 390, 71

Cappellari, M. 2017, MNRAS, 466, 798

Cappellari, M., Bacon, R., Bureau, M., et al. 2006, MNRAS, 366, 1126

Cappellari, M. & Emsellem, E. 2004, PASP, 116, 138

Cappellari, M., Emsellem, E., Bacon, R., et al. 2007, MNRAS, 379, 418

Cappellari, M., Emsellem, E., Krajnović, D., et al. 2011, MNRAS, 413, 813

Cappellari, M., McDermid, R. M., Alatalo, K., et al. 2012, Nature, 484, 485

Cappellari, M., Romanowsky, A. J., Brodie, J. P., et al. 2015, ApJ, 804, L21

Cappellari, M., Scott, N., Alatalo, K., et al. 2013, MNRAS, 432, 1709

Chattopadhyay, S., Joshi, V., Ramaprakash, A. N., et al. 2018a, in Society of Photo-Optical Instrumentation Engineers (SPIE) Conference Series, Vol. 10706, Proc. SPIE, 107062D

Chattopadhyay, S., Ramaprakash, A. N., Joshi, B., et al. 2018b, Journal of Astronomical Telescopes, Instruments, and Systems, 4, 036002

Chattopadhyay, S., Ramaprakash, A. N., Khodade, P., et al. 2018c, in Society of Photo-Optical Instrumentation Engineers (SPIE) Conference Series, Vol. 10706, Proc. SPIE, 107065S

Choi, H. & Yi, S. K. 2017, ApJ, 837, 68

Choi, H., Yi, S. K., Dubois, Y., et al. 2018, ApJ, 856, 114

Choi, Y.-Y., Han, D.-H., & Kim, S. S. 2010, Journal of Korean Astronomical Society, 43, 191

Chung, H., Ramaprakash, A. N., Khodade, P., et al. 2018a, in Society of Photo-Optical Instrumentation Engineers (SPIE) Conference Series, Vol. 10702, Proc. SPIE, 107027A

Chung, H., Ramaprakash, A. N., Khodade, P., et al. 2018b, in Society of Photo-Optical Instrumentation Engineers (SPIE) Conference Series, Vol. 10702, Proc. SPIE, 107027U

Chung, H., Ramaprakash, A. N., Omar, A., et al. 2014, in Society of Photo-Optical Instrumentation Engineers (SPIE) Conference Series, Vol. 9147, Proc. SPIE, 91470V

Chung, H., Ramaprakash, A. N., & Park, C. 2015, Publication of Korean Astronomical Society, 30, 675

Cooley, J. W. & Tukey, J. W. 1965, Mathematics of computation, 19, 297

Corradi, R. L. M. & Capaccioli, M. 1990, A&A, 237, 36

Cortese, L., Fogarty, L. M. R., Bekki, K., et al. 2016, MNRAS, 463, 170

Courbin, F., Magain, P., Kirkove, M., & Sohy, S. 2000, ApJ, 529, 1136

Courteau, S. 1997, AJ, 114, 2402

Croom, S. M., Lawrence, J. S., Bland-Hawthorn, J., et al. 2012, MNRAS, 421, 872

Dale, D. A., Giovanelli, R., Haynes, M. P., Hardy, E., & Campusano, L. E. 2001, AJ, 121, 1886

Dawson, K. S., Schlegel, D. J., Ahn, C. P., et al. 2013, AJ, 145, 10

de Lorenzi, F., Debattista, V. P., Gerhard, O., & Sambhus, N. 2007, MNRAS, 376, 71

de Vaucouleurs, G., de Vaucouleurs, A., Corwin, Herold G., J., et al. 1991, Third Reference Catalogue of Bright Galaxies

Distefano, A., Rampazzo, R., Chincarini, G., & de Souza, R. 1990, A&AS, 86, 7

Dressler, A. 1980, ApJ, 236, 351

Dressler, A., Bigelow, B., Hare, T., et al. 2011, PASP, 123, 288

Dressler, A., Oemler, Augustus, J., Couch, W. J., et al. 1997, ApJ, 490, 577

Drory, N., MacDonald, N., Bershady, M. A., et al. 2015, AJ, 149, 77

Emsellem, E., Cappellari, M., Krajnović, D., et al. 2011, MNRAS, 414, 888

Emsellem, E., Cappellari, M., Krajnović, D., et al. 2007, MNRAS, 379, 401

Emsellem, E., Monnet, G., & Bacon, R. 1994, A&A, 285, 723

Faber, S. M. & Gallagher, J. S. 1979, ARA&A, 17, 135

Falcón-Barroso, J., Sánchez-Blázquez, P., Vazdekis, A., et al. 2011, A&A, 532, A95

Feng, J. Q. & Gallo, C. F. 2011, Research in Astronomy and Astrophysics, 11, 1429

Genel, S., Vogelsberger, M., Springel, V., et al. 2014, MNRAS, 445, 175

Girardi, L., Bressan, A., Bertelli, G., & Chiosi, C. 2000, A&AS, 141, 371

Gómez, P. L., Nichol, R. C., Miller, C. J., et al. 2003, ApJ, 584, 210

Graham, M. T., Cappellari, M., Li, H., et al. 2018, MNRAS, 477, 4711

Greene, J. E., Leauthaud, A., Emsellem, E., et al. 2018, ApJ, 852, 36

Gunn, J. E., Siegmund, W. A., Mannery, E. J., et al. 2006, AJ, 131, 2332

Henault, F., Bacon, R., Bonneville, C., et al. 2003, in Society of Photo-Optical Instrumentation Engineers (SPIE) Conference Series, Vol. 4841, Proc. SPIE, ed. M. Iye & A. F. M. Moorwood, 1096–1107

Hernquist, L. 1990, ApJ, 356, 359

Hopkins, P. F., Bundy, K., Hernquist, L., Wuyts, S., & Cox, T. J. 2010, MNRAS, 401, 1099

Houghton, R. C. W., Davies, R. L., D'Eugenio, F., et al. 2013, MNRAS, 436, 19

Jeans, J. H. 1922, MNRAS, 82, 122

Jesseit, R., Cappellari, M., Naab, T., Emsellem, E., & Burkert, A. 2009, MNRAS, 397, 1202

Kalinova, V., Colombo, D., Rosolowsky, E., et al. 2017, MNRAS, 469, 2539

Kauffmann, G., White, S. D. M., Heckman, T. M., et al. 2004, MNRAS, 353, 713

Kelz, A., Verheijen, M. A. W., Roth, M. M., et al. 2006, PASP, 118, 129

Kent, S. M. 1987, AJ, 93, 816

Kronberger, T., Kapferer, W., Unterguggenberger, S., Schindler, S., & Ziegler, B. L. 2008, A&A, 483, 783

Lagos, C. d. P., Schaye, J., Bahé, Y., et al. 2018, MNRAS, 476, 4327

Law, D. R., Cherinka, B., Yan, R., et al. 2016, AJ, 152, 83

Law, D. R., Yan, R., Bershady, M. A., et al. 2015, AJ, 150, 19

Le Fèvre, O., Vettolani, G., Garilli, B., et al. 2005, A&A, 439, 845

Lee, J. C., Hwang, H. S., & Chung, H. 2018, MNRAS, 477, 1567

Lewis, I., Balogh, M., De Propris, R., et al. 2002, MNRAS, 334, 673

Li, H., Li, R., Mao, S., et al. 2016, MNRAS, 455, 3680

Li, R., Li, H., Shao, S., et al. 2019, arXiv e-prints, arXiv:1903.09282

Long, R. J. & Mao, S. 2010, MNRAS, 405, 301

Lucy, L. B. 1974, AJ, 79, 745

Lucy, L. B. & Walsh, J. R. 2003, AJ, 125, 2266

Ma, C.-P., Greene, J. E., McConnell, N., et al. 2014, ApJ, 795, 158

Magain, P., Courbin, F., & Sohy, S. 1998, ApJ, 494, 472

Mathewson, D. S., Ford, V. L., & Buchhorn, M. 1992, ApJS, 81, 413

Merritt, D., Graham, A. W., Moore, B., Diemand , J., & Terzić, B. 2006, AJ, 132, 2685

Milgrom, M. 1983, ApJ, 270, 365

Monaghan, J. J. & Lattanzio, J. C. 1985, A&A, 149, 135

Monnet, G., Bacon, R., & Emsellem, E. 1992, A&A, 253, 366

Naab, T., Oser, L., Emsellem, E., et al. 2014, MNRAS, 444, 3357

Nair, P. B. & Abraham, R. G. 2010, ApJS, 186, 427

Navarro, J. F., Frenk, C. S., & White, S. D. M. 1996, ApJ, 462, 563

Noordermeer, E., van der Hulst, J. M., Sancisi, R., Swaters, R. S., & van Albada, T. S. 2007, MNRAS, 376, 1513

Omar, A., Yadav, R. K. S., Shukla, V., Mondal, S., & Pant, J. 2012, in Society of Photo-Optical Instrumentation Engineers (SPIE) Conference Series, Vol. 8446, Proc. SPIE, 844614

Park, C. & Choi, Y.-Y. 2005, ApJ, 635, L29

Park, C. & Choi, Y.-Y. 2009, ApJ, 691, 1828

Park, C., Gott, J. Richard, I., & Choi, Y.-Y. 2008, ApJ, 674, 784

Park, C. & Hwang, H. S. 2009, ApJ, 699, 1595

Pedrosa, S., Tissera, P. B., Fuentes-Carrera, I., & Mendes de Oliveira, C. 2008, A&A, 484, 299

Penoyre, Z., Moster, B. P., Sijacki, D., & Genel, S. 2017, MNRAS, 468, 3883

Persic, M. & Salucci, P. 1988, MNRAS, 234, 131

Portail, M., Wegg, C., Gerhard, O., & Martinez-Valpuesta, I. 2015, MNRAS, 448, 713

Postman, M. & Geller, M. J. 1984, ApJ, 281, 95

Press, W. H., Teukolsky, S. A., Vetterling, W. T., & Flannery, B. P. 2007, Numerical recipes 3rd edition: The art of scientific computing (Cambridge university press)

Puech, M., Flores, H., Hammer, F., et al. 2008, A&A, 484, 173

Richardson, W. H. 1972, Journal of the Optical Society of America (1917-1983), 62, 55

Roberts, M. S. & Whitehurst, R. N. 1975, ApJ, 201, 327

Rodet, T., Orieux, F., Giovannelli, J.-F., & Abergel, A. 2008, IEEE Journal of Selected Topics in Signal Processing, 2, 802

Rubin, V. C., Burstein, D., Ford, W. K., J., & Thonnard, N. 1985, ApJ, 289, 81

Rubin, V. C., Ford, W. K., J., & Thonnard, N. 1980, ApJ, 238, 471

Rubin, V. C. & Ford, W. Kent, J. 1970, ApJ, 159, 379

Rubin, V. C., Whitmore, B. C., & Ford, W. Kent, J. 1988, ApJ, 333, 522

Sagar, R., Kumar, B., Omar, A., & Pand ey, A. K. 2012, in Society of Photo-Optical Instrumentation Engineers (SPIE) Conference Series, Vol. 8444, Proc. SPIE, 84441T

Sánchez, S. F. 2006, Astronomische Nachrichten, 327, 850

Sánchez, S. F., García-Benito, R., Zibetti, S., et al. 2016, A&A, 594, A36

Sánchez, S. F., Kennicutt, R. C., Gil de Paz, A., et al. 2012, A&A, 538, A8

Sánchez-Blázquez, P., Peletier, R. F., Jiménez-Vicente, J., et al. 2006, MNRAS, 371, 703

Sandin, C., Becker, T., Roth, M. M., et al. 2010, A&A, 515, A35

Schaye, J., Crain, R. A., Bower, R. G., et al. 2015, MNRAS, 446, 521

Schwarzschild, M. 1979, ApJ, 232, 236

Schwarzschild, M. 1982, ApJ, 263, 599

Scott, N., van de Sande, J., Croom, S. M., et al. 2018, MNRAS, 481, 2299

Sharp, R. & Birchall, M. N. 2010, , 27, 91

Sharples, R., Bender, R., Agudo Berbel, A., et al. 2013, The Messenger, 151, 21

Shepp, L. A. & Vardi, Y. 1982, IEEE Transactions on Medical Imaging, 1, 113

Simard, L., Mendel, J. T., Patton, D. R., Ellison, S. L., & McConnachie, A. W. 2011, ApJS, 196, 11

Smee, S. A., Gunn, J. E., Uomoto, A., et al. 2013, AJ, 146, 32

Sofue, Y. & Rubin, V. 2001, ARA&A, 39, 137

Sofue, Y., Tutui, Y., Honma, M., et al. 1999, ApJ, 523, 136

Song, H., Park, C., Lietzen, H., & Einasto, M. 2016, ApJ, 827, 104

Soulez, F., Bongard, S., Thiebaut, E., & Bacon, R. 2011, in 2011 3rd Workshop on Hyperspectral Image and Signal Processing: Evolution in Remote Sensing (WHISPERS), 1–4

Sperandio, M., Chincarini, G., Rampazzo, R., & de Souza, R. 1995, A&AS, 110, 279

Srivastava, M. K., Ramaprakash, A. N., Das, H. K., et al. 2011, MNRAS, 418, 1127

Swaters, R. A., Sancisi, R., van Albada, T. S., & van der Hulst, J. M. 2009, A&A, 493, 871

Syer, D. & Tremaine, S. 1996, MNRAS, 282, 223

van de Sande, J., Bland-Hawthorn, J., Fogarty, L. M. R., et al. 2017, ApJ, 835, 104

Vazdekis, A., Casuso, E., Peletier, R. F., & Beckman, J. E. 1996, ApJS, 106, 307

Vazdekis, A., Sánchez-Blázquez, P., Falcón-Barroso, J., et al. 2010, MNRAS, 404, 1639

Veale, M., Ma, C.-P., Greene, J. E., et al. 2017, MNRAS, 471, 1428

Villeneuve, E. & Carfantan, H. 2014, IEEE Transactions on Image Processing, 23, 4322

Vogt, N. P., Haynes, M. P., Giovanelli, R., & Herter, T. 2004, AJ, 127, 3325

Wake, D. A., Bundy, K., Diamond-Stanic, A. M., et al. 2017, AJ, 154, 86

Whitmore, B. C. 1984, ApJ, 278, 61

Whitmore, B. C., Forbes, D. A., & Rubin, V. C. 1988, ApJ, 333, 542

Wiegert, T. & English, J. 2014, , 26, 40

Yan, R., Bundy, K., Law, D. R., et al. 2016a, AJ, 152, 197

Yan, R., Tremonti, C., Bershady, M. A., et al. 2016b, AJ, 151, 8

Appendix A

MaNGA IFU and Data Reduction

A.1 MaNGA IFU

IFS instruments adopt several concepts to realize the spatially resolved spectroscopy (e.g. lenslet only - SAURON (Bacon et al. 2001), lenslet+fiber - GMOS (Allington-Smith et al. 2002), image slicer - MUSE (Bacon et al. 2010)) MaNGA utilizes a bare-fiber based (without lenslet) IFU, primarily to exploit the existing SDSS fiber cartridge system and the BOSS spectrograph. MaNGA IFU has a hexagonal shape, and fibers are packed regularly by making a hexagonal shape rings with respect to the inner fibers. MaNGA science IFUs have a five sizes with different field of view to adapt the various angular size distribution of the target galaxies. Likewise other single-fiber based SDSS spectroscopic surveys, MaNGA IFUs are also plugged into the pre-drilled 3 degree field of view plate. There are 6 sets of MaNGA IFUs thus six different plate can be observed in a single night utilizing the existing fiber cartridge changing system. Size distribution of MaNGA IFUs can be found in Figure A.1. The distribution is determined along with the MaNGA survey design to achieve the survey goal and maximize the survey efficiency. In addition to the science IFUs, there are mini-bundle (7-fiber IFU) and sky fibers for the calibration purpose. Mini-bundles (12 mini-bundles for each set of IFUs)

are targeting the standard stars on the plate for the purpose of flux calibration as well as PSF measurement. Due to the wide field of view of the 2.5m telescope, the mini-bundles are distributed across the entire plates. Sky fibers are nearly identical to the BOSS single fiber. Each science IFU (and mini-bundle) has designated sky fibers, which can be plugged around them. The number of associated sky fibers per IFU varies with the number of fiber per a IFU (for 7, 19, 37, 61, 91, and 127 fiber IFUs, 1, 2, 2, 4, 6, and 8 sky fibers respectively). On the other side of the IFUs, fibers are comprising two sets of fiber slit and the light from the slits are dispersed by BOSS spectrographs. Note that the total number of MaNGA fibers is 1,423 which is about 40% larger than the total number of fibers of other surveys utilizing BOSS spectrographs. This was made possible by more closely packed fiber on the fiber slit. For the other survey each fiber observes physically different objects therefore the fibers should be separated enough to minimize the fiber cross-talk (Overlap of fiber images) on the CCD. However, this limitation can be relaxed for the MaNGA where the fibers are arranged in a way that adjacent fibers on the slit are also adjacent in the sky (i.e. observing objects which are already somewhat correlated). Due to the hexagonal arrangement of fibers, fill factor of MaNGA IFU is only about 56%. To fill the physical gap between fibers, MaNGA targets are observed with 3-point dithering. Thus a set of MaNGA observation is composed to three 15-minutes exposures. During the observation, the quick reduction pipeline monitor the data quality and run an additional 45-minutes exposure on a plate to achieve S/N goals(three to four sets per plate on average).

A.2 Data Reduction

MaNGA data reduction process is similar to the reduction of conventional SDSS spectroscopic observation date but with one additional step, cube generation. In the first stage, the observed data is reduced by the MaNGA data reduction pipeline (DRP) 2D stage which is reducing individual fiber spectra like BOSS IDLSPEC2D pipeline (Dawson et al. 2013). This stage includes sky subtraction and flux calibration that use information from the standard star observation by 12 mini-bundles and the sky fibers. In

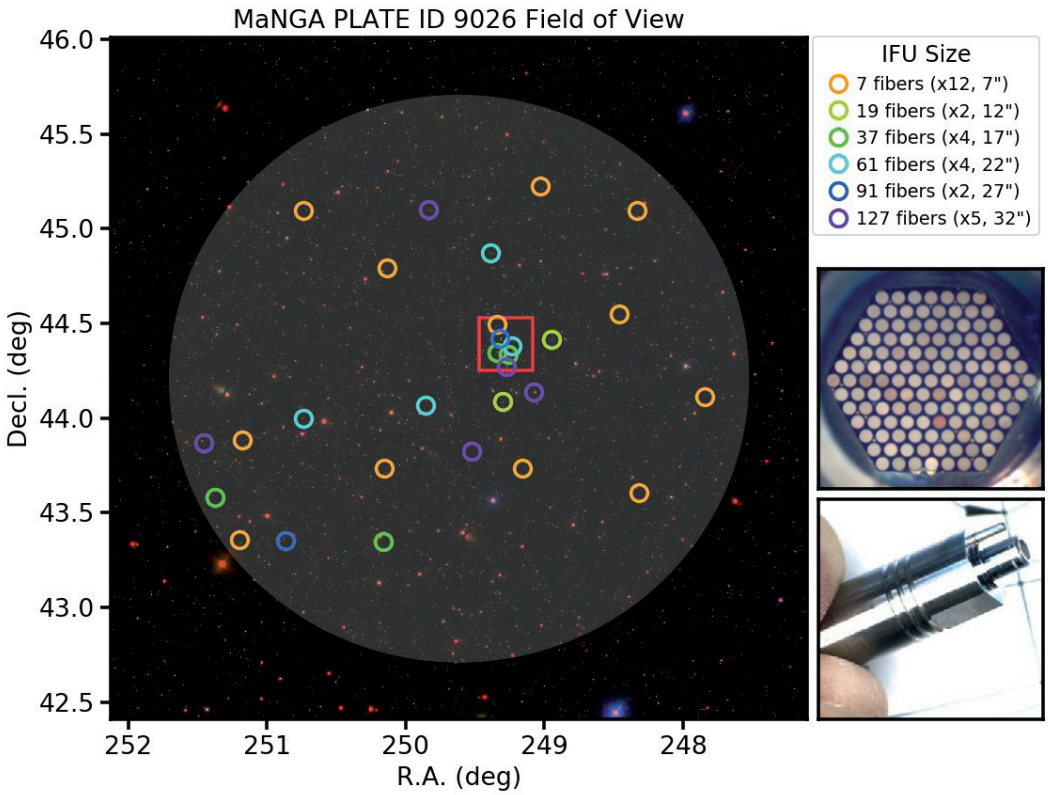

Figure A.1. (left) Distribution of MaNGA IFUs on the MaNGA PLATE ID 9026. The grey background circle represents 3° field of view of the MaNGA plate (Plate center R.A./Dec. (in J2000): 249.6149/44.2073). The legend shows the number of IFUs and field of view per each IFU size.) Red square denotes the region of Figure A.2. (middle right) A face of a proto-type 127-fiber IFU. (bottom right) Image of IFU ferrule housing. A guide rod on the ferrule is used to put the IFU with desired orientation. IFU images are taken from SDSS web-page[a], following the image use policy[b].

[a]https://www.sdss.org/instruments/manga-instrument/
[b]https://www.sdss.org/collaboration/image-use-policy/

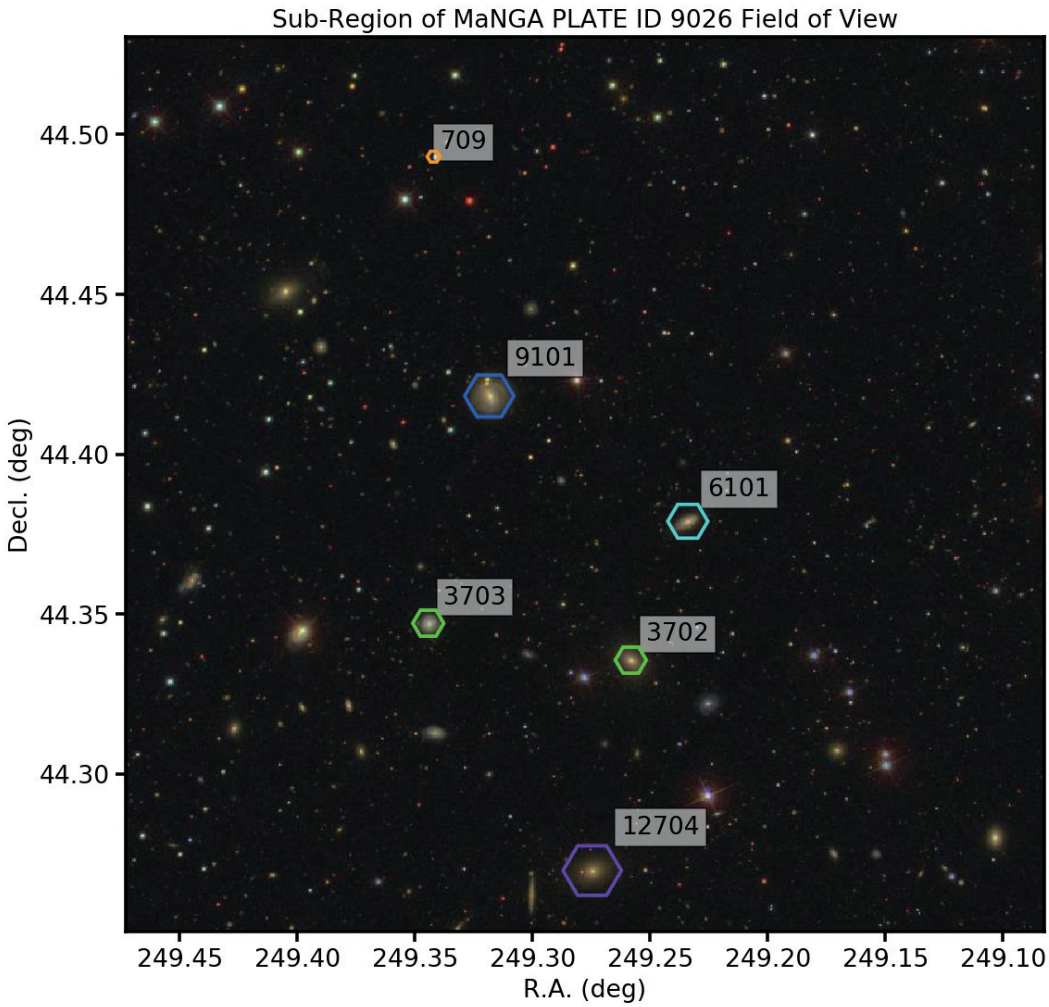

Figure A.2. Distribution of MaNGA IFUs on the sub-region of MaNGA PLATE ID 9026. Colors represent the size of IFU as in Figure A.1. IFU design ID is also shown at the top right of each IFU. Outline of hexagonal shape is two times larger than the actual size for better visibility.

the second stage (3D stage), individual fiber spectra are combined to generate 3D data cube with the knowledge of fiber bundle metrology, dithering offset, field/chromatic differential refraction, and other necessary factors. During the 3d stage, the spectra are spatially resampled in a regular bin size of $0.5''$. The modified Shepard's method is adopted as a resampling algorithm. The method uses a circular Gaussian kernel as a weighting function (scale length of $0.7''$) with an upper limit of the radius of influence as $1.6''$. In the wavelength direction, the spectrum is binned in two different spaces, a decadal logarithmic and a linear. The logarithmically binned wavelength spans from 3621.5960 to 10353.8054 Å or from 3.5589 to 4.0151 in the logarithmic grid with 0.0001 steps (4563 wavelength bins). The linearly binned wavelength spans from 3622 to 10353 Å with 1 Å interval (6732 wavelength bins).

Appendix B

DOTIFS Overview, Optical System, and Software

B.1 Instrument Overview

DOTIFS is mainly composed of four parts: fore-optics, integral-field-units (IFUs), IFU deployment system, and spectrographs. The fore-optics enlarges the telescope's focal plane and modifies the plate scale to match the image resolution with physical size of the microlenses. IFUs gather lights from the focal plane and transfer them to the spectrograph via optical fibers.

In Figure 1.2, the light coming from the telescope is directed to the Cassegrain side port by telescope tertiary mirror. It passes DOTIFS fore-optics, which slows down focal ratio (F-ratio) of the light and forms magnified $8'$ focal plane. IFU deployment system allocates 16 IFUs on the focal plane, and the IFUs gather light from the observation targets on the sky. Each IFU has $8.7'' \times 7.4''$ field of view with fiber-coupled 12×12 hexagonal aperture shape microlens array. The other end of the fibers are connected to the entrance of 8 identical spectrographs, and the spectrographs disperse light over 370 to 740 nm wavelength range simultaneously in a single exposure. The spectrographs are mounted on the telescope Cassegrain port rather than a gravitationally invariant area to minimize fiber length and therefore maximize the throughput. They occupy the

remaining space around the telescope direct port instrument, ARIES Devasthal Faint Object Spectrograph Camera (ADFOSC, Omar et al. 2012). We briefly describe each subsystem of DOTIFS below.

- Fore-Optics and Calibration Unit

  The original plate scale at the Cassegrain focal plane of the 3.6m telescope is $1''$ per $157\mu m$. The physical size of $0.8''$ with the original plate scale is $126\mu m$, which too small to put microlens-fiber based sampling element. Therefore, a fore-optics is introduced to modify the plate scale so combination of a microlens and a fiber can be matched with the desired sampling size. The calibration unit shares lenses with the fore-optics to mimic the light from calibration sources as the beam from the telescope.

- Integral Field Unit

  IFUs are one of the most import parts of DOTIFS which capture light from an "area" of the sky and transfer them to the spectrographs. Each IFU of DOTIFS is comprised of a 12×12 array of hexagonal shaped microlens and 144 optical fibers which are coupled to the microlens array. The fibers are attached at the back focus of the microlenses and deliver light from each lens to the designated spectrograph. The physical size of the hexagonal microlens is 300 μm from vertex to vertex. The F/4.5 plano-convex microlens forms 84 μm diameter pupil at their back focus where fibres are in optical contact. The optical path inside the microlens is depicted in the Figure 2 of Chung et al. (2014). We use 100 μm cose diameter, N.A. = 0.12 fiber from CeramOptec. Multiple fibre samples were tested in the lab for their input F-ratio as well as focal ration degradation FRD) effect. A new photolithography based technique has been employed for production of the IFUs (Chattopadhyay et al. 2018a).

- IFU Deployment System

  The IFU deployment system is technically the most challenging part of DOTIFS.

A combination of two linear actuators are used for the movement of each IFU in X and Y direction. With a novel deployment algorithm (Chattopadhyay et al. 2018c), the system can deploy IFUs at the exact position (less than 10% of the sampling element size) on the focal plane efficiently, quickly, and safely without collision or other damage.

- Spectrograph

  Eight identical DOTIFS spectrographs deliver spectra of 2304 optical fibers with the desired spectral resolution. Each spectrograph optics is composed of fiber slit, F/4 collimator, volume phase holographic (VPH) grating, F/1.5 camera, and 4K by 2K CCD. The combination of VPH grating and the high throughput optics enables relatively high throughput spectrograph optics. A broadband filter is positioned between the last lens of the collimator and the pupil. The filter is inclined by 10 degrees to minimize the reflection ghosts. The VPH grating is located slightly behind the filter to be served as a dispersion element. The graded-coated CCD is used to maximize the throughput.

The following specifications are determined from the requirements set by the science cases (section 1.4).

- Wavelength coverage: 370 nm - 740nm

  The shortest wavelength has been set by OII doublet, which is one of the major star formation indicators located at the wavelength of 372.7nm in the rest frame. The longest wavelength is forced to double of the shortest wavelength, to avoid the second-order contamination. In this wavelength range, DOTIFS could detect OIII lines from z$\sim$0.4 galaxies.

- Spectral resolution: R = 1500 - 1800

  Many science cases require the ability to measure the velocity dispersion of galaxies. Observations of narrow line regions of the active galactic nuclei (AGNs) and rotation velocity measurement of the spiral galaxies can be made with R = 1500 - 1800. It also enables to separation of Hβ and OIII lines in the blue region.

- Spatial resolution: $0.8''$, vertex to vertex in hexagonal shape

  The spatial resolution of DOTIFS is set to match with the median seeing at the observing site, which is about $0.8''$. The tightly coupled relations between physical parameters of the input and output beams (F-ratio, beam size), microlens (size, F-ratio), and optical fiber (size, critical angle), also affects the realistically achievable spatial resolution. This spatial resolution resolves about 50 pc at a distance of 10 Mpc and this is sufficient to study regions of primary interests eg; NLR of AGNs, Giant HII regions, and starburst nuclear ring which lie in the range of hundreds to thousands parsecs.

- Field of view: $8.7'' \times 7.4''$ (IFU), $8'$ (deployable field)

  Since the typical sizes of the biggest luminous infrared galaxies at 100 Mpc is about $40'' \times 40''$, IFU should be able to cover about $50'' \times 50''$ area. At the same time, to study the HII region structures in nearby galaxies or to observe multiple targets in a single exposure, multiple narrow field of view IFUs are preferred than a single wide field of view IFU. In addition, considering physical constraints of the spectrograph, one spectrograph could accommodate $\sim$300 fibres. Given these considerations, each IFU is composed of 144 (12×12) spaxel elements, which correspond to $8.7'' \times 7.4''$ on the sky. Each spectrograph can then cover fibres from two independent IFUs. The size of the deployable area is determined by the field of view of the telescope side port, the physical size of the IFU deployable area, and the optical performance of the fore-optics. Considering all constraints, we get about $8'$ diameter circular field as the instrument field of view. This field is also comparable to the size of the optical disks of nearby galaxies.

- Number of spatial elements: 2304

  The number of spatial elements is constrained by the budget and the available space around the telescope Cassegrain main port. Since we are able to accommodate up to eight spectrographs and one spectrograph can cover fibers from 2 IFUs, the number of spatial elements is determined as 2304.

- Throughput: 20%

  The sensitivity requirement of DOTIFS is 10^{-16} erg/cm^2/s/Å/$''$. Calculation shows that the instrument (from the telescope to the spectrograph CCD) needs more than 20% total throughput to achieve an emission line S/N$\sim$5 with one hour exposure,

B.2 Optical System

B.2.1 Fore-Optics

The instrument requires the fore-optics system to deliver appropriate light into IFUs so they can be transferred to the spectrograph optics properly (Chung et al. 2018b). F-ratio of the light from the telescope primary and secondary mirrors is not proper to be accepted by IFUs. Thus a set of optics are required to modify the light appropriately. Figure B.1 shows an opto-mechanical overview of DOTIFS side port subsystem. Fore-optics and calibration unit are combined as an integrated module. It is attached directly to the Cassegrain side port entrance.

Design goals

We design DOTIFS fore-optics to match plate scale on the focal plane to the microlens sampling size. DOTIFS requires a fore-optics to match IFUs with the original telescope plate scale, which is 157 $\mu m/''$. To work without fore-optics, the physical size of one IFU would be only 1.37 mm $\times$ 1.16 mm, and the size of each microlens would be 125.6 μm. Considering available diameter of the optical fiber, packing fibers with 125.6 μm spacing is physically not feasible. Thus, we need to modify the plate scale on the focal plane and increase the physical size of the microlens accordingly. Our choice is using fore-optics to modify that plate scale on the focal plane to 300 $\mu m/0.8''$. This corresponds to the F-ratio of 21.486. The optical performance of the fore-optics magnifier should be good enough to make image quality captured by IFU to be limited by sampling size. Root-Mean-Square (RMS) spot radius size less than 50 μm is estimated to satisfy

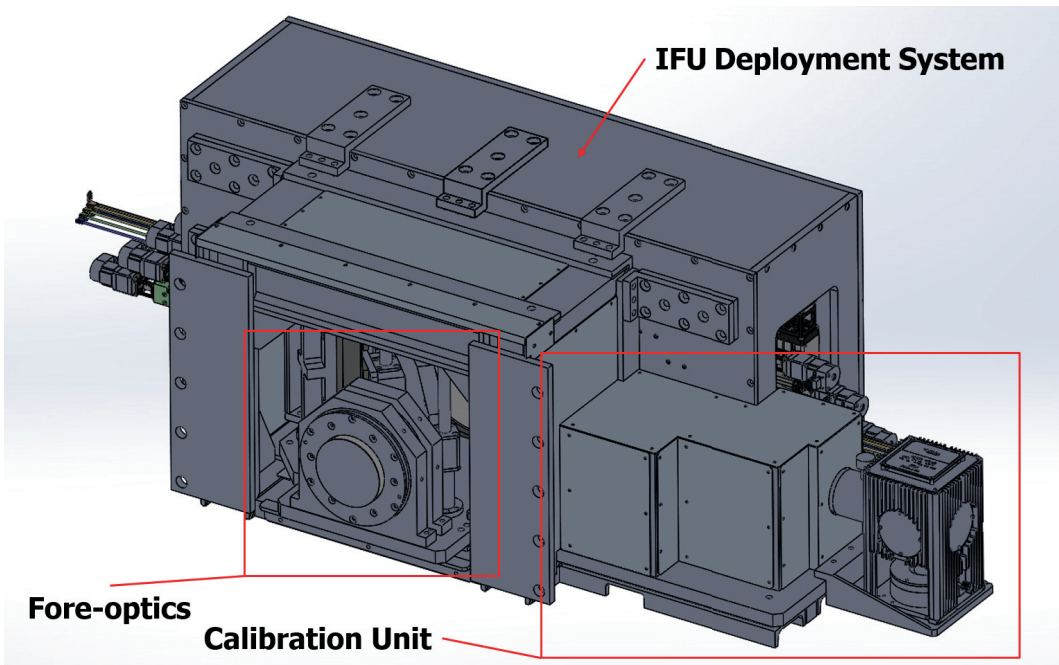

Figure B.1. Overall mechanical rendering of DOTIFS subsystems, positioned at the telescope Cassegrain side port. Each subsystem is pointed out with red arrows.

the optic performance requirement. More than 80% of the energy from a $2''$ size source should be contained within the 750 μm hexagonal area at the microlens array surface, which corresponds to 2.5 times of spatial sampling size. The optics should have a field of view as wide as possible while maintaining homogeneous imaging quality over the entire focal plane. Also, the output beam should be telecentric so incidence angle of the light to each IFU would not change over the optics field of view.

Optical design

We design fore-optics to refract telescope F/9 beam to F/21.486 telecentric beam. It changes plate scale on the focal plane from 157 μm / 1 $''$ to 300 μm / $0.8''$. This is about 2.39 times of magnification. Original telescope field of view is known as $10'$ at the Cassegrain side port, but we utilize $8'$ of them. We use the optical layout of the 3.6m DOT to start fore-optics design and put several plane elements near the original focal plane as a starting design. We set merit function as a sum of RMS spot radius of three different wavelengths and five field points. Also, effective focal length is constrained to match the desired plate scale. We add several operands to make telecentric beam at the focus. We constrain the lens positions to be around the position of the original focal plane since we can put optics only around the Cassegrain side port space. During the optimization, we manually add or subtract a lens element to find the optimal solution. The design (Figure B.2) is comprised of five singlets, all spherical lenses. Three relatively small singlets are located close to the side port entrance, and two large singlets are located just before the focal plane. We have two Calcium Fluoride (CaF_2) component to maximize the throughput at the near-UV (370 – 400 nm) wavelength range.

In Figure B.3, we show spot diagram and wavelength versus RMS spot radius graph of the fore-optics. The diameter of a black circle around each spot is 300 μm, which represent a size of one microlens. An actual microlens is a hexagonal shape with 300 μm vertex to vertex, which is slightly smaller than the black circle in the diagram. In general, the spots are well shaped and concentrated at the center, but their size is increasing as the location of field point gets further from the center. We find that

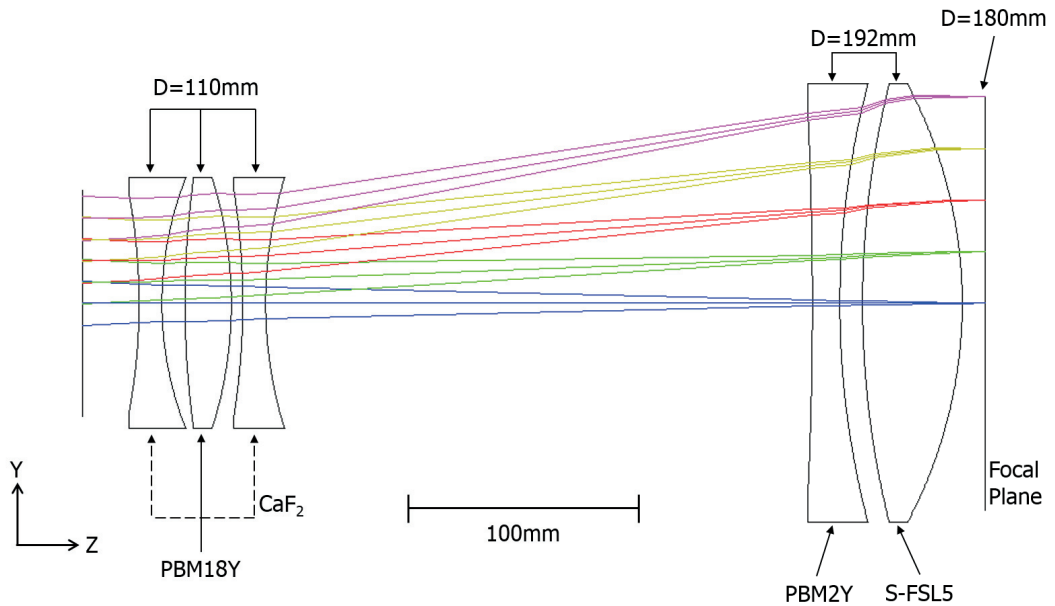

Figure B.2. Fore-optics layout. Diameter and glass material of each component is shown. Different color lines represent light from five different field points. (0, 1, 2, 3, and 4 (′))

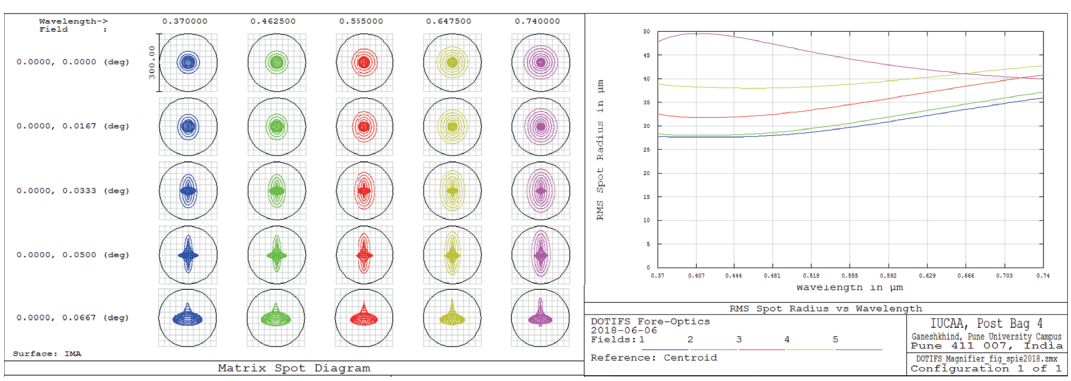

Figure B.3. (Left) Matrix spot diagram of the fore-optics. Color represents different wavelength. (Right) Wavelength versus RMS spot radius plot. Color represents the light of different field points, as in the top of the bottom rows of the left figure.

this change is inevitable by doing magnification at the very end of converging light. There could be some effect on IFU imaging quality near the edge of the field, which needs to be mitigated by post-processing. There is also chromatic dispersion between the center and the edge of the 8′ diameter field, which requires proper calibration and post-processing. Since the IFU field of view is less than 10″, there will be negligible chromatic dispersion effect within a single IFU.

B.2.2 Calibration Unit

DOTIFS requires a designated calibration system since the telescope does not have a calibration system to be used by DOTIFS spectrograph (Chung et al. 2018b). By having a dedicated calibration unit, we can choose proper light source which is optimized to calibrate the DOTIFS spectrograph. Figure B.5 shows an top-view of the DOTIFS side port subsystem opto-mechanics. It shows the arrangement of calibration sub-components and the location of elliptical movable mirror which can switch the source of light enter to the focal plane.

Design goals

We design DOTIFS calibration unit to provide a telescope-alike beam to the focal plane from calibration light sources. CCD image of integral field spectrograph is complex. Thus a precise calibration process to obtain high-quality data is required. Major calibration sources are continuum source and emission line source. Continuum source is used to map the position of the spectrum from each spatial elements (fibers), and emission line source is used to map the pixel location in a spectral direction to the wavelength. Geometrical property of the light from those calibration sources should be identical to the one from telescope and fore-optics, to have no systematic difference in between.

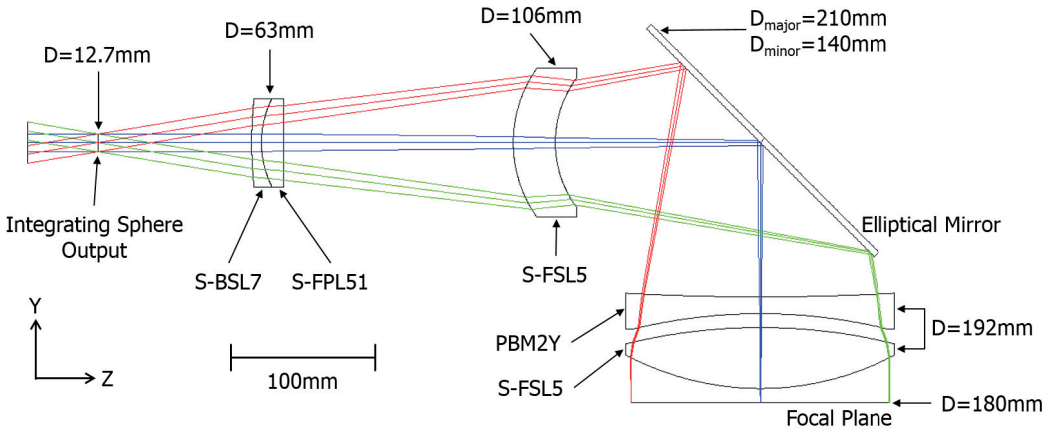

Figure B.4. Layout of calibration unit optics. Elements from the integrating sphere output to the focal plane is shown. Diameter and glass material of each component are labeled with black arrows. The last two lenses in this diagram are identical to the last two lenses in Figure B.2. Different color lines represent light from different angles

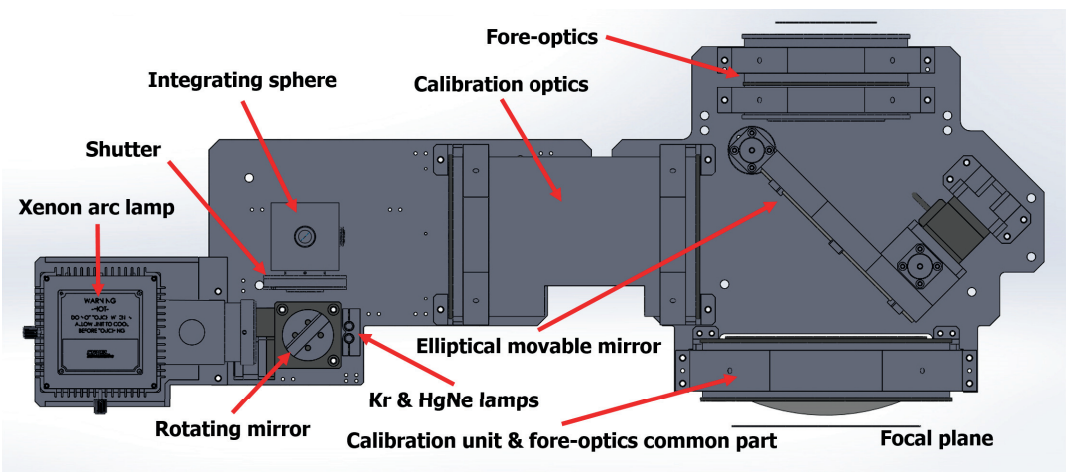

Figure B.5. Top-view of DOTIFS fore-optics and calibration unit opto-mechanical structure. Location of subcomponents is pointed out with red arrows. Covers are removed to show internal components. The elliptical movable mirror can be retracted to the out of paper direction by linear guideway stage.

Calibration sources and integrating sphere

DOTIFS uses Xenon arc lamp (Newport part #6263) as a continuum source. We choose Xenon arc lamp because of its relatively flat radiation curve within the DOTIFS working wavelength range, compare to the traditional continuum sources such as quartz lamp or halogen lamp. It is expected to provide sufficient photons in the near UV range as well. Also, calibration with a continuum source can be done in seconds since the lamp has sufficient power. Krypton (Kr) and Mercury-Neon (HgNe) lamp (Newport part #6031 and #6034) are chosen as wavelength calibration sources, considering there emission line profiles and DOTIFS working wavelength range. The original supplier of all three lamps is Oriel Instrument which is a well-known lamp manufacturer in the field of astronomical instrumentation. We also employ a small integrating sphere (Newport part #819D-SL-2) to scramble the light from calibration source and provide uniform and collimated light to the calibration optics.

Optical design

Light from calibration sources enters to the integrating sphere. The output light from the sphere is considered as a uniform light source and used as an object of calibration optics. Considering limited space around the focal plane which IFUs are deployed, calibration optics and fore-optics are designed to use two lenses in common, which are components just before the focal plane (Figure B.4). We utilize available space of the Cassegrain side-port area and the gap among the fore-optics elements to locate remaining calibration optics. The movable large elliptical mirror is placed between the third and fourth lenses of the fore-optics lens and acting as a calibration source selector. One doublet and one singlet are placed next to the integrating sphere output as a dedicated calibration optics. The combination of optical components produces F/21.486 light at the fore-optics focal plane.

Calibration Scheme

Here we describe fundamental calibration scheme of DOTIFS. In principle, each science exposure requires two sets of calibration exposure, before and after the target observation. This is to have highest calibration accuracy as well as to trace possible flexure effect during the science exposure. One set of calibration exposure is comprised of one flat field image (with continuum source) and one wavelength calibration image. (With wavelength calibration sources). We make simulated calibration exposure images from DOTIFS data simulator (Chung et al. 2015), using known throughput of the instrument and radiation curve of continuum and emission line sources (Figure B.13 and B.14). At each calibration exposure, Xenon lamp will be turned on for few minutes ahead to be stabilized. A shutter near the integrating sphere input port will be closed during this warm-up phase. When Xenon lamp becomes stabilized, the shutter will be opened, and the elliptical mirror will be placed between the fore-optics lenses to block the light from the telescope. Continuum source image will be taken when everything is ready. After that, the arc lamp will be turned off, and wavelength calibration lamps will be turned on to take wavelength calibration source image. After taking two calibration images, the shutter will be closed, and the elliptical mirror is moved out so the next science exposure can be made.

B.2.3 Spectrograph

DOTIFS spectrograph is all-refractive, fixed configuration optics optimized to focus images of fibers on the CCD. Combination of high transmission glasses, volume phase holographic grating, and the graded-coated CCD yields the high optics throughput (Chung et al. 2018a). All-spherical lens surfaces reduces the fabrication cost as well as enables doable optical alignment. Figure B.6 shows the overall opto-mechanical structure of the spectrograph.

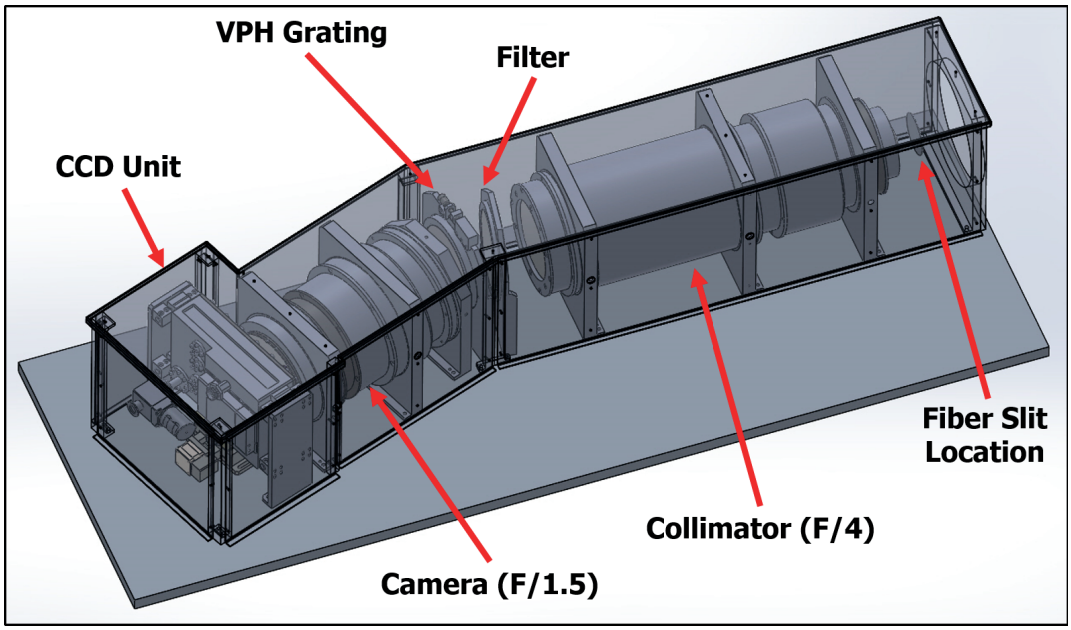

Figure B.6. Opto-mechanical structure of DOTIFS spectrograph. Location of sub-components is pointed out with red arrows. CCD dewar is not shown in this figure.

Design Goals

We describe design goals of the spectrograph optics below. We explain concerns or issues regarding each goal as well.

- Wavelength coverage from 370 nm to 740 nm

  The wavelength coverage affects available optics material choices while designing optics. This range is mostly in the visible region, and there are diverse kinds of glass with good transmission in the visible range. However, there are only a few glasses with high transmission ($>$ 99.5 %/10 mm) at near-UV range (370 to 400nm). A small difference in transmission (%/10 mm) ends up with a huge amount of light loss because the light loss is increasing exponentially as optics size becomes big. It leads us to use CaF_2 and other high UV throughput i-line glass materials which have transmission higher than 99.5 %/10 mm. An option for splitting wavelength range with a dichroic element was rejected since a single-arm spectrograph can satisfy the required wavelength range and spectral resolution.

- Spectral resolution of R∼1500-1800

  The requirement of R∼1800 at the central wavelength demands a dispersion of 0.00822 nm/μm, assuming 2.5 pixels sampling per spectral element. 2.5 pixels corresponds to 37.5 μm with 15 μm size pixel, and this will be the size of fiber image on the detector. Since the diameter of the fiber is specified as 100 μm and an angle of light coming out of fiber is about F/4, it leads spectrograph optics to have F/4 collimator and F/1.5 camera. Wavelength coverage from 370 nm to 740 nm corresponds to 3000 pixels on the detector with required dispersion.

- $>$ 80% Ensquared energy within 2.5 pixels from monochromic 100 μm size, circular, and NA=0.125 light

  This is a performance requirement of the optics. Low ensquared energy per sampling leads lower spectral resolution than expected, as well as increasing cross-talk between lights from adjacent fibers. Optics should be well designed to achieve required ensquared energy specification. Also, this requirement should be fulfilled over the entire field points since spectra of fibers are equally important.

- Average throughput $>$ 35%

  DOTIFS sensitivity requirement (emission line S/N $\sim$ 5) from one-hour exposure sets throughput budget for each sub-system. Throughput higher than 35% for spectrograph optics is required to fulfill the budget. The throughput includes throughput of the collimator, filter, grating, camera and CCD quantum efficiency.

Base design

DOTIFS spectrograph optics is designed based on South African Large Telescope Robert Stobie Spectrograph (SALT RSS) optical design. We studied this design as one of starting design candidates and chose as final one because of its similar optical characteristic to requirements of DOTIFS spectrograph. Details of SALT RSS design including optics prescription are described in its optics design paper (Burgh et al. 2003). SALT RSS is an imaging spectrograph with long-slit and multi-slit spectroscopy and

Fabry-Perot imaging spectroscopy capabilities. Unlike other conventional slit spectrographs, this spectrograph is designed for fast input beam (F/4.2). It also has a fast F/2.2 camera with wide a field of view as well as wide wavelength coverage. Since DOTIFS spectrograph also need to accommodate fast input beam (F/4) with fast camera optics (F/1.5), SALT RSS becomes the excellent starting point for designing DOTIFS spectrograph optics. Table 1 of Chung et al. (2018a) shows the difference between DOTIFS and SALT RSS parameters.

Fiber slit

In a fiber-fed spectrograph, fibers are located at the position of a slit in a conventional long-slit spectrograph and acting as a slit. This so-called fiber slit is composed of fibers with certain spacing in between (Figure B.7). Light coming out from fibers is dispersed in the spectral direction, which is perpendicular to the slit direction. Therefore, spectrum from each fiber forms multiple line-like images on the CCD. Ideally, an image of fiber at specific wavelength should be looked like a finite circle, because fiber cores have a circular shape. However, the actual fiber images are bigger and fuzzier than the theoretical size due to aberration. It brings a phenomenon called fiber cross-talk, which is overlapping of light from two adjacent fibers on the CCD. Thus, separation between fibers should be wide enough to minimize this cross-talk. At the same time, the separation should be narrow as much as possible to accommodate the maximum number of fibers in a single spectrograph, to reduce the number of total spectrographs. Therefore, proper spacing between fibers is necessary to be investigated. It is known that this separation should be at least 2-3 times bigger than Full Width-Half Maximum (FWHM) of fiber image profile (Sharp & Birchall 2010). In DOTIFS spectrograph, fiber image size is corresponding to 2.5 pixels on CCD so the spacing should be between 5 to 7.5 pixels. We applied such spacing as 6.75 pixels, which is 270 μm separation at the fiber silt (Figure B.7, left) so fibers can be properly separated within $\sim$2000 pixels in the spatial direction of the CCD. This corresponds to 288 fibers per one spectrograph.

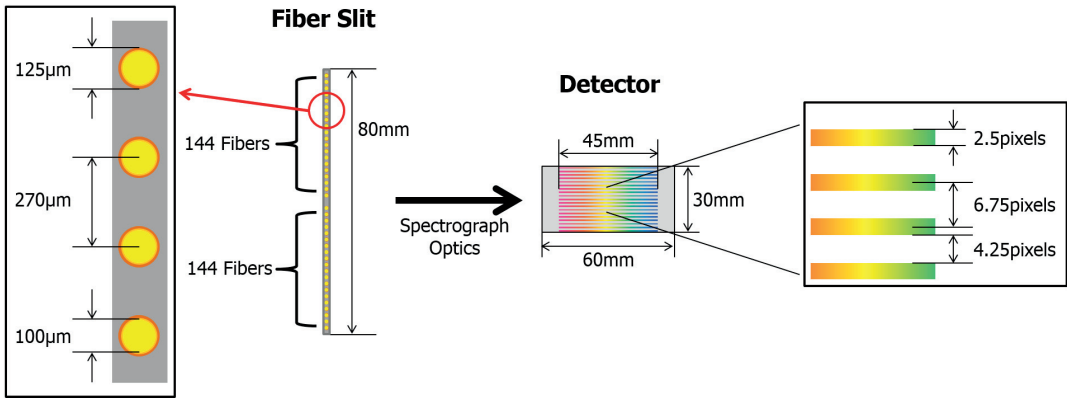

Figure B.7. Conceptual diagram of fiber slit and detector. One fiber slit contains light from two IFUs. The arrangement of the fibers is shown at the enlarged diagram on the left. Light from each fiber is dispersed by spectrograph optics and forms spectrum on the CCD, as shown in the right side diagram. Each spectrum is separated by 6.75 pixels.

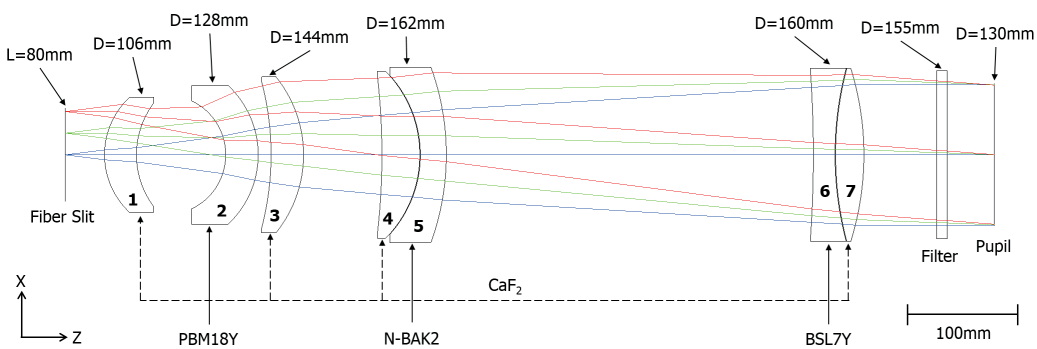

Figure B.8. Collimator optics layout. Diameter and glass material of each component is shown. Different color lines represent light from different field points. Path of the light is shown for only three field points for clarification.

Collimator

We design DOTIFS collimator to refract F/4 light from 80 mm fiber slit into collimated 130 mm diameter beam in the entire working wavelength range. The requirement for near-UV wavelength range (370 nm-400 nm) makes this design challenge since only a few available glass materials have high transmission (better than 99.5 %/10 mm) in this range. We take elements from the SALT RSS collimator, (F/4.2, 120 mm entrance slit, 150 mm diameter pupil, focal length=630 mm, 9 elements in 5 groups) as starting design and re-optimize to the DOTIFS requirements. Based on the measurement of the intensity distribution profile obtained from light coming out from actual optical fiber, we choose object property as NA=0.125 Gaussian profile beam with apodization factor of 3 for the collimator. A perfect 195 mm focal length paraxial lens is used during collimator optimization process. We set merit function as a sum of Root-Mean-Square (RMS) spot radius of 5 different wavelengths and 9 different field points. Also, the effective focal length is constrained to be 520 mm, and the incident angle of marginal rays at the pupil position is tried to be parallel as much as possible. The design (Figure B.8) starts with 3 singlets and followed by 2 pairs of closely separated singlets (7 elements in total.). We initially designed the close pairs as doublets, but later we decide to separate them to avoid possible risk during fabrication and delivery of optics. Compare to the starting design, the size and number of the lens had been decreased since our field and pupil diameter are smaller than the original. We use only spherical lenses to save fabrication cost as well as minimize alignment difficulty. Also, it has 2 pairs of closely separated singlets instead of 2 doublets + 1 triplet configuration in the starting design. Lens diameter is ranging from 106 mm to 162 mm.

Broadband Filter

We introduce the broadband filter to filter lights out of working wavelength range, to prevent second order contamination by wavelength shorter than 370nm and reduce stray light. Thus, we design the filter as a bandpass filter for the wavelength range from 370 nm to 740 nm. The filter is located next to the pupil and the dispersion

element, so the light out of working wavelength cannot propagate beyond. Also, we tilt the filter with respect to the slit direction (X-axis in Figure B.8) by 10 degrees. This tilting is shown in Figure B.9 but not in Figure B.8, since Figure B.9 is rotated by 90 degrees with respect to the optical axis compared to Figure B.8. We tilt the filter to remove light reflected from the camera optics side. Without filter tilting, the light can be reflected again by the filter and produce stray light on CCD. Considering the path of light reflected by the different angle of the tilted filter, wavelength dependent efficiency of the grating, and maximum incident angle of the collimated beam to the filter, we determine the tilted angle as 10° to effectively minimize the stray light.

Pupil and Dispersion Element

Dispersion element is a heart of spectrograph which disperses lights of a different wavelength in different directions. It is located is 30 mm after the pupil location to minimize the incident of scattered light coming from the collimator side. Since DOTIFS working wavelength range and spectral resolution do not require exchangeable grating or dichroic, we adopt a single and fixed dispersion element in the design. At the beginning of design phase, both conventional ruled grating and VPH grating had been investigated as a dispersion element. The ruled grating has an advantage on relatively wide bandwidth and flat efficiency curve, but it was turned out to be expensive and took long lead time for production. On the other hand, VPH grating has relatively higher throughput and can be designed with smaller optics since it is transmitted element (Barden et al. 1998). Also, it is cheaper than ruled grating and can be manufactured within few months (Barden et al. 2000). Based on the result of expected throughput comparison between both types of gratings, we choose VPH grating as a dispersion element of DOTIFS spectrograph. Grating properties are determined by various parameters; dispersion, pupil diameter, camera F-ratio and diffraction angle. For grating spectrograph configured at Littrow condition, wavelength dispersion on focal plane at the first order is given by

$$\lambda = 2 \times \sin \theta_{\mathrm{Littrow}} / \mathrm{L} \tag{B.1}$$

$$\text{dispersion}(\text{nm}/\mu\text{m}) = \text{d}\lambda/\text{dw} = \cos\theta_{\text{Littrow}}/\text{L}/\text{f}_{\text{camera}} \tag{B.2}$$

where θ_{Littrow} is an angle of the Littrow condition, w is length in the spectral direction, L is line density of a grating, and f_{camera} is focal length of a camera optics. Since dispersion value is set as 0.00822 (nm/μm) from spectral resolution requirement, other parameters should be determined appropriately to yield the dispersion. We consider a few things while determining those parameters. First, choice of angle of incidence should be similar to the Littrow wavelength, which is a wavelength with the highest efficiency over entire wavelength coverage. Also, a high angle of incidence to the grating increases the dispersion as well as the size of the grating. Second, the focal length of camera depends only on pupil diameter because F-ratio is already fixed as F/1.5. In practice, design optics with larger pupil size is easier than smaller since larger pupil size leads longer focal length for both collimator and the camera with given F-number. However, larger pupil also makes optics bigger so that it increases weight and fabrication cost. Third, lines per mm in VPH grating should be as low as possible to achieve broad bandwidth on response curve since our wavelength coverage is relatively wide for VPH grating (Baldry et al. 2004). At the same time, it is also required to be dense enough for manufacturability. This gives about 600 lines/mm as a minimum grating line density. By considering above characteristics of parameters, we decided the final parameters of the grating and size of the pupil. We use Rigorous Coupled-Wave Analysis (RCWA) simulation software, GSolver[1] (Version 5.2) to explore optimal grating parameters which yield reasonable optics size and high grating efficiency. The final parameter is determined as in the Table 2 of Chung et al. (2018a). We choose Littrow wavelength as 480 nm instead of the central wavelength (555 nm). This is due to known phenomena called Littrow ghost (Burgh et al. 2007), which is appeared as a bright spot on the image plane at the location of Littrow wavelength. Since there are many known galaxy emission/absorption lines just before 555 nm, there is a chance that one of those emission lines from redshifted galaxy can be overlapped with the ghost and cause a problem, if we do not remove it. Although there is some known way to

[1] `http://www.gsolver.com`

remove this ghost (Burgh et al. 2007), the methods are not easily applicable in case of DOTIFS spectrograph. Therefore, we decided to shift the ghost wavelength to mitigate the problem rather than removing it. By shifting Littrow wavelength to 480 nm, which is shorter than known emission/absorption lines, we can minimize the overlapping of the ghost with those known lines. In this case, lines longer than 480 nm will never be suffered by the ghost, and lines shorter than 480 nm is located quite far from there, (e.g., OIII: 436.32 nm, H-gamma: 434.1 nm) thus they will also not be contaminated by nearby galaxies with redshift less than z=0.1, which are primary target of DOTIFS.

Camera

DOTIFS camera optics is designed to focus the dispersed light on the CCD. The camera is articulated about the grating axis to choose the wavelength range to focus. We choose the angle between grating axis and camera axis as 11.17 degrees so that the central wavelength light will pass through the optical axis of the camera. The F-ratio of the camera is determined as F/1.5 (focal length = 195 mm) by the collimator F-number, fiber core size, pixel size and the spectral resolution requirement. This fast F-ratio makes this design challenging and sensitive to tolerances. Optics size should be large enough to accommodate whole light coming from the dispersion element within working wavelength range without any vignetting.

Again, starting design takes elements from the SALT RSS camera (F/2.2, 95 × 61 mm focal plane, focal length=330 mm, 9 elements in 4 groups), and re-optimized to fulfill the DOTIFS requirements. For initial optimization, a perfect paraxial lens (focal length = 520 mm) is used as an artificial collimator. After the initial optimization, the paraxial lens is replaced with the actual collimator optics design which is designed as in the Ch. 3.2. The merit function minimized the RMS spot radius in the same way as of the collimator. An effective focal length is constrained to be 195 mm.

The design (Figure B.9) starts with 3 pairs of closely separated singlets and followed by 3 singlets (9 elements in total.) Compare to the starting design, size of lens elements are decreased, but some elements remain identical although the size of the focal plane

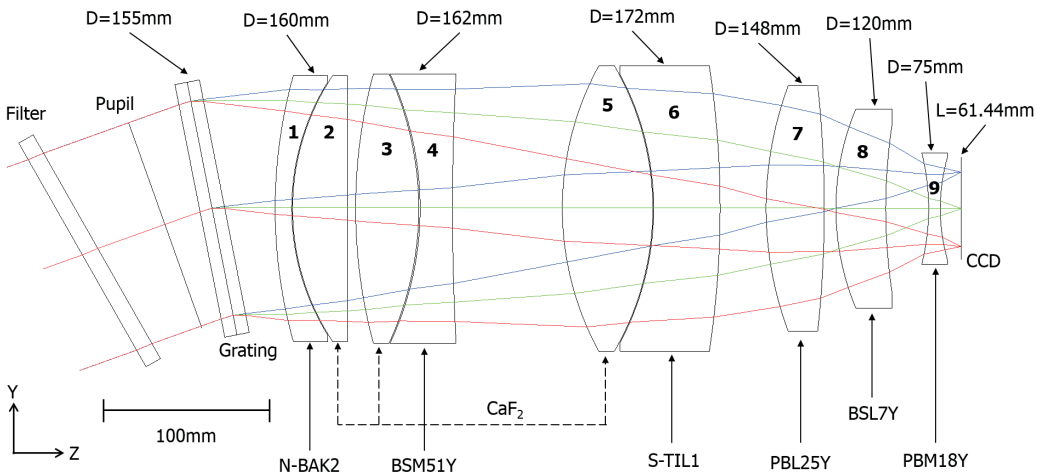

Figure B.9. Camera optics layout. Descriptions are identical as in Figure B.8. In this figure, the color of light represents difference wavelength. Blue is 370 nm, and red is 740 nm light. A tilted filter with respect to the optical axis is shown in this figure.

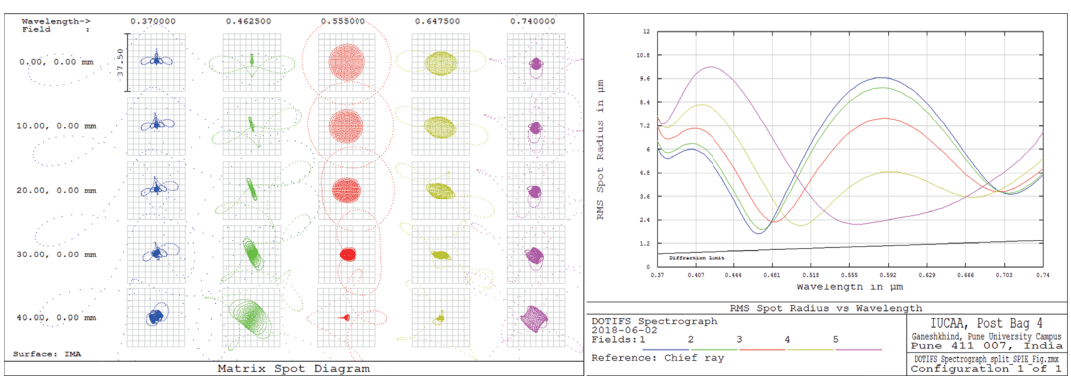

Figure B.10. (Left) Matrix spot diagram of the spectrograph optics. Color represents different wavelength. (Right) Wavelength versus RMS spot radius plot. Color represents the light of different field points, as in the left figure from top to bottom rows.

is smaller than the original. This is because the starting design has an aspheric surface, but our design has only spherical surfaces. Also, F-ratio of our design is faster than the original. Thus it demands more surfaces to achieve desired performance. Field of view of the camera is about 13.5°.

In Figure B.10, we present spot diagram and wavelength versus RMS spot radius graph of the spectrograph optics. The box size of the spot diagram is 37.5 μm which correspond to 2.5 pixels on CCD. Although the diagram shows quite a large spot shape at their out-most region, most of the lights are concentrated at the center. Therefore it has very small RMS spot radius as appeared in the wavelength versus RMS spot radius graph. The camera will be controlled by the IUCAA digital sampling array controller, using a digital correlated double sampling technique which can reduce a thermal noise (Chattopadhyay et al. 2018b).

Detector

The detector size is chosen based on spectral resolution requirement, CCD availability, and the capability of the optics. The size in spectral direction is set as 3,000 pixels to accommodate the whole wavelength coverage with required spectral resolution (See section B.2.3). Since there is no available CCD with 3K in one direction from major CCD manufacturers, we have to choose 4K in spectral direction and remains 1K as unused. The size in the spatial direction is determined to minimize expected cost with reasonable complexity. It gives us two options on the size of the spatial direction, 2K pixels or 4K pixels. 4K by 4K CCD requires bigger and more optical elements, but it can reduce the number of the spectrograph. On the other hand, 2K by 4K requires smaller optics, but double the number of the spectrograph to accommodate the same number of total fiber compare to 4K by 4K CCD option. After estimation of fabrication cost and weight budget of both options, 2K by 4K CCD option with 8 spectrographs is turned out to be the more economical solution. The final decision on CCD model is e2v CCD44-82 chip (2048×4096, 15 μm size pixels).

We adopt new coating technique on CCD to increase throughput. DOTIFS spec-

trograph has fixed wavelength distribution on the CCD since the spectrograph is in a single configuration with fixed dispersion element and working wavelength range. We take this as an advantage to maximize the throughput. Unlike the traditional broadband coating, we applied wavelength dependent coating called graded coating along the spectral direction, so coating on each pixel will be optimized for the wavelength of light which will fall on the pixel. Wavelength map of our coating scheme is shown in the Figure 5 of (Chung et al. 2018a). This graded coating improves CCD quantum efficiency by several percentage points, especially in the blue and near UV region.

We present throughput of the spectrograph optics in Figure B.11. Throughputs of the individual sub-component are plotted with different colors. Due to high-throughput optical glasses, throughput loss from collimator and camera optics are mainly attributed from AR coating, not from glass except near-UV range. Throughput curve of CCD response is from the theoretical expectation of CCD quantum efficiency with the graded coating. Similarly, the curve of VPH grating is also from the theoretical simulation, fitted to the several measured values. The curve of the broadband filter is again from the theoretical simulation. Thus, the actual curves of CCD, VPH grating and filter could be different from what shown here. The black line shows combined throughput of spectrograph optics. It is 53.9% at peak wavelength and 41.8% on average, which satisfies the design goal of the optics ($> 35\%$). We also show throughput of the entire DOTIFS instrument which includes fore-optics, IFU, fibers, and spectrograph, but without sky transmission. Average throughput of the instrument is 26.0%.

Tolerance and Thermal Analysis

We performed tolerance analysis with Zemax optical design software. This is to find out required fabrication and alignment tolerance of DOTIFS spectrograph optics. Requirements for lens fabrication and alignment accuracy are derived and stated in the Table 3 and Table 4 of Chung et al. (2018a). We did sensitivity and Monte-Carlo analysis with those requirements as well. Results show that we can achieve the tolerance requirements by modern fabrication and alignment technology. Since DOTIFS spectrograph

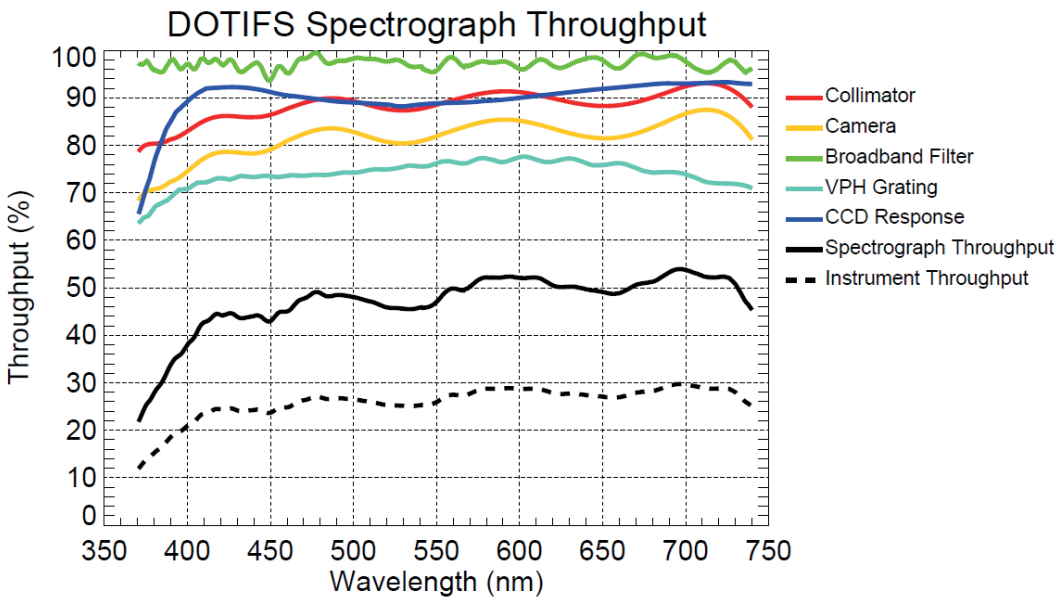

Figure B.11. (Left) Matrix spot diagram of the spectrograph optics. Color represents different wavelength. (Right) Wavelength versus RMS spot radius plot. Color represents the light of different field points, as in the left figure from top to bottom rows.

uses the distance between the last and the second last element of the camera optics as a compensator, we use the same for this analysis.

We present the result of sensitivity analysis in the Table 5 of Chung et al. (2018a). The change of average RMS spot radius is 5.64 μm. In general, camera optics is more sensitive than the collimator due to its fast F-ratio. Major worst offenders in fabrication requirements are the surface tilt of close pair singlets in camera optics. The performance is also sensitive to refraction index and Abbe number of several camera elements. It shows similar trends in the sensitivity analysis of alignment requirements. Element tilt of close pair singlets in camera is the most sensitive offender among alignment tolerances.

We ran 100,000 Monte-Carlo simulations, assuming normal distribution statistics with requirements above. Results are stated in the Table 6 of Chung et al. (2018a). The statistics show that mean RMS spot radius as 11.1 μm, with a standard deviation of 3.1 μm. This difference is considered to be acceptable. Additional analysis on designs

generated by Monte-Carlo simulation also confirms that the result is satisfying optics performance requirements.

We also performed thermal analysis to estimate the impact of temperature variance on optics and compensate performance degradation derived from the variance. Since the spectrograph optics will be thermally equivalent with the surrounding environment, the effect of the temperature variance should be clarified. The spectrograph optics is designed and optimized for the temperature of 20°C. Air temperature at the observing site is known as varying between -5 to +22°C yearly while the intra-night temperature variation is less than 2°C (Sagar et al. 2012). Although thermal effect within a single night is expected to be negligible, the variance over entire year should be considered because of its wide temperature variation range and CaF_2 elements which has a large value of temperature dependent index of refraction variance and thermal expansion coefficient. In general, performance degradation due to temperature variance can be easily compensated by changing the distance between two elements in the optics. As in the tolerance analysis, we use the distance between the last and the second last element of the camera optics as a compensator.

We again ran thermal analysis with Zemax optical design software. In Zemax, size, thickness, and index of refraction of optics are changed by temperature variation. We use thermal index variation and expansion coefficient data of each glass from catalogs supplied by glass manufacturers. The thermal coefficient of Aluminum 6061-T6, $(23.5 \times 10^{-6}/°\mathrm{C})$ is used for expansion of opto-mechanical structure in between. We consider only expansion along the optical axis in this analysis. We performed thermal analysis in two conditions. First, we tested the effect of temperature change among annual temperature variation range at the telescope site. This analysis had been done with temperature range from -5 to +25°C with 5°C increments. At each temperature, first we measure RMS spot radius without any compensation. Then we tried to re-optimize optics to minimize RMS spot radius using compensator and record corrected RMS spot radius as well as the displacement of the compensator.

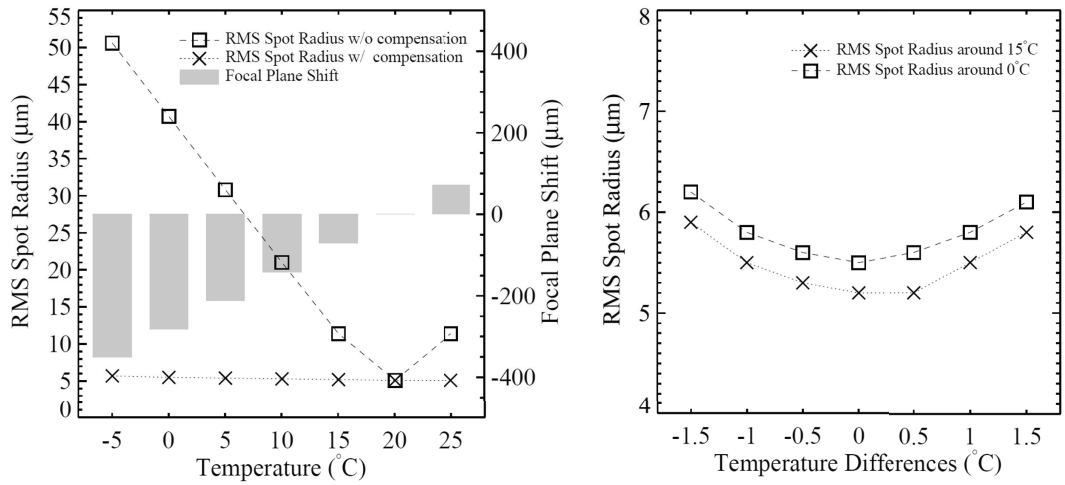

Figure B.12. (Left) Result of thermal analysis with and without compensation within a yearly temperature range of the telescope site. (Right) Similar result without compensation within the intra-night temperature range.

The result shows that the temperature variation significantly changes the RMS spot radius. It also shows that a compensator with a reasonable displacement can successfully correct such change (Figure B.12, Left). Second, we investigated the impact of temperature variance within intra-night variance range. We select two nominal temperatures. (0 and 15°C) At each temperature, we first re-optimize optics using compensator, and measure its RMS spot radius changes over +/-1.5°C with 0.5°C increments without any additional compensation. This procedure assumes an actual observing condition, which will do optics compensation only at the beginning of each night. Result shows that RMS spot radius variation over intra-night temperature variance at both nominal temperature is very small. (Figure B.12, Right) Thus, once the optics is compensated at the beginning of each night, there will be no significant performance degradation during rest of the night. Compensator mechanics is introduced in the opto-mechanical structure by putting camera dewar on the high precision linear stage. Image quality optimization algorithm will be developed and included in the instrument control software so that this procedure can be done automatically. The algorithm some continuum images at different stage location, then find out optimal displacement which has minimum

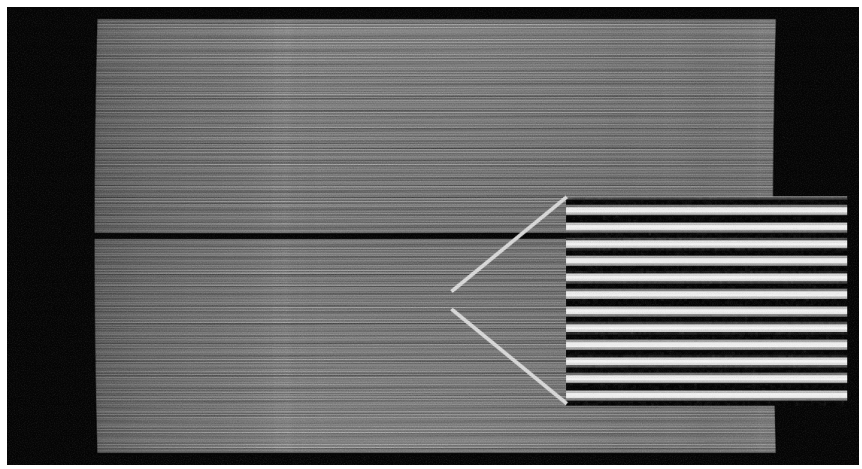

Figure B.13. Simulated DOTIFS calibration image with Xenon arc lamp.

line width along the spatial direction.

B.3 Software

DOTIFS software have several sub categories: 1) Instrument control, 2) User interface, 3) Data reduction pipeline, 4) Auxiliary program. Instrument control system is a back-end of the DOTIFS software, includes controllers for the electronics, such as CCD, actuator, lamp, sensors, and deployment algorithm. User interface is a front-end which enables engineers or observers to monitor the system and execute the observation command. Data reduction pipeline is a specific software which can process raw CCD image and generate science-ready data which astronomers can directly use for the research. Auxiliary program includes data simulator or signal to noise ratio calculator. Here we present the DOTIFS auxiliary programs developed by the author.

B.3.1 Data Simulator

Data reduction software for DOTIFS has been developed simultaneously with the instrument hardware design. We plan to use one of the publicly available general IFS data reduction tools (eg. P3D (Sandin et al. 2010), or R3D (Sánchez 2006)) as a starting point. and include some additional features like sky subtraction or treatment of

particular observing mode. Due to complex nature of the CCD image of fiber-fed spectrograph, it is desirable to have a simulated image therefore we can fine tune the pipeline parameters. The DOTIFS data simulator has been developed to provide such a simulated image. It performs a virtual observation and generates spectral data as would be recorded on the CCD by the real instrument. Various instrumental and other effects are involved in making the simulated data as close as possible to real data: e.g. atmosphere, sky background, transmission, spectrograph optical aberration, and detector noise. Initially, the simulator was developed in C programming language. It was converted to the IDL version later and designed to use an output of signal to noise ratio calculator as an input.

In Figure B.13 and Figure B.14, we present the simulated CCD iamge of fiber-flat and wavelength calibration. Enlarged view of the image is also given in the middle. Figure B.15 shows the subsection of an image observing an artificial object. More details of the simulator can be found in Chung et al. (2015).

B.3.2 S/N Calculator

We developed a S/N calculator to generate a input spectrum for the data simulator, as well as for the users to plan their observation in the future. The calculator simulates an expected S/N ratio of the spectrum from a given target (galaxy template, sky, or calibration sources). Command line version DOTIFS S/N calculator in `Python` is available through Github[2]. We show the example output from the calculator in Figure B.16.

[2] `https://github.com/astrohchung/dotifsetc`

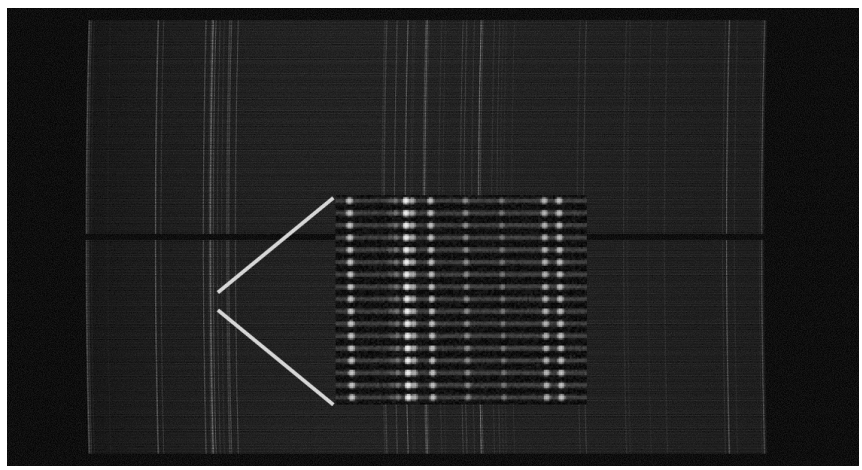

Figure B.14. Simulated DOTIFS calibration image with Krypton and Mercury-Neon lamp.

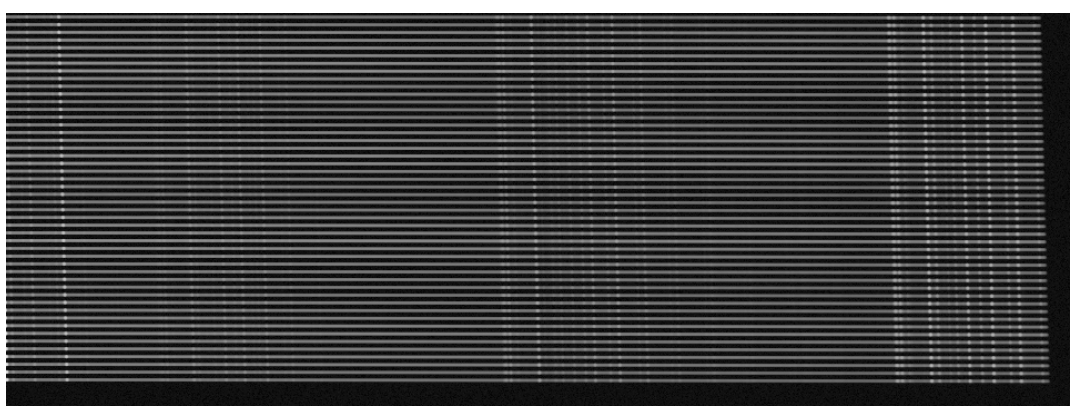

Figure B.15. Section of the simulated CCD image of the DOTIFS(artificial object). It shows lower right part of the CCD. Each horizontal line represents light from one spatial element (fiber). A low level of distortion can be also found in the image. Most of the emission lines in the image are bright sky lines.

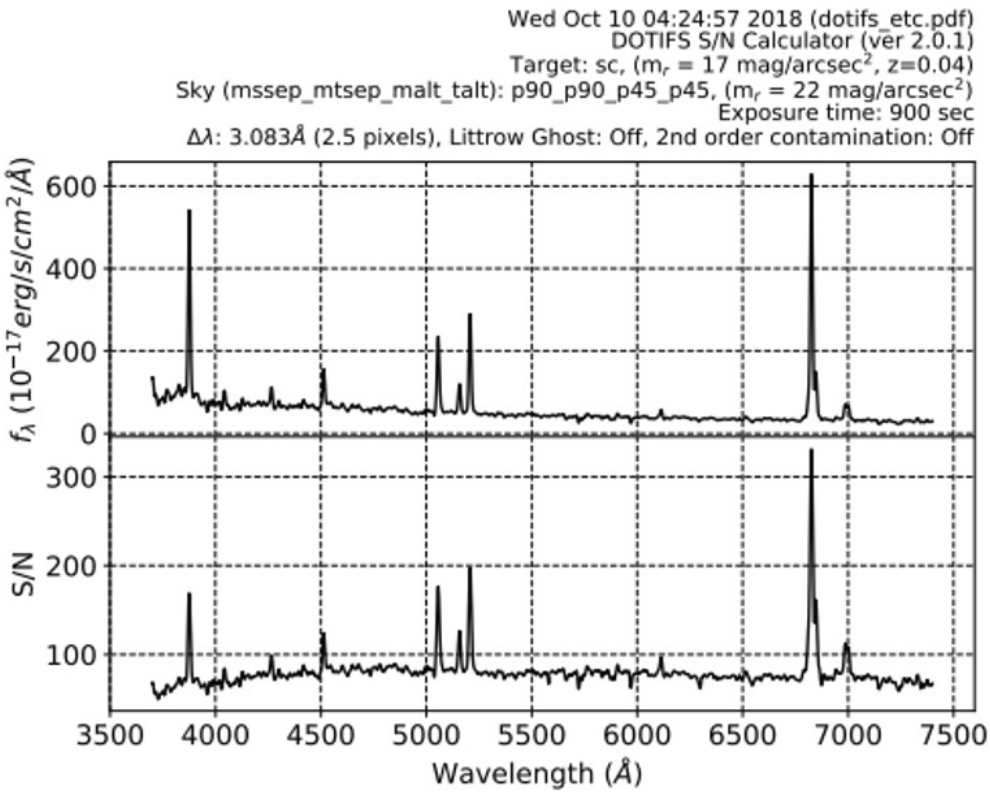

Figure B.16. Example of DOTIFS exposure time calculator output. It shows all the input parameters along with the input spectrum and the calculated signal to noise ratio distribution (Sc type galaxy template with surface brightness of $m_r = 17 mag/arcsec^2$, exposure time of 15 minutes, sky brightness, and wavelength bin size.)

Appendix C

Deconvolution Method Verification

C.1 Mock IFU Data Generation

In order to quantitatively examine the effect of the deconvolution, the mock IFU data should be generated correctly as per the model galaxy parameters. Here we describe the generation process of each type of mock IFU data (*Free*, *Conv*, *Deconv*) in detail. Initially, an ideal IFU data (*Free*, without any seeing effect) is produced for each set of galaxy model parameters. Then the PSF-convolved IFU data (*Conv*) is made by the convolution of a wavelength dependent PSF on the 2D image at each wavelength slice with addition of Gaussian random noise. *Deconv* IFU data is produced from *Conv* IFU data by applying the deconvolution method.

An arbitrary synthetic spectrum, composed by single-stellar populations with three different age (1 Gyr (15%), 5 Gyr (60%), 10 Gyr (25%)) from MILES stellar library (Sánchez-Blázquez et al. 2006; Falcón-Barroso et al. 2011; Vazdekis et al. 2010) is chosen as a rest-frame model spectrum (using unimodal initial mass function (Vazdekis et al. 1996) and Padova+00 isochrones (Girardi et al. 2000); $\Delta\lambda$ = 2.51 Å, λ range from 3,540 to 7,410Å)

For each set of a galaxy model parameters (subsection 2.3.2), we generate the *Free*

and *Conv* mock IFU data, according to the below steps.

1. The spatial and spectral sampling size is determined. Following the sampling size and the data structure of MaNGA IFU data, we choose spatial sampling size as 0.5 $''$, and spectral sampling as a logarithmical bin which follows $\lambda = 10^{3.5589+0.001\mathrm{x}}$, where x from 0 to 4562.

2. 2D maps of flux (Sersic profile), velocity (Equation 3.1), velocity dispersion (Equation 2.2), S/N are identified as per a set of galaxy model parameters. We assume that all three maps follow the identical geometry as defined by the inclination angle, position angle, x_{cent} and y_{cent}. In case of S/N map, a relative S/N map is generated as per the Sersic profile then scaled to have a S/N at 1 R_e as per the galaxy model parameter.

3. At each 2D pixel(Spaxel), a rest-frame synthetic spectrum is modified as per the respective line-of-sight velocity and the velocity dispersion value in the 2D map. First, the spectrum is convolved by a Gaussian function as per the velocity dispersion value. Second, it is redshifted by z of a model galaxy. Third, a spectrum at each spaxel is blue-shifted/red-shifted according to the corresponding line-of-sight velocity value.

4. (*Conv* IFU data only) A 2D Gaussian PSF is convolved to the 2D image slice at each wavelength bin. The size of the Gaussian PSF is determined according to the model FWHM coefficient parameters. For example, in case of $c_0 = 2.6''$ and $c_1 = -1.2 \times 10^{-5}''/$Å, $\mathrm{FWHM_{Conv}}$ at g-band effective wavelength (4770 Å) is $2.52''$, which is median $\mathrm{FWHM_{PSF}}$ at g-band of MaNGA galaxies (Figure 2.8).

5. A constant instrument spectral resolution (2.9Å) is applied at each spaxel. It is done by the convolution of Gaussian function with FWHM corresponds to the quadratic difference between the instrument spectral resolution and the intrinsic resolution of the model synthetic spectrum (2.51 Å).

6. At each spaxel, the noise spectrum is calculated. The relative S/N spectrum is

calculated from the flux spectrum, and it is scaled so that the S/N value of the median flux value would be the value from the S/N map. The noise spectrum is calculated by dividing the flux spectrum by the scaled S/N spectrum. The noise is not added to the flux spectrum at this stage.

7. Hexagonal shape mask is applied to the IFU data to resemble the MaNGA-like IFU data.

8. (*Conv* IFU data only) Gaussian random noise is applied to the IFU data using noise spectrum from the step 6. At each spaxel, the noise spectrum is multiplied by the Gaussian random value (-3 to 3) and added to the flux spectrum.

Although our mock IFU data is generated to mimic the MaNGA IFU data, it can be considered as IFU data of other IFS instrument by considering the scaled the model parameters. For example, $0.5''$ grid size, field of view = $32''$, $R_1 = 4''$, and $1/R_2 = 0.02$ $(1/'')$ can be considered as equivalent with the MUSE IFU data with 0.2 $''$ grid size, field of view = $12.8''$, $\mathrm{FWHM_{PSF}} = 1''$, $R_1 = 1.6''$, and $1/R_2 = 0.05$.

C.2 Deconvolution Effect Examples

In Figure 2.2, we presented the example of the effects of PSF convolution and deconvolution to the IFU data. Here we show more examples from our mock IFU data to illustrate the effects of the deconvolution in various mock galaxy parameter space. Examples are taken from Group 1 mock IFU data. Figure C.1 and Figure C.2 show the result of the deconvolution at low S/N (Median $\mathrm{S/N_{pPXF}}@1R_e = 10$) when n_{Sersic}=1 and 4, R_1=$3''$, i=55°. Figure C.3, Figure C.4, Figure C.5, and Figure C.6 show the result of the deconvolution at different combinations of i (55, 70°) and n_{Sersic} (1,4), when $\mathrm{S/N_{pPXF}}@1R_e = 20$ and R_1=$3''$. The forth columns of the all figures represent the significant difference between the maps from *Free* and *Conv*. The effect of PSF convolution is crucial in the distribution of Flux, velocity and the velocity dispersion. The fifth columns of the all figures show that the mismatch induced by the PSF convolution

are significantly restored. However, the restoration is not very effective at the outer radius where S/N becomes low, and the flux distribution shows non-negligible artifacts around the center of galaxies, particularly when n_{Sersic}=4. Nevertheless, the velocity and the velocity dispersion are generally well recovered even when the n_{Sersic}=4.

C.3 Dependence on Deconvolution Parameters

C.3.1 Number of Deconvolution Iteration

In section 2.3.4, we described the relationship between N_{iter} and the restored model kinematic parameters (Figure 2.6). Here we give similar plots with model galaxies of different parameters to provide more insight into the determination of N_{iter} to the readers. Figure C.7, Figure C.8, Figure C.9, Figure C.10 are complementary figures to the Figure 2.4. The figures show the relation between the fitted RC model parameter to the N_{iter} for different R_1 (2, 3, 4 ($''$)) and $1/R_2$ (-0.05, 0, 0.05 ($1/''$)). The result is consistent with Figure 2.4 thus the N_{iter}=20 is an adequate choice for the deconvolution.

C.3.2 Size of PSF FWHM

Here we show the relation between $\mathrm{FWHM_{DECONV}}$ and the restored model kinematic parameters. We present plots similar to the Figure 2.8 but with different model galaxies as well as different $\mathrm{FWHM_{CONV}}$.

Figure C.11, Figure C.12, Figure C.13, and Figure C.14 are complementary figures to the Figure 2.5. The figures show the relation between the fitted RC model parameter to the $\mathrm{FWHM_{Deconv}}$ with different R_1 (2, 3, 4 ($''$)) and $1/R_2$ (-0.05, 0, 0.05 ($1/''$)). The result is consistent with Figure 2.5 thus the result of the deconvolution is consistent when $|\mathrm{FWHM_{Deconv}} - \mathrm{FWHM_{Conv}}|$ is smaller then the $\mathrm{FWHM_{PSF}}$ measurement error ($0.2''$).

Figure C.15 and Figure C.16 show the result of the deconvolution with different $\mathrm{FWHM_{Conv}}$ (2.3, 2.9 ($''$)). Again, the result of the deconvolution is consistent when $|\mathrm{FWHM_{Deconv}} - \mathrm{FWHM_{Conv}}|$ is small.

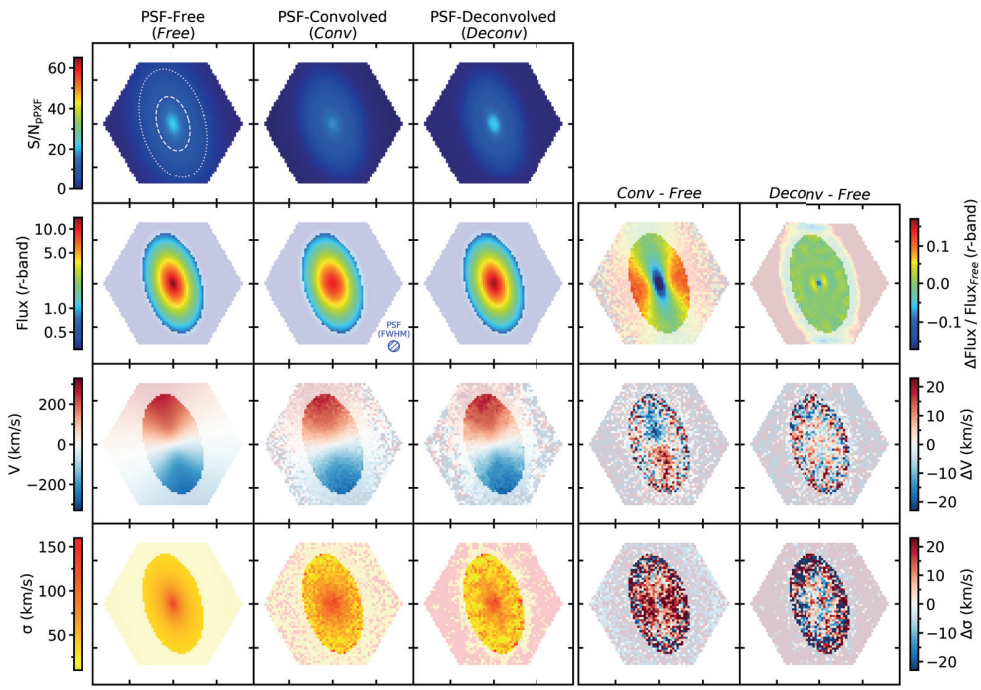

Figure C.1. n_{Sersic}=1, $R_1 = 3''$, $1/R_2 = 0.05/''$, $i = 55°$, and $\mathrm{S/N_{pPXF}}@1R_e = 10$

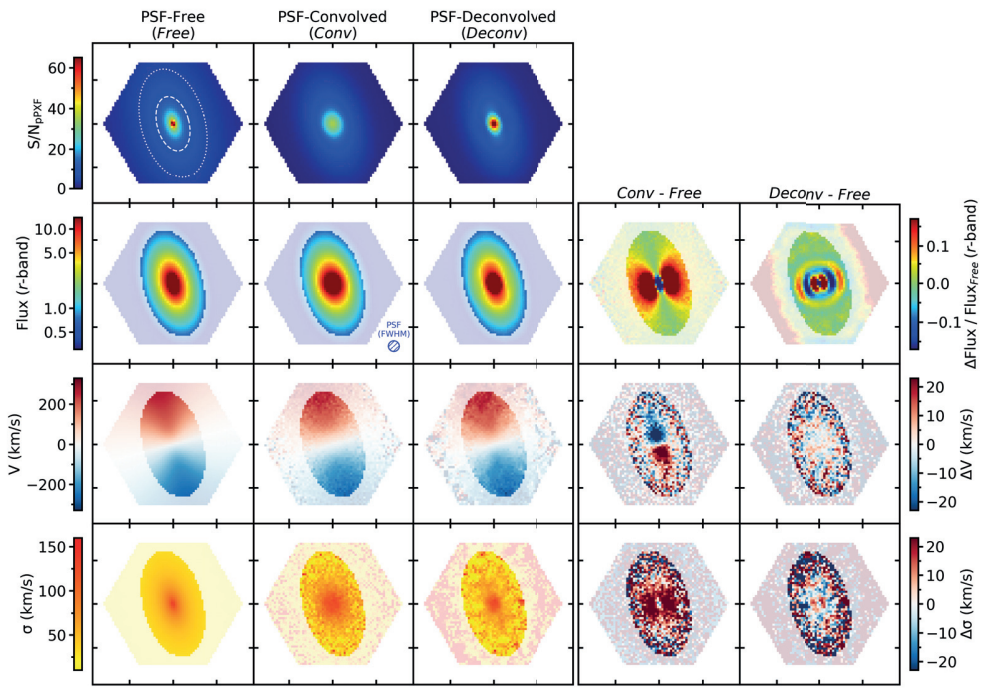

Figure C.2. n_{Sersic}=4, $R_1 = 3''$, $1/R_2 = 0.05/''$, $i = 55°$, and $\mathrm{S/N_{pPXF}}@1R_e = 10$

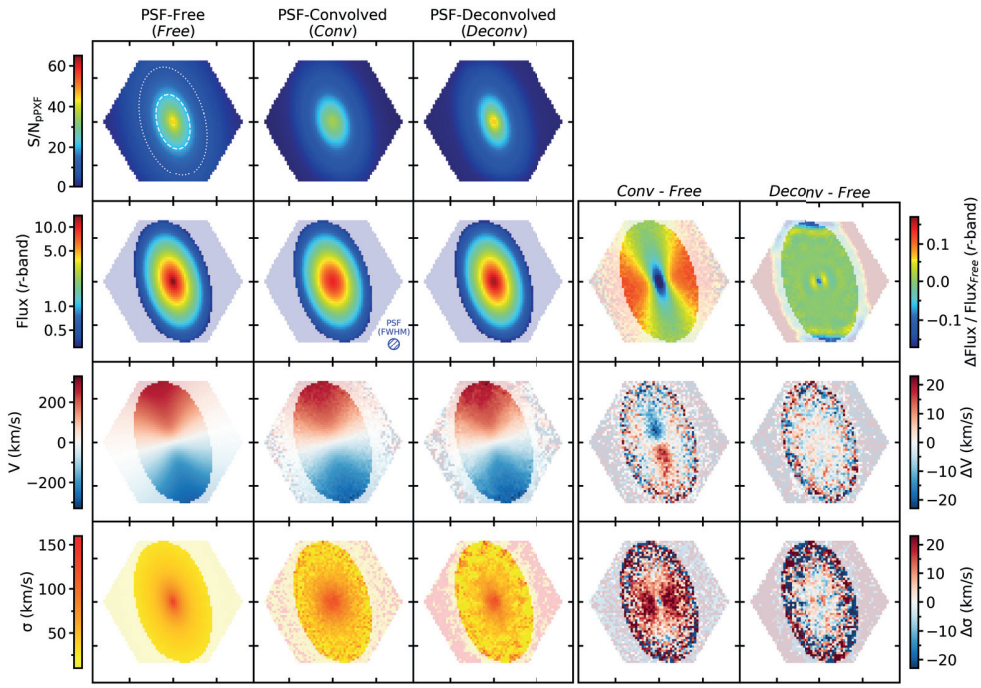

Figure C.3. n_{Sersic}=1, $R_1 = 3''$, $1/R_2 = 0.05/''$, $i = 55°$, and $\mathrm{S/N_{pPXF}}@1R_e = 20$

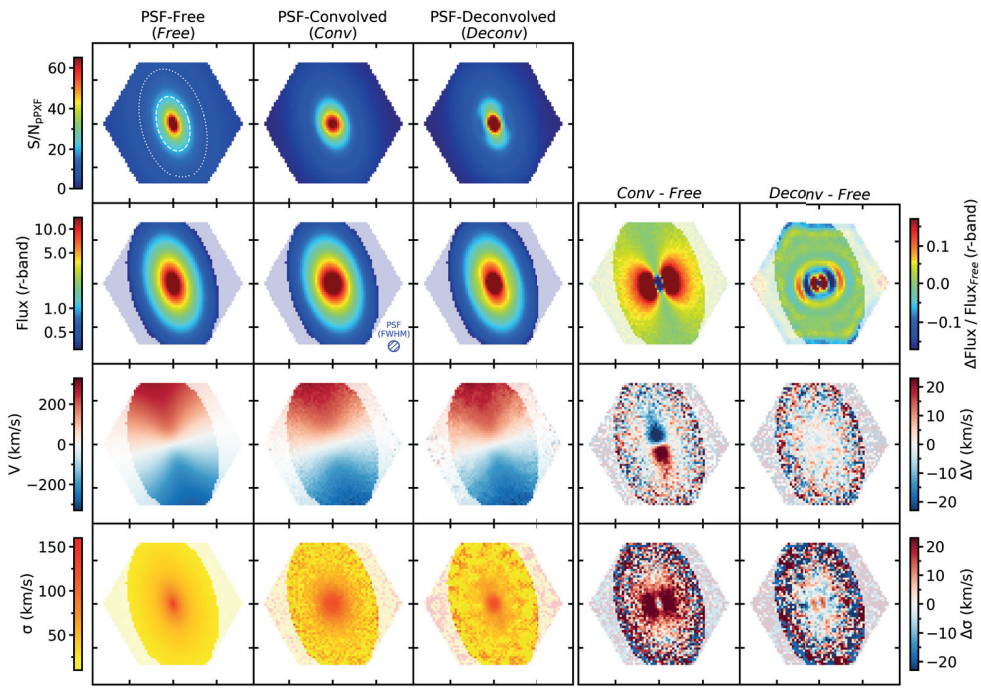

Figure C.4. n_{Sersic}=4, $R_1 = 3''$, $1/R_2 = 0.05/''$, $i = 55°$, and $\mathrm{S/N_{pPXF}}@1R_e = 20$

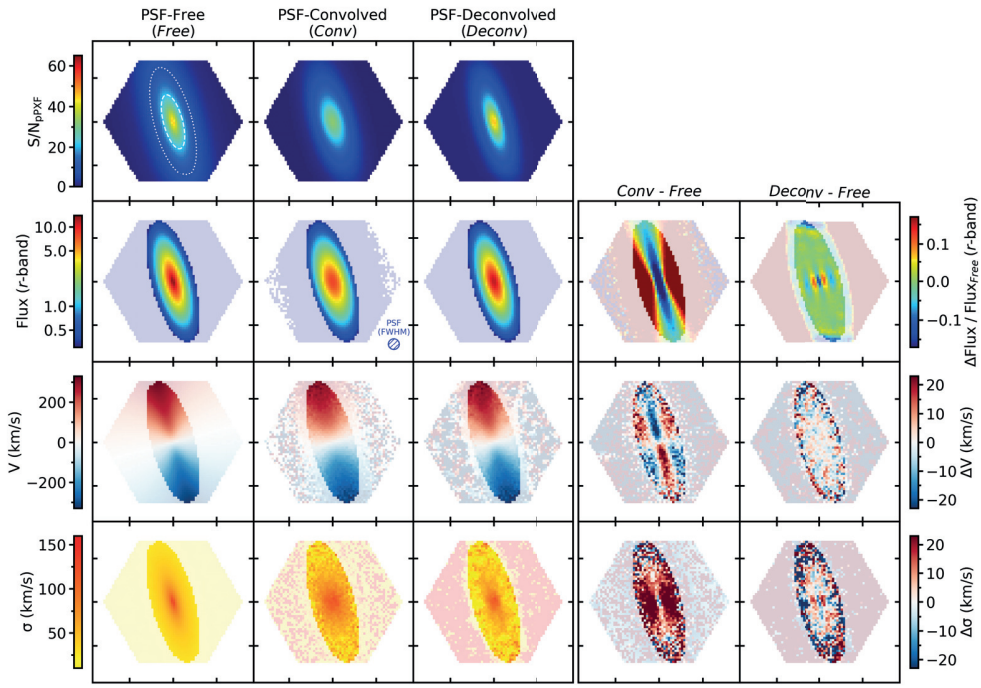

Figure C.5. n_{Sersic}=1, $R_1 = 3''$, $1/R_2 = 0.05/''$, $i = 70°$, and $\mathrm{S/N_{pPXF}}@1R_e = 20$

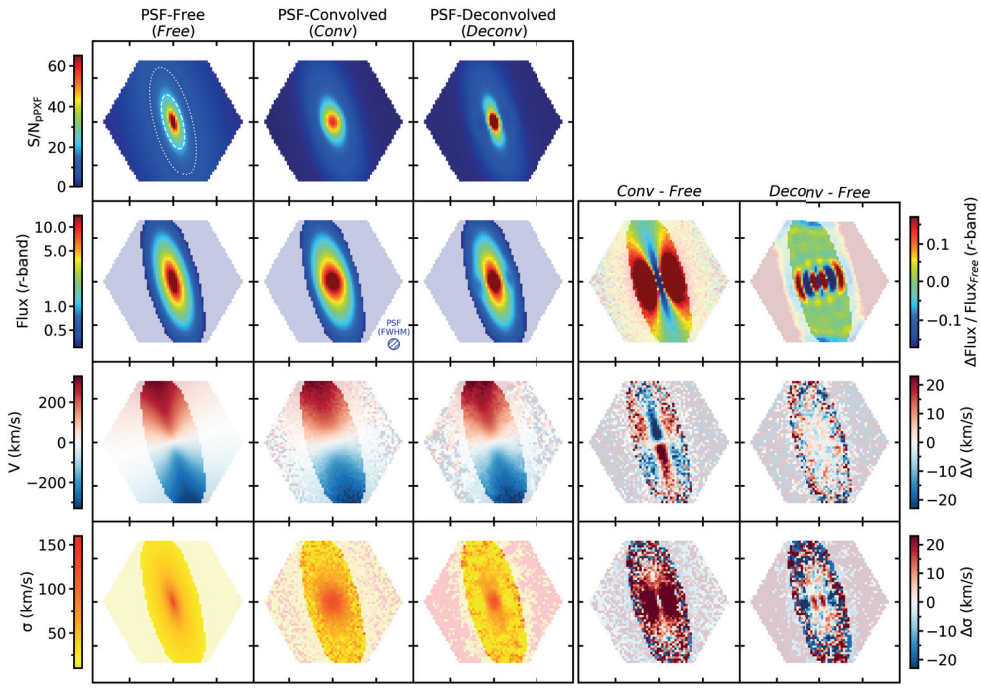

Figure C.6. n_{Sersic}=4, $R_1 = 3''$, $1/R_2 = 0.05/''$, $i = 70°$, and $\mathrm{S/N_{pPXF}}@1R_e = 20$

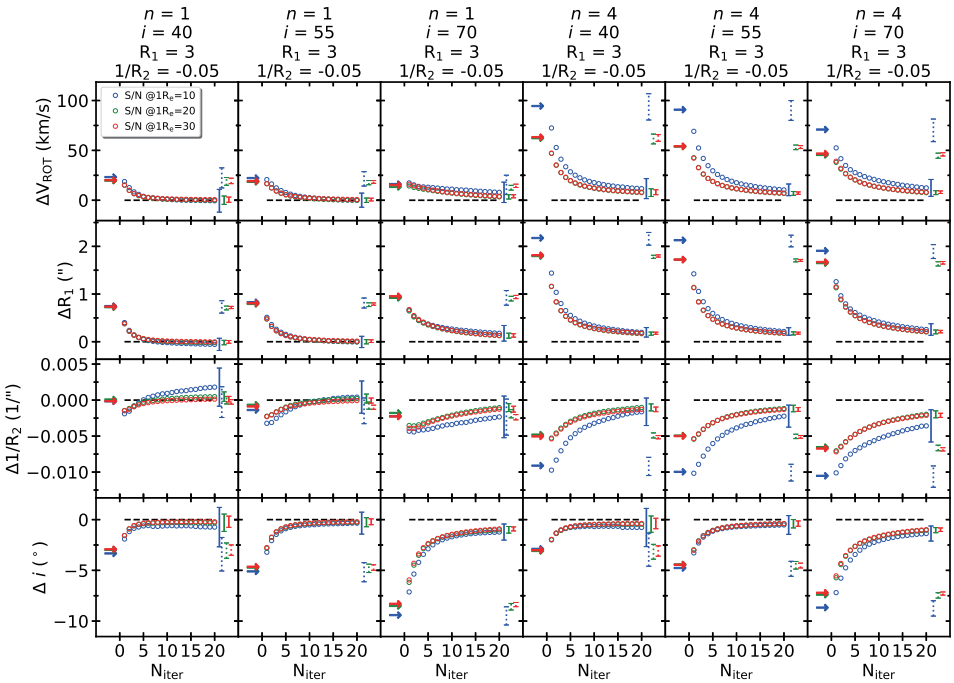

Figure C.7. $R_1 = 3, 1/R_2 = -0.05$

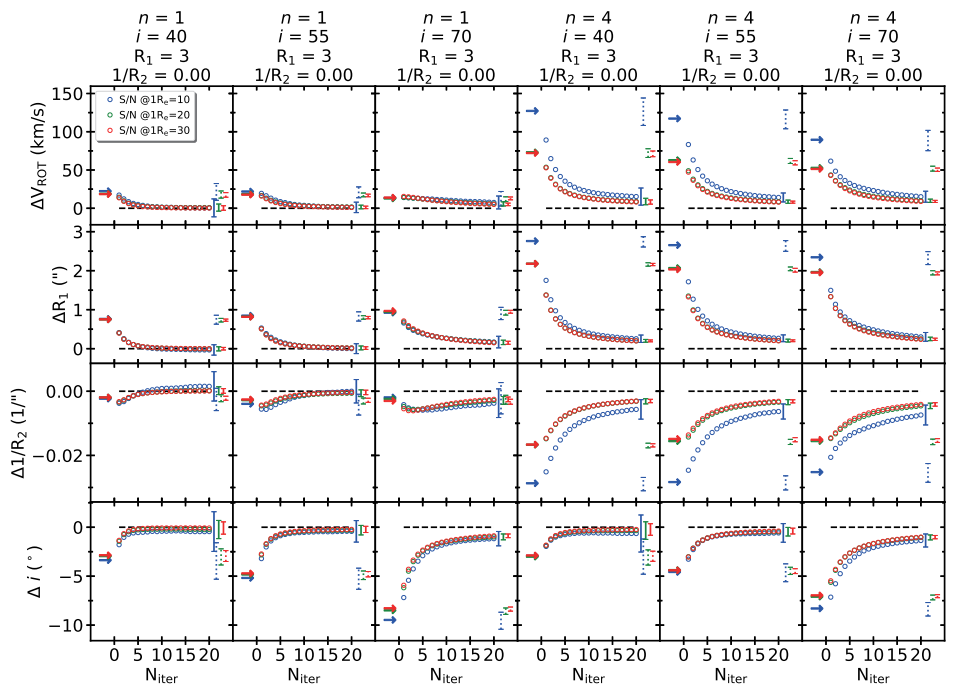

Figure C.8. $R_1 = 3, 1/R_2 = 0$

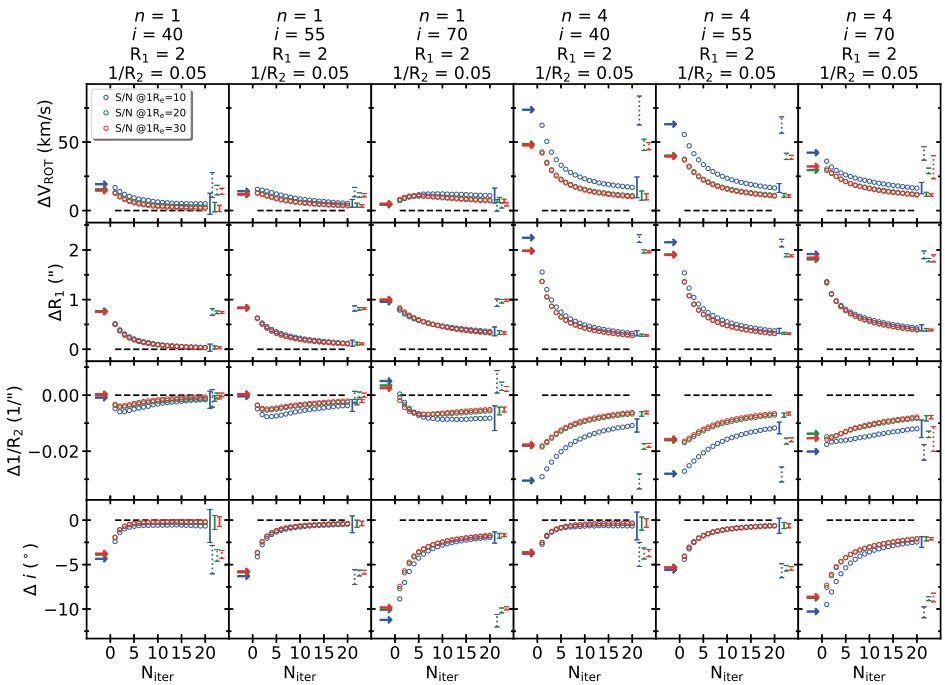

Figure C.9. $R_1 = 2, 1/R_2 = 0.05$

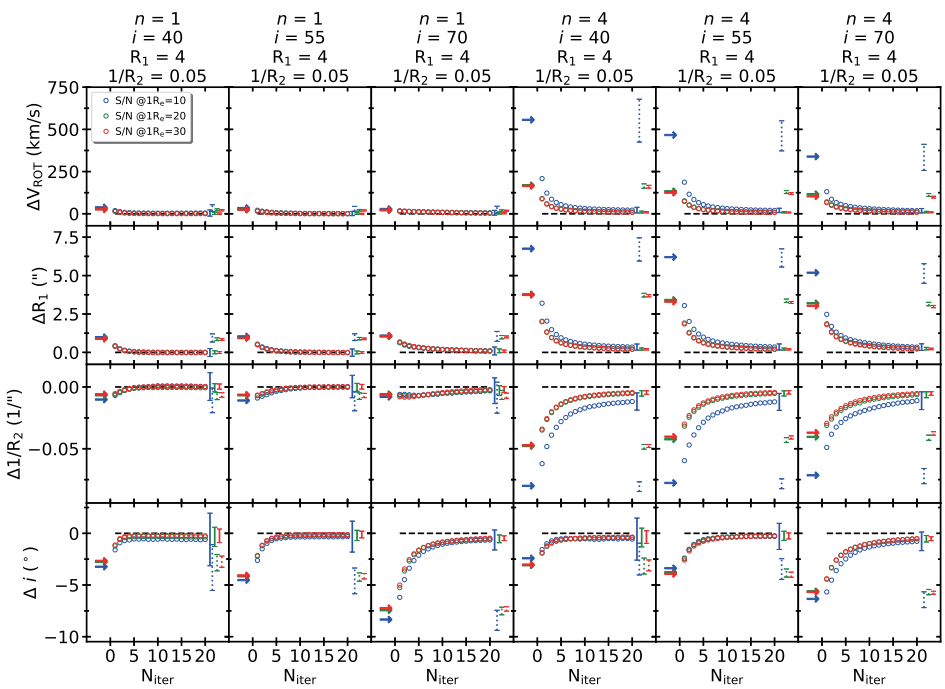

Figure C.10. $R_1 = 4, 1/R_2 = 0.05$

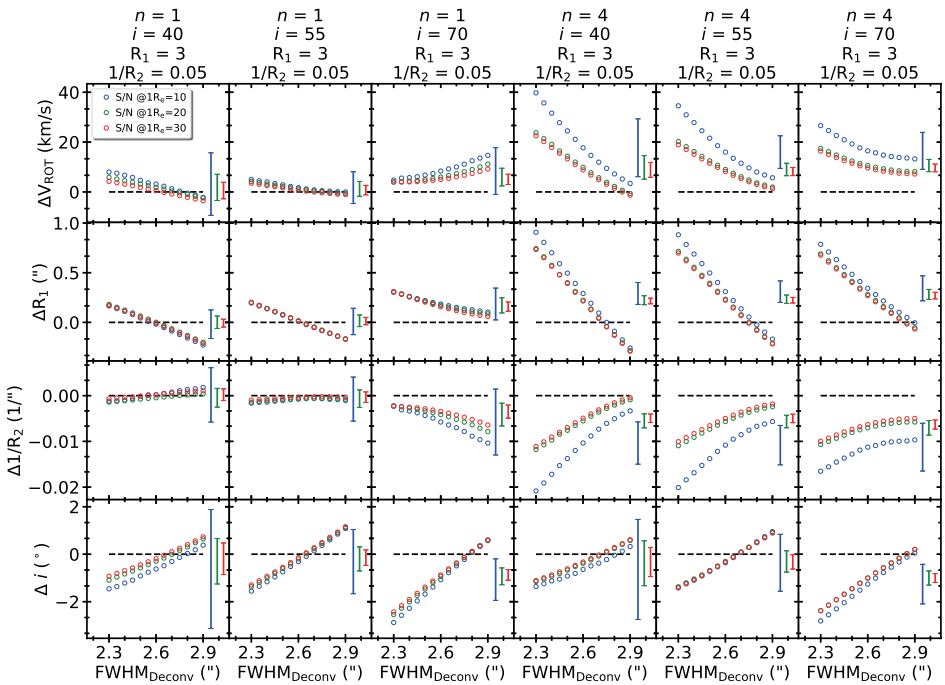

Figure C.11. $R_1 = 3, 1/R_2 = -0.05, FWHMc_0 = 2.6$

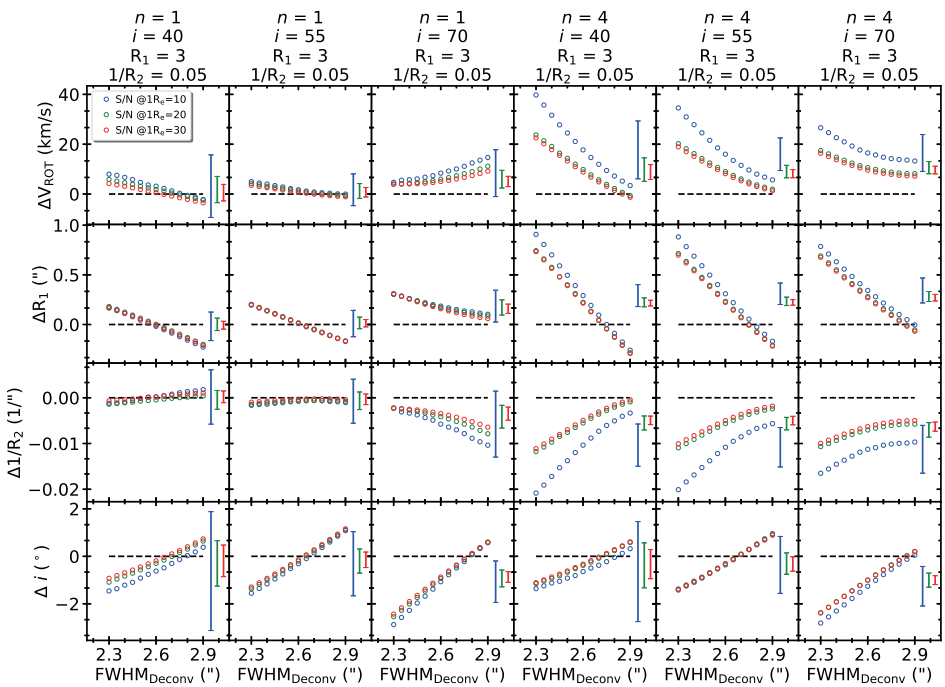

Figure C.12. $R_1 = 3, 1/R_2 = 0.05, FWHMc_0 = 2.6$

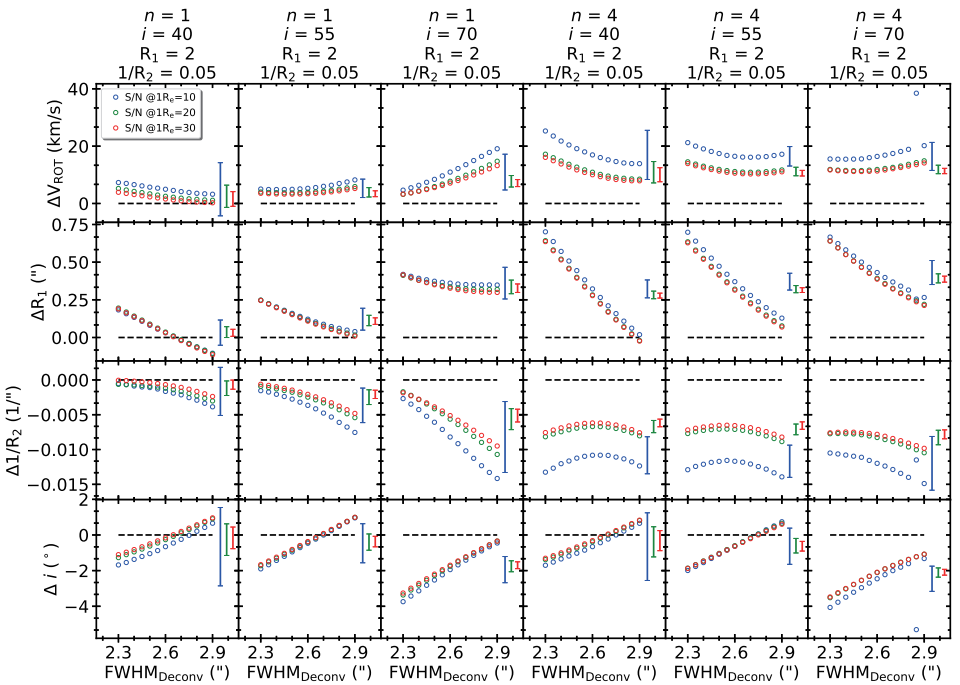

Figure C.13. $R_1 = 2, 1/R_2 = 0.05, FWHMc_0 = 2.6$

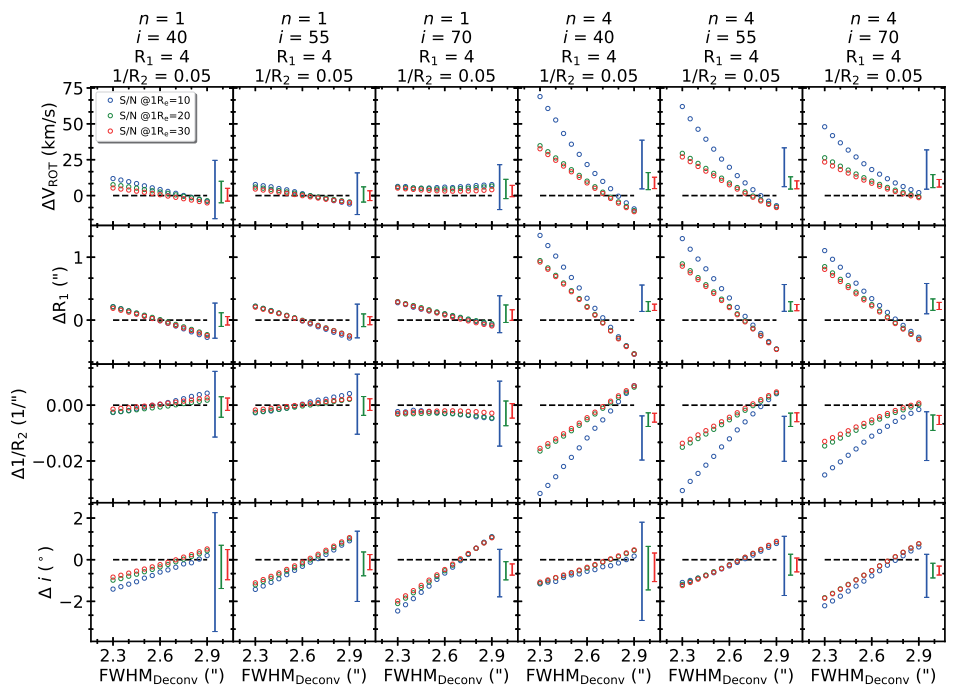

Figure C.14. $R_1 = 4, 1/R_2 = 0.05, FWHMc_0 = 2.6$

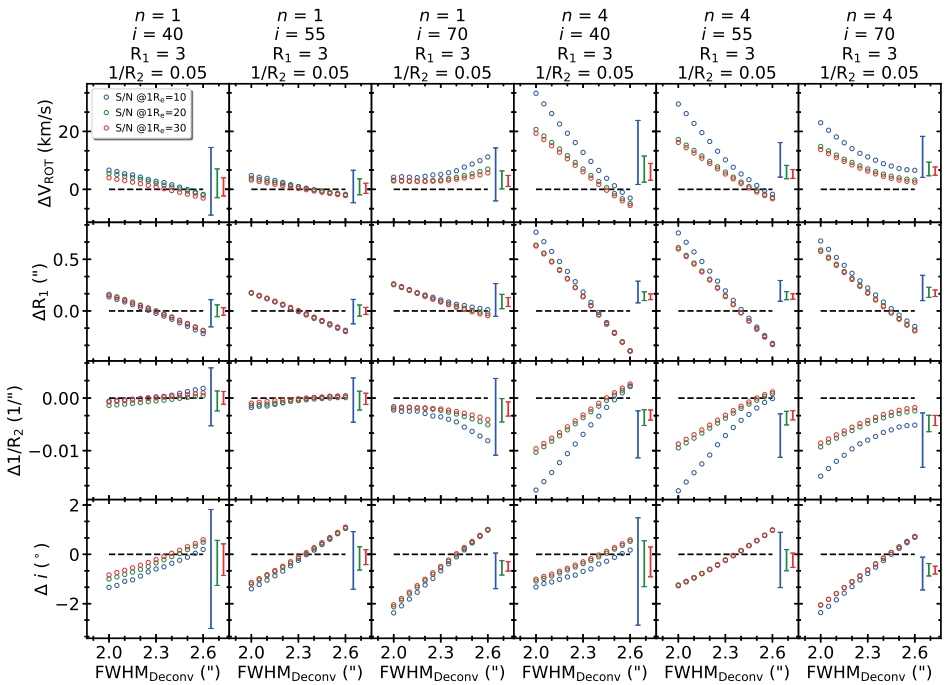

Figure C.15. $R_1 = 3, 1/R_2 = 0.05, FWHMc_0 = 2.3$

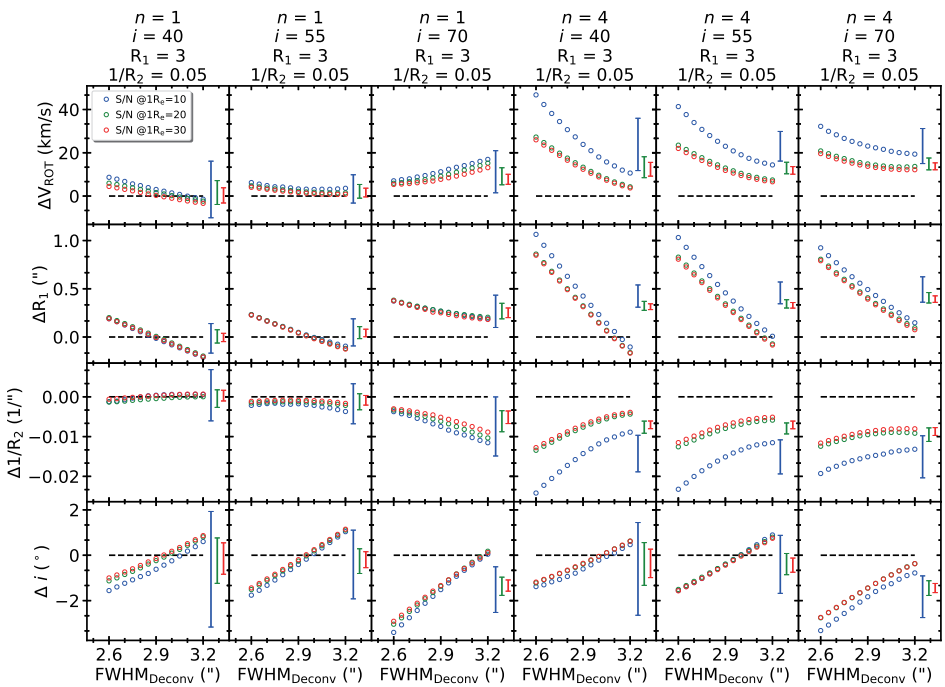

Figure C.16. $R_1 = 3, 1/R_2 = 0.05, FWHMc_0 = 2.9$

요 약

본 학위논문에서는 가까운 은하들의 동역학적 특성과, 그 은하들이 위치한 환경이 동역학적 특성에 미치는 영향에 대한 연구를 수행하였다. 은하들의 동역학적 특성에 관한 연구는 직접적인 관측이 불가능한 암흑 물질에 대한 연구를 가능케 한다는 점에서 중요하다고 할 수 있다. 또한 은하들의 동역학적 특성과 환경의 관계에 대한 연구는 은하 환경이 은하를 구성하는 물질의 분포에 어떠한 영향을 주는지 이해하는 데 있어 꼭 필요한 연구이다.

본 학위논문에서 사용한 주 관측 자료는 4세대 슬로언 전천 탐사 (Sloan Digital Sky Survey-IV) 중 Mapping Nearby Galaxies at Apache Point Observatory (MaNGA) 탐사에서 제공하는 2차원 영역에서의 분광 자료인 Integral Field Unit (IFU) 자료이다. MaNGA는 지금까지 수행된 IFU 탐사들 중 가장 많은 은하를 관측한 탐사로써, 이를 이용하면 넓은 범위의 은하 질량과 형태에 걸쳐 은하의 동역학적 특성에 대한 통계적인 연구를 할 수 있다.

2장에서는 IFU 자료의 공간 분해능을 낮추는 점퍼짐함수 (Point Spread Function, PSF)의 효과를 감소시키고자 IFU 자료에 적용 가능한 PSF 디컨볼루션 (Deconvolution) 기법을 개발하였다. 이 기법은 IFU 자료를 파장별 2차원 이미지로 나누고 각각의 이미지에 대해 Lucy-Richardson 알고리즘을 사용하여 디컨볼루션을 수행한다. 이때 파장에 따라 PSF의 크기를 나타내는 PSF Full-Width-Half-Maximum (FWHM) 값이 변함을 고려하였다. 이 기법은 PSF의 모양을 가우시안 (Gaussian) 으로 가정했을 경우의 PSF FWHM 값과 계산의 반복 횟수, 이 두 가지 변수만을 필요로 하는 것이 장점이다. 본 연구에서는 모형 IFU 자료를 사용하여 PSF가 IFU 자료에 미치는 영향을 양적으로 확인하였고, 동시에 PSF 디컨볼루션 기법이 그러한 영향을 효과적으로 줄일 수 있음을 보였다. 이를 위해 다양한 빛의 분포, 시선방향에 따른 은하의 겉보기 모양, 신호 대 잡음비, 속도 및 속도 분산 분포의 조합으로 만들어진 150,000개 이상의 모형 IFU 자료를 이용하였다. 모형 IFU 자료를 이용한 분석 결과 PSF 디컨볼루션 기법이 잘 작동함을 확인하였고, 기법 적용에 필요한 적절한 계산 반복 횟수가 20회 임을 찾았다. 또한 PSF 디컨볼루션 기법에 사용된 PSF FWHM 값이 실제 자료에 적용되었던 PSF FWHM 값과 $\pm 0.3''$ 정도 차이가 나더라

도 PSF 디컨볼루션 기법이 유의미한 결과를 준다는 것을 보였다. 본 연구에서는 이 기법을 MaNGA 자료에 적용하였으며, 그 결과로부터 구한 2차원 속도/속도 분산 분포가 이전과 비교하여 눈에 띄는 차이를 보임을 확인하였다. 또한 모형 IFU 자료를 이용한 분석한 결과 스핀 변수의 대체값으로 사용되는 λ_{R_e} 변숫값이 이 기법을 적용한 IFU 자료로부터 측정되었을 때 훨씬 정확하게 측정됨을 보였다.

3장에서는 가까운 은하들의 회전속도곡선을 측정하고, 회전속도곡선의 환경 의존성을 연구하였다. 회전속도곡선의 형태를 더 잘 모사하기 위하여 하이퍼볼릭 탄젠트 (hyperbolic tangent) 함수에 선형 항을 더한 함수를 제안하였다. 회전속도곡선 측정에는 PSF 디컨볼루션 기법을 적용한 4,425개 MaNGA 자료로부터 구한 시선방향 속도/속도 분산 분포를 사용하였다. 또한 환경 의존성 연구를 위해 MaNGA 은하들 각각에 대한 작은 범위 환경 변수 (R_n, 가장 가까운 이웃 은하까지의 시선방향으로 투영된 거리)와 넓은 범위 환경 변수 (ρ_{20}, 20개의 이웃 은하들로부터 구한 질량 밀도) 값을 계산하였다. 회전속도곡선 측정이 잘 이루어진 600여 개의 만기형 MaNGA 은하들을 이용한 분석 결과, 은하 바깥쪽의 회전속도곡선 기울기가 다양하게 나타남을 확인하였다. 이러한 바깥쪽 회전속도곡선 기울기는 은하의 별 질량 및 회전속도곡선의 중앙 강체 회전이 끝나는 지점까지의 거리와 양의 상관관계를 보인다. 또한 은하의 T-형태 분류 값이 2 이상일 경우 회전속도곡선의 기울기는 강한 질량 의존성을 나타내었으며 T-형태 분류 값에 따른 의존성은 나타나지 않았다. 반면 은하의 T-형태 분류 값이 2 미만일 경우에는 질량 의존성이 사라지고 T-형태 분류 값에 따른 의존성이 나타났다. 우리의 연구 결과는 회전속도곡선의 모양이 은하의 환경, 특히 가장 가까운 이웃 은하 까지의 거리 및 배경 질량 밀도와 밀접한 관련이 있음을 나타낸다. 이러한 결과는 은하와 은하 사이의 누적된 상호작용과 가장 가까운 이웃 은하의 즉각적인 영향에 따른 것으로 추정된다.

4장에서는 은하회전속도 곡선을 더 정량적으로 이해하기 위해 Jeans-Anisotropsic-Model (JAM) 방법을 사용하여 MaNGA 자료 은하들에 대해 은하들의 질량 구성요소에 따른 질량 분포를 모델링 하였다. 은하 모델의 질량 요소로써는 별과 암흑 물질 헤일로, 두 가지를 사용하였다. Multi-Gaussian-Expansion 방법을 이용하여 은하의 빛과 질량 모형을 기술하였고, 그 결과를 JAM 방법에 적용하여 모형으로부터 예측되는 시선방향 속도 Root-Mean-Square (RMS) 분포와 MaNGA 자료로부터 얻어진 시선방향 속도 RMS 분포를 비교하는 방식으로 은하의 질량 분포를 모델링 하였다. 관측 결과와 가장 잘 일치하는

모델 변수 조합을 구하기 위하여 Markov-Chain Monte Carlo 방법을 사용하였다. 얻어진 은하들의 3차원 질량 밀도 분포는 다양한 별 질량-광도 비율, 속도 타원체의 이방성, 암흑 물질 비율과 암흑 물질 분포의 안쪽 기울기 값을 보였다.

더불어 지금까지의 이루어진 연구들의 후속 연구를 가능케 하는 관측 기기 개발 연구를 수행하였다. Devasthal Optical Telescope Integral Field Spectrograph (DOTIFS)라고 불리는 이 관측기기는 광섬유와 렌즈 조합을 기반으로 한 여러 개의 IFU를 가진 분광기로써 16개의 물체를 한 번에 관측할 수 있다는 점이 특징이다. DOTIFS의 실시간 IFU 배치 시스템은 IFU 재배치에 많은 준비 시간이 필요한 다른 분광기들과 비교하여 큰 강점이라 할 수 있다. 본 연구에서는 이 기기의 개발 초기부터 기기의 개념설계를 수행하였고, 기기의 요구 조건에 부합하는 실현 가능한 기기 디자인을 제시하였다. 또한 기기의 분광기 콜리메이터와 카메라 광학계, 전방 광학계, 보정 광학계를 설계하였다. 더불어 공차분석과 열분석을 수행하였고, 분석 결과를 이용하여 온도 변화가 광학계에 미치는 영향을 줄이기 위한 해결방안을 제시하였다. 마지막으로 기기에 필요한 프로그램인 분광기 CCD 이미지 시뮬레이터 (simulator)와 이 기기를 이용한 관측에서 예상되는 신호 대 잡음비 (signal-to-noise ratio) 를 계산하는 프로그램을 개발하였다. DOTIFS는 미래에 MaNGA 은하들에 대한 후속 관측 및 가까운 은하들의 외곽부 관측과 상호작용은하, 그리고 병합은하 시스템 관측 등에 사용될 예정이다.

주요어: 은하, 기술:디컨볼루션, 은하:회전속도곡선, 은하:동역학, 기기:분광기

학 번: 2012-23104

감 사 의 글

누구에게나 그렇겠지만, 학위를 마치기까지 지난 7년 동안 참 많은 일이 있었습니다. 학교와 고등과학원, 그리고 인도 IUCAA를 오가며 학위 과정을 밟아가는 동안, 그 모든 곳에서 저를 따뜻하게 맞아주고 또 지지해주신 많은 분들, 동료, 선후배, 그리고 친구들 덕분에 무사히 학위를 마칠 수 있었습니다. 그분들께 이 자리를 빌려 감사의 인사를 드리고자 합니다.

먼저 8년 전 아무것도 모르던 학부생의 이메일에 정성스레 답해주시고, 부족한 점이 많은 저를 인내와 격려로 지도해주신 박창범 교수님께 감사드립니다. 교수님께 박사과정생으로서 지도 받을 수 있었던 것은 제 인생의 크나큰 행운이었습니다. 교수님께서 몸소 가르쳐 주신 학문을 대하는 방식과 학자로서의 자세는 연구자로서 평생 견지하며 살아가도록 하겠습니다.

Also, I would like to express my deepest gratitude to Prof. A. N. Ramaprakash. I sincerely appreciate all the insightful guidance and advise you have provided throughout the journey and especially the opportunity to be involved in the development of DOTIFS from the very beginning to date. 여러 요청에 항상 긍정적으로 응하여 주시고, 연구에 어려움이 없도록 아낌없이 지원해주신 저의 또 다른 지도 교수님이신 박용선 교수님, 진심으로 감사드립니다. 저의 박사학위 논문 심사위원을 맡아주신 임명신 선생님, 김웅태 선생님, 그리고 이종철 박사님께도 감사의 말씀을 드립니다. 부족함이 많은 논문임을 잘 알고 있습니다. 이를 마중물 삼아 더 많은 일을 할 수 있는 기회를 주신 것으로 생각하고, 열심히 하는 모습 보여드리겠습니다.

대학원 생활 가운데 헤아릴 수 없이 많은 깨달음과 가르침을 주시고 참 연구자로서 본을 보여주신 학과의 교수님들께도 감사 인사를 전합니다. 박사과정 초기, 천문학의 기초를 다지는데 큰 가르침을 주신 구본철 선생님, 감사드립니다. 대학원에서 가장 많은 수업을 들은 이명균 선생님, 행복한 천문학자의 모습에서 많은 교훈을 얻었습니다. 감사드립니다. 항상 열정적인 강의를 해주시고, 찾아뵐 적마다 유익한 말씀 나눠주신 이정훈 선생님과 세미나 수업을 통해서 논문 해석에 많은 가르침을 주시고 제 연구에 관심을 가져주신 우종학 선생님, 감사드립니다. 윤성철 교수님, 교수님께 들었던 항성 내부 구조 강의는 대학원에서 수강한 가장 인상 깊었던 수업 중 하나였습니다. 교수님 덕분에 별에 대해 조금이나마 더 깊은 이해를 할 수 있었습니다. 감사드립니다.

박사과정이라는 긴 여정에서 셀 수 없이 많은 도움을 주신 황호성 박사님, 저의 무수한 질문에도 항상 명쾌한 답 주시고, 위기 때마다 피가 되고 살이 되는 조언 주셔서 감사합니다. 박사님의 연구하시는 모습을 근거리에서 보고 배우며 함께 연구할 수 있음이 큰 기쁨이었습니다. 앞으로도 동료 연구자로서 박사님을 통해 많은 배움 얻게 되길 기대합니다.

19동에서 함께 수업 들으며 동고동락한 대학원 선배, 동기, 후배들에게도 감사의 말을 전합니다. 대학원 입학 동기 탁과 용민이 형, 대학원 내내 많은 시간을 같이 보낸 수업 동기 용정이, 종호, 헌철이 그리고 졸업한 윤영이, 고맙습니다. 함께한 시간이 대학원 생활에 큰 활력이 되었습니다. 다재다능한 능력자 민희 누나, 함께 졸업하는 재진이 형, 항상 성실한 유나에게도 고맙다는 말 전합니다. 졸업학기에 같은 방 연구실 쓰던 후배들 강주형, 문재연, 김주연. 말년 선배를 상대해주어 고맙습니다. 앞으로도 즐거운 연구생활 이어나가길 바라겠습니다. 연구 외적인 부분에서 지원을 아끼지 않으신 천문학 전공 행정실 선생님들께도 감사 말씀드립니다. 특별히 학생들 한 명 한 명에게 많은 도움 주시는 노현주 선생님께도 특별히 감사드립니다.

학위과정 동안 여러 면에서 도움 주시고 조언과 격려를 아끼지 않으신 고등과학원의 김용휘 박사님, 김주한 교수님, 심준섭 박사님, 이재현 박사님, 전현성 박사님, 홍성룡 박사님 감사합니다. 특히 함께 인도를 오가며 수고하시고 급한 부탁에도 흔쾌히 저의 조악한 글들에 의미 있는 코멘트 주신 홍성욱 박사님, 감사합니다. 김은빈 박사님, 송현미 박사님, 신지혜 박사님, 윤미진 박사님. 덕분에 고등과학원을 비롯하여 여러 학회와 워크숍에서 유쾌한 시간을 보낼 수 있었습니다. 감사하다는 말 전합니다. 저의 첫 관측 자료 연구가 결실을 맺을 수 있게 해주신 고종완 박사님께도 감사 말씀드립니다. My sincere appreciation also goes to all the present and formal members of the IUCAA instrumentation laboratory. Abhay, Bhushan, Chaitanya, Deepa, Hillol, Jyotirmay, Kalpesh, Madhusudan, Mahesh, Mandar, Pravin Chordia, Pravin Khodade, Rani, Ravi, Sabyasachi, Sakya, Shreeram, Siddharth, Sujit, Swapnil, Vilas, and Vishal. I would not be able to thank enough for all the dedicated works and kindness in all aspects. I truly hope our paths cross again in the future. And, Prof. Ajit Kembhavi and Prof. Somak Raychaudhury, your continued support and guidance in developing DOTIFS have been such a blessing for me.

그동안 천문학 하겠다는 아들을 한결같이 신뢰하고 물심양면으로 지원해주신 아버지와 어머니께 한없는 감사와 사랑을 전합니다. 꾸준히 노력하고 정진해서 더 자랑스러운 아들, 효도하는 아들 될 수 있도록 하겠습니다. 세상에 하나뿐인 사랑하는 동생, 성은이에게도 응원해주어 고맙다는 말 전합니다. 또한 박사과정 학생이었던 저를 가족으로 받아주시고, 찾아뵐 때마다 반갑게 맞아주시는 장인어른, 장모님, 그리고 처가 식구들에게 감사 말씀 전합니다. 떨어져 지낸다는 이유로 더 많은 시간을 함께 보내지 못해 아쉬운 마음과 죄송한 마음이 큽니다. 앞으로 더 잘하고 아름다운 가정 세워나가도록 계속 힘쓰겠습니다. 마지막으로 학자로서의 제 삶을 늘 격려하고 응원해주는 아내 사라씨에게 고맙고 사랑한다는 말 전합니다. 여보는 배울 점이 참 많은 사람입니다. 살아가면서 앞으로도 함께 더 많이 배우고 성장할 수 있기를 바랍니다. 지난 2년 4개월 동안 우리 가정에 크나큰 행복을 가져다준 딸 시온이게도 고맙다는 말 전합니다. 사랑하는 딸 시온, 언젠가 네가 집 책장 한쪽에서 이 글을 발견하는 날, 지금만큼이나 사랑스러운 모습으로 성장해 있길. 그리고 아빠는 시온이 보기에 자랑스러운 아빠가 되어있길. 우주만큼 사랑해!